A comparison of Logging While Drilling (LWD) and Wireline acoustic measurements.

by

Victoria Alice Briggs

Submitted to the Department of Earth Atmospheric and Planetary Science
in partial fulfillment of the requirements for the degree of

Doctor of Philosophy

at the

MASSACHUSETTS INSTITUTE OF TECHNOLOGY

September 2006

Author ....
Department of Earth Atmospheric and Planetary Science
September, 2006

Certified by ....
M. Nafi Toksöz
Professor of Geophysics
Thesis Supervisor

Accepted by ....
Maria T. Zuber
E.A. Griswold Professor of Geophysics. Head, Department of Earth,
Atmospheric and Planetary Science

A comparison of Logging While Drilling (LWD) and Wireline acoustic measurements.

by

Victoria Alice Briggs

Submitted to the Department of Earth Atmospheric and Planetary Science
on May, 2006, in partial fulfillment of the
requirements for the degree of
Doctor of Philosophy

Abstract

The instruments used to measure borehole acoustic data can be classified as either wireline or logging while drilling (LWD). The wireline tool measures formation speeds after the borehole is drilled, and the LWD tool measures formation speeds while the borehole is drilled. This thesis focusses on comparing the data collected by these tools and how formation properties affect their measurements.

LWD and wireline measurements taken from the same borehole are compared. Discrepancies in estimated shear and compressional velocities, as calculated by time semblance methods, were found between the two data sets. We modeled radially layered formations with increasing or decreasing radial velocity profile to estimate the acoustic measurement penetration for each tool. We reprocessed sections of the data using frequency semblance methods and compared with layered model results. We found that a frequency-domain analysis is feasible and reduces the overall difference between the LWD and wireline shear and compressional velocity estimates. The remaining discrepancy can be explained by the different radial depths of penetration of these two tools, which naturally leads to a difference in the velocity estimates when there is a radial gradient in the velocity profile.

We model axisymmetric propagation of waves in a borehole with a transversely isotropic (TI) formation. An algorithm is developed for an arbitrarily radially layered medium that can be used to approximate the steel LWD tool inside the fluid-filled borehole. We present a full description of modal arrivals, as a function of frequency and phase velocity, for the LWD tool and compare with the wireline case, both for isotropic and TI formation. The tool modes were found to be largely unaffected by the presence of a TI medium while the modes associated with the borehole fluid and formation, i.e. Stoneley, pseudo-Rayleigh and borehole flexural modes, displayed sensitivity to the TI formation parameters, specifically to C_{44} in the elastic stiffness matrix. Our analysis demonstrates that at a lower frequency of operation, the LWD tool can potentially measure the effect of a TI medium in the fundamental shear modes, if the modes are well-coupled to the formation (i.e., the formation is soft).

This thesis makes two new contributions to the field of borehole geophysics. Firstly, we make an independent comparison of LWD and wireline measurements, and our work suggests that frequency-domain semblance processing may be a better method of analysis, particularly in radially varying formations. As industry moves toward faster and more cost efficient LWD measurements, it is essential to understand the implications of the LWD tool geometry in relation to its wireline counterpart and how traditional velocity processing methods are affected. Secondly, we present a modal analysis of the LWD tool in a transversely isotopic formation, which suggests that the newer generation of LWD tools, operating in a lower range of frequency may be able to measure TI formations. The TI medium is of major importance to exploration geophysics as it represents the anisotropy found in thinly layered media, i.e. sedimentary strata. This is the predominant form of anisotropy seen in many sedimentary basins, so that its effect on LWD measurements is of great interest to exploration geophysics.

Thesis Supervisor: M. Nafi Toksöz
Title: Professor

Contents

List of Figures

List of Tables

Chapter 1

Introduction

In this thesis, we present a systematic comparison of two acoustic logging tools used in the industry to estimate formation shear velocities. These tools are the "wireline" tool, which is used to perform acoustic measurements after the borehole is drilled, and the "logging while drilling" (LWD) tool which is used to perform measurements while the borehole is being drilled. Due to the very different mode of operation of these tools, they must satisfy very different physical constraints, so that their physical dimensions are different, as well as their operating frequencies. The goal of this thesis is to compare both tools from a measurements perspective as well as from a theoretical modeling standpoint, and to offer possible explanations for some of the differences in shear and compressional measurements achievable with these tools.

This thesis consists of two parts: in the first part, we compare measurement data taken with both tools in the same borehole and quantify the differences in the estimated shear and compressional velocities. Several scenarios are investigated to account for the difference in estimated velocities using these two tools. In particular, we compare two different methods of velocity processing: time domain semblance and frequency-domain semblance. In addition, we model the effect of the different source-receiver offsets and the different frequency ranges of the tools. Finally, we model the effect of radially non-homogeneous formation velocities around the borehole. Because of their different geometries and ranges of operating frequencies, LWD and wireline tools inherently probe the formation at different radial depths from the borehole, so that any radial inhomogeneity results in different estimated velocities. In the second part of this thesis, we consider the effect of transverse anisotropy in the formation on the tool acoustic measurements. We extend previous models of the acoustic modes associated with borehole acoustic logging tools, in particular the theory for a radially multilayered medium is applied to the LWD tool in a transversely isotropic (TI) formation and its effects on the tool modes are studied. The developed algorithm has the flexibility to add an arbitrary number of layers which can be defined as fluid or solid with the outer most layer being isotropic or transversely isotropic. The code is used to generate the modes for the wireline and LWD tools in isotropic and TI formations. It is also used to generate the tool response in multi-layered formations with both increasing and decreasing radial velocity profiles, to simulate damaged and flushed zones. The results of these studies are compared with data taken from a well where both the wireline and LWD tool were used to log the formation properties.

The above research makes two important and new contributions to the field of borehole geophysics. Firstly we make an independent comparison of wireline and LWD data. We are fortunate to have data taken from the same borehole with both tools, giving a unique opportunity to compare the two in identical formations. Additionally we show how complicated radial structure surrounding the borehole influences both the wireline and LWD data and how, using careful processing methods, we can recognize this in the data. Lastly, we present for the first time a method for LWD mode analysis in a TI formation. This type of anisotropy is commonly found in sedimentary strata seen in oil reservoirs and for this reason it is essential to understand how it effects measurements made with LWD technology.

In the broadest sense the development of new acoustic logging tools aims to improve subsurface seismic velocity estimations from borehole acoustic data. The data is taken using a logging sonde which excites and records acoustic waveforms measured along the borehole at regular intervals. Typically the data are measured at depths relevant for oil reservoirs which are usually between 1000 to 10,000 m. Borehole geophysics refers to the study of subsurface properties using measurements made at varying depth in drilled boreholes. While borehole geophysics is often applied to the petroleum industry, data taken at the borehole scale can have a much broader applicability in the geo-sciences. Measurements which can better characterize subsurface properties are directly relevant to flow modeling, fluid delineation and saturation, to seismology (both on the reservoir and the global scale), as well as to time reverse acoustics to name a few. In short, the methods and data presented in this thesis can be used to better define subsurface properties, as well as to refine and improve models in many areas of geophysics not restricted to petroleum applications.

A large portion of the work presented here concentrates on measurements made by LWD tools. LWD tools are at the current forefront of borehole measuring technology and much of the recent literature in borehole geophysics has been directed at interpretation methods for LWD measurements. Another topical area of research is that of reservoir anisotropy. Until recently, in the last twenty years or so, the formation surrounding the borehole was modeled as homogeneous and isotropic. This assumption simplifies the physics and mathematics of modeling and data interpretation considerably, and produces reasonable and useable results. Indeed many formations are essentially isotropic and homogeneous on the scale at which the measurements are made. However, with escalating computational power and ever dwindling oil resources, it is possible and increasingly important to account for certain types of anisotropy seen at the reservoir scale.

Much of the research pertinent to borehole geophysics, and to the sub-discipline of borehole acoustics, can be found in geophysical and acoustics journals, with areas of cross-over with medical imaging techniques. The main drivers for research of this type are the larger oil and oil service companies and academic institutions. Seminal papers such as White (1968) and Biot (1952) formulated the equations and solutions to describe the propagation of waves in a borehole environment. The second generation of research, seen in papers such as Cheng and Toksöz (1981), Tsang and Rader (1979), Schmitt and Bouchon (1985) and Kurkjian (1985) focussed on reproducing the seismograms as measured by the logging sonde. This work was further extended to include radial layering, poro-elasticity and transverse isotropy, White and Tongtaow (1981), Schmitt (1989), Schmitt (1988a), Ellefsen (1990) and Leslie and Randall (1992).

Simultaneously to the theoretical work referenced above, a body of work on interpretation of acoustic data was also published. Very early tools used just one or two receivers and formation compressional velocity was calculated from the distance between source and receiver divided by the time taken for the first break to arrive at the receiver. As full waveform logging was developed, i.e. where the full wavetrain is recorded, and the number of recievers was increased, the methods to extract the formation shear and compressional speeds became more advanced. Semblance Time Coherence (STC) methods, Kimball and Marzetta (1984) and for dispersive arrivals Kimball (1998), Tang et al. (1995) and frequency domain methods Lang et al. (1987), Sinha et al. (1994), Huang et al. (1998) and Rao (2005). More recently, measurements using tools developed with orthogonally placed sources and receivers, have enabled stress-induced, or azimuthal anisotropy, to be estimated in-situ, Sinha and Kostek (1996), Tang and Chunduru (1999) and Tichelaar and Hatchell (1997).

We have cited here just a few of the authors who have made contributions to the field over the last few decades, and very briefly covered some of the larger areas of interest. Much of this research however was completed before the LWD tool had been implemented and therefore many of the well understood facets of borehole acoustics must be re-examined for the newer tool geometries.

In chapter 2 we present a discussion of the various types of industry logging sondes, with an emphasis on wireline and LWD acoustic tools. We present an overview of the acoustic modes of the isotropic borehole environment for both tools. We show the cases for both fast and slow formations and the response for monopole, dipole and quadrupole excitations. We start by presenting a full modal analysis for these tools, and then emphasize those modes which are pertinent to the borehole formation properties. We discuss qualitatively the mode characteristics and how they affect the interpretation of data seen in later chapters. Finally, we briefly discuss methods of velocity analysis in the time and frequency domain.

In the following section, chapter 3, we compare LWD and wireline data taken from the same borehole. The data show some initial discrepancies which cannot be explained by formation alteration or inherent tool differences. We reprocess the waveforms using frequency domain methods and the resulting differences between data sets are explained by the use of three radially layered formation velocity models. The numerical code developed in chapter 4 is used to model the radially layered media and the results are compared with the data. Velocity processing methods are compared and tool measurement penetration is discussed.

Chapter 4 outlines the theory for the mode analysis, we describe how to solve the wave equation in a TI medium using cylindrical coordinates and how to compute the solution for a given phase velocity and frequency. In this chapter, the focus is on the LWD tool in the TI formation but the equations are easily reducible to the wireline and/or the isotropic case. We outline the algorithm used to create the multi-layer model and present results for the wireline and LWD tools in fast and slow TI media using monopole, dipole and quadrupole excitations.

Appendix A outlines the theory, presented in chapter 4, for a simple two-fluid case. The absence of shear waves in the fluid-fluid model greatly simplifies the theory, making it possible to solve analytically. This section is included as a simple introduction to the theory presented in chapter 4.

Appendix B gives the full formulation of the equations needed to solve the TI, LWD system. They are presented as matrix elements which are plugged in to the equations in chapter 4.

The final appendix, appendix C, presents a method used to calculate the stress induced anisotropy using four component acoustic data. This appendix uses a different data set and has no LWD data, and therefore is not directly applicable to compare LWD and wireline tools. Additionally this type of anisotropy is seen in vertically fractured media and not in the layered media modeled in the TI case in chapter 3. However, it may still be of interest to the reader as it discusses formation flexural modes and how they are influenced by azimuthal anisotropy. It describes a method of dispersion analysis from tool seismogram arrays and presents cross-dipole acoustic data giving further insight into tool operation.

Chapter 2

Tool design, Overview of modes in isotropic formations and Velocity processing methods.

2.1 Logging Tool Design

In this section of the thesis we present a brief overview of general tool design for use in a borehole environment. The goal of this thesis is to compare the data from a wireline and LWD perspective and in later chapters we model two generic versions of these acoustic tools. Figure 2-1 shows a cartoon of the respective tools in the borehole, note the difference in length and diameter of the tools and the size of the fluid annulus between the tool and the borehole wall. . However it should be noted that there are a broad range of logging tools available and depending on the type of formation, borehole fluid and data requirement there are many types of measurement that can be taken in-situ. This section serves as a brief introduction to these tools and some of the measurements made, with an emphasis on acoustic data.

Taking physical measurements in the borehole environment presents numerous engineering challenges. The tool must withstand extreme conditions of intense heat

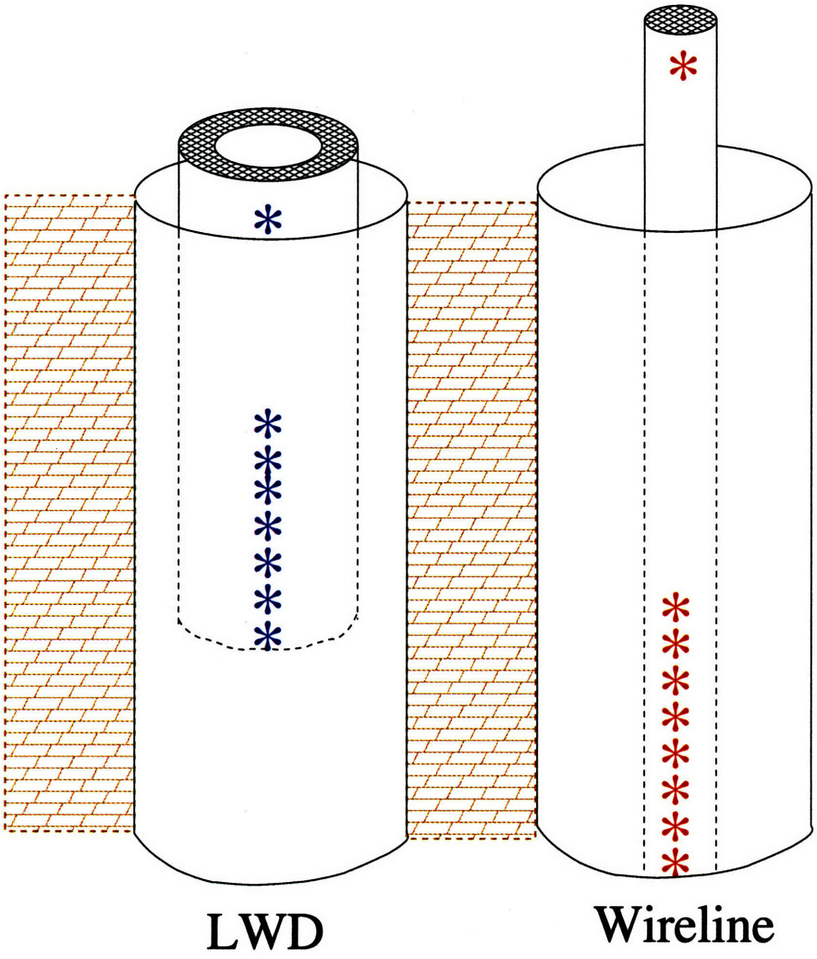

Figure 2-1: Cartoon of generic LWD and wireline tools in the borehole. The blue and red stars represent the source and receiver array.

and pressure, in a fluid-filled and remote location. In addition, efficient coupling of the tool to the physical environment must take place in a very limited space. The borehole is drilled in sections, of decreasing diameter, starting at near 36" near the surface and decreasing to as little as 4.5" at large depth. After each section is drilled, logging tools can be used to record data before the section is cased with a steel pipe to maintain stability. Some wireline measurements can be made after the well is cased, however, for acoustic measurements the open hole is the preferred environment. As the diameter of the borehole changes so does the tool used to make the measurement. A specific tool may come in 5 or 6 different diameters so that an appropriate borehole to tool diameter ratio is optimized over the length of the well.

Borehole logging measurements can be separated into two groups, measurements made while the borehole is drilled, called "Logging While Drilling" (LWD), and measurements made after the borehole is drilled, called wireline. Common types of measurement include acoustic measurements for formation shear and compressional velocites, resistivity measurements for hydrocarbon saturation and porosity, spontaneous potential measurment as a lithological indicator, gamma ray measurement as a lithological indicator and shale fraction estimator, and finally neutron logs, for porosity estimation. This list is by no means exhaustive but gives a few of the possible measurements that can be made in-situ. In addition to these formation measurements there are also readings such as caliper measurements, for borehole diameter and ellipticity estimation, which give information about the state of the borehole. While these measurements are not necessarily of direct use to formation evaluation, they are of extreme importance to interpreting the data pertinent to the formation.

In this thesis we concentrate on acoustic measurements. Acoustic data can be measured in several ways depending on the formation property of interest. In chapter 3 we present monopole and dipole data taken in the same well for wireline and LWD tools, although these are not the only type of acoustic data that can be measured. Monopole sources excite axi-symmetric modes and are used primarily to estimate formation compressional and shear velocities from refracted arrivals in fast formations. The compressional refracted arrival can be detected using this measurement regardless of whether the formation is fast or slow, since the compressional velocity in the solid is always greater than that of the borehole fluid. The shear refracted arrival however, only exists in fast formations where the shear velocity in the solid is faster than that of the borehole fluid. In slow formations, dipole data is used to measure modal arrival and estimate the formation shear velocity. We discuss modes in more details in section 2.3. In addition to monopole and dipole tools, some acoustic logging tools are capable of measuring quadrupole and higher order modes, which are also useful for determining formation shear velocities. Finally, we present a study of a cross-dipole tool in appendix C, used to measure azimuthal variation of formation velocities. In contrast to the measurements described above, the cross-dipole measurement uses sources and receivers that are oriented orthogonally in the azimuthal direction. This so-called cross-line data, is used to determine azimuthal variation in velocity and thus, horizonthal formation stresses.

2.2 Summary of main differences between LWD and wireline acoustic logging tools

While there is much variation between LWD and wireline tools in the industry, there are certain properties which are common to most tools. In general, the LWD tool has a greater diameter and a shorter offset between source and receiver than its wireline counterpart. The LWD tool must withstand harsher conditions than the wireline tool since it is used for logging while drilling and is therefore designed to be more robust. The LWD tool has a hollow center to allow the drilling mud to flow through the borehole, removing the cuttings from the drilling bits. The flow of fluid and borehole cuttings around the tool create noise in a frequency band of 0 to 5 kHz, so that data is recorded in a higher frequency band to avoid contamination by the noise. For the wireline tool however, this low frequency noise is not present, so that operating frequencies in the 0 to 5 kHz are possible. Additionally the wireline tool takes measurements as a function of depth whereas the LWD tool takes measurements as a function of time. This is important when comparing the data as the formation velocities have not necessarily been sampled at exactly the same locations along the borehole wall and if thin layering is present there may be discrepancies. In chapter 3 we present a comparison of two particular acoustical tools used in the industry whose main differences are outline above and discussed in further details in the chapter.

2.3 Overview of Modes

Before complicating the modal analysis with the transversely isotropic formation or a radially layered formation, we present the modes for the LWD and wireline case in a isotropic homogeneous formation. It is important to understand under which conditions certain modes are excited and how they interact for a given tool and borehole geometry. The wireline case, which is modeled as a fluid filled borehole shows the simplest example while the addition of the LWD tool and inner fluid annulus excites more complicated modes. The order of the source type, e.g. monopole, dipole or quadrupole and whether the formation is fast or slow, are also necessary considerations in determining which modes are present. Here we present a brief overview of the expected modes excited in the wireline and LWD cases. We show monopole, dipole and quadrupole responses to fast and slow isotropic formations and discuss nomenclature and characteristics. The model parameters and formation velocites for the fast and slow mediums are given in table 2.3.

The borehole radius used is 0.11m and the LWD tool's inner and outer radii are 0.024m and 0.092m respectively.

2.3.1 Wireline

The wireline case is most often modeled as a fluid filled borehole surrounded by an infinite formation. The tool itself, which has a much smaller diameter than the LWD

	Vp $[ms^{-1}]$	Vs $[ms^{-1}]$	ρ $[kgm^{-3}]$
Fast Formation	3309	1819	2440
Slow Formation	2024	1180	2440
Steel Tool	6500	3000	7800
Fluid	1500	0	1000

Table 2.1: Formation parameters used for the models in this chapter.

tool, has only an outer radius and can be modeled as a solid steel pipe. In reality the tool is filled with the necessary electronics to excite and record the borehole response, but it has no inner free space that is open to the borehole, which is unlike the LWD tool. The shear and compressional velocities and the density of the tool can take into account the internal electronics to yield some average values slightly less fast and dense than solid steel. The algorithm described in chapter 4 can easily handle the additional solid layer at the center of the borehole but here we follow convention and model the wireline case as the fluid filled borehole without the tool. This allows us to view the modes associated with the formation, and therefore of the most interest, easily and is also considered valid as the sources and receivers are very well insulated for the wireline case reducing the possible tool modes substantially.

Wireline: fast formation, monopole, dipole and quadrupole

In a fast formation as seen in figure 2-2, both the monople (axisymmetric), dipole (non-axisymmetric) and quadrupole (non-axisymmetric) modes are plotted for comparison. The monopole excites Stoneley and Pseudo-Rayleigh modes, the dipole excites formation flexural modes and the quadrupole excites formation screw modes.

The fundamental modes in each case exist at all frequencies and asymptote to the Scholte velocity at high frequencies, Schmitt (1988b). The Stoneley mode, for the fast formation parameters, exhibits reverse dispersion which is characterized by an increase in phase velocity with frequency. The Stoneley wave travels in the fluid at the fluid-borehole interface and is strongly coupled with the fluid properties, especially in fast formations. We will further discuss the zero frequency phase velocity asymptote which determines whether the dispersion in direct or reversed in chapter 4. The Pseudo-Rayleigh modes, which are also excited by the monople source, have definite cutoff frequencies below which they cannot exist. These cutoff frequencies increase with each higher mode. At the low frequency cutoff they travel at the formation shear velocity and asymptote to the fluid compressional velocity at high frequencies. The dipole source excites the fundamental formation flexural mode and higher flexural modes. The higher flexural modes and higher quadrupole screw modes are analogous to the pseudo-Rayleigh modes in that they have defined cutoffs below which they do not exist. All of the higher order modes for monopole, dipole and quadrupole asymptote to the formation shear velocity at low frequencies and to the fluid compressional velocity at high frequencies in the case with a fast formation.

Wireline: slow formation, monopole, dipole and quadrupole

In the slow formation only the fundamental modes for the monopole and dipole are excited, i.e when the mode phase velocity is less than the formation shear velocity. Modes which travel above the formation shear velocity radiate energy into the solid and are termed leaky modes. Figure 2-3 shows the excited modes for monopole, dipole and quadrupole in a slow medium where the formation shear velocity is less than that of the borehole fluid compressional velocity. Similarly to the fast formation the monople excites the Stoneley wave which starts at the tube wave velocity at zero frequency and asymptotes to the Scholte velocity at high frequencies. However in this case the dispersion is direct due to the fluid compressional velocity being higher than

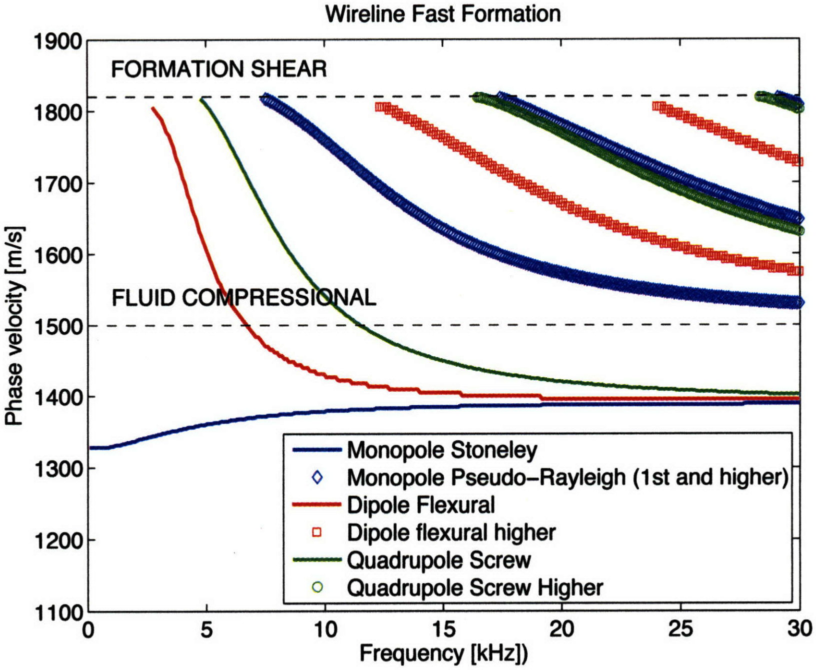

Figure 2-2: Wireline monopole and Dipole in a fast isotropic formation

the formation. The borehole flexural mode reaches the formation shear velocity at low frequencies and has the same Scholte velocity as the Stoneley at high frequencies, similarly for the quadrupole screw mode.

2.3.2 LWD

The LWD tool is attached to the drill string and takes measurements as the borehole is being drilled, meaning that the tool must be able to withstand much higher pressures than the wireline. This leads to a much larger and more robust tool making the tool modes harder to suppress. The borehole modes are complicated by the presence of a steel tube within the borehole and a small annular fluid between the tool and formation. The tool itself generates modes which couple with the modes generated by the formation and both the inner and outer fluid layers propagate a Stoneley wave. Here we model the borehole and tool together as the interaction of the tool and formation modes provides a more realistic basis for interpretation of real LWD data.

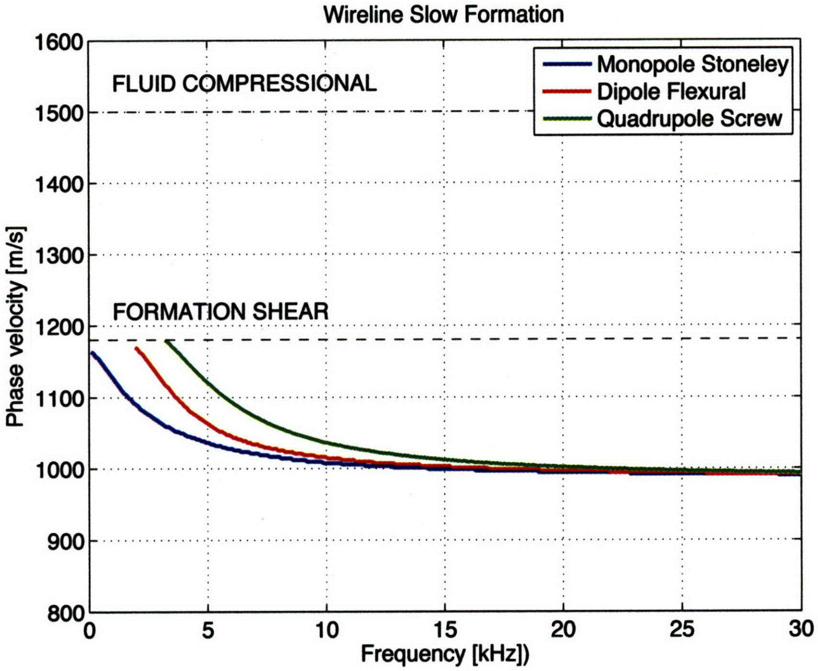

Figure 2-3: Wireline monopole and Dipole in a slow isotropic formation

LWD: fast formation, monopole, dipole and quadrupole

Figure 2-4 shows all the modes associated with the tool and formation for the LWD case in a fast formation with monopole, dipole and quadrupole excitation. The addition of a steel tube in the center of the borehole considerably complicates the interaction of modes. When two modes approach each other at a given frequency and phase velocity they will not cross but instead exchange character, this is termed as an avoided crossing and is of particular importance in the dipole case. Incorrectly identifying a modal arrival in the seismogram data may lead to erroneous velocity estimations and so it is of great importance to understand how the modes interact and influence each other. Figure 2-5 shows a closer view of the modes associated with the formation in the LWD case. These are the modes of primary interest in the analysis of borehole data.

In a similar pattern to the wireline case the LWD monopole excites Stonely and pseudo-Rayleigh waves with a monopole source. The Stonely has no cutoff and travels at a lower phase velocity than in the wireline case at low frequencies and has a comparable phase velocity at high frequencies. The fundamental pseudo-Rayleigh mode has a cutoff at much higher frequencies compared with the wireline case, this is due to the smaller fluid annulus between the tool and formation. The smaller dimension means that the longer wavelengths cannot propagate constructively along the fluid and only at higher frequencies can the mode exist.

The dipole formation flexural mode for the LWD case has a dramatic change in character from the wireline case caused by the presence of the tool flexural mode. Without the confines of a borehole the tool flexural mode (seen in figure 2-4) would normally start at zero phase velocity at zero frequency and slowly increase to the tool shear velocity as the frequency increases. If the tool were in free space this would correspond physically to the change from the waves exciting the bending of the whole tool, at low frequency, to waves which travel just along the surface at high frequencies, i.e. Rayleigh waves which travel at 0.919 of the shear velocity. (It should be noted in figure 2-4 that the tool flexural mode is subject to another avoided crossing with one of the higher order dipole tool modes and therefore does not reach the Rayleigh velocity associated with tool shear velocity in this example.) The presence of the tool and borehole cause the tool flexural and borehole flexural to interact and exchange character either side of an avoided crossing. This means that the borehole flexural mode, which would have asymptoted to the formation shear velocity, now takes on the tool flexural character at low frequencies and similarly the tool flexural mode now resembles the wireline borehole flexural at low frequencies. The geometry of the tool in relation to the borehole defines where the modes interact and for the example shown in figure 2-4, it is around 3 kHz. At high frequencies the borehole flexural is unchanged and tends to the Stoneley velocity.

The fundamental quadrupole screw mode asymptotes to the formation shear at low frequencies and to the Scholte velocity at high frequencies. The higher order screw mode is also excited and has similar asymptotes to the fundamental screw mode but at much higher frequencies.

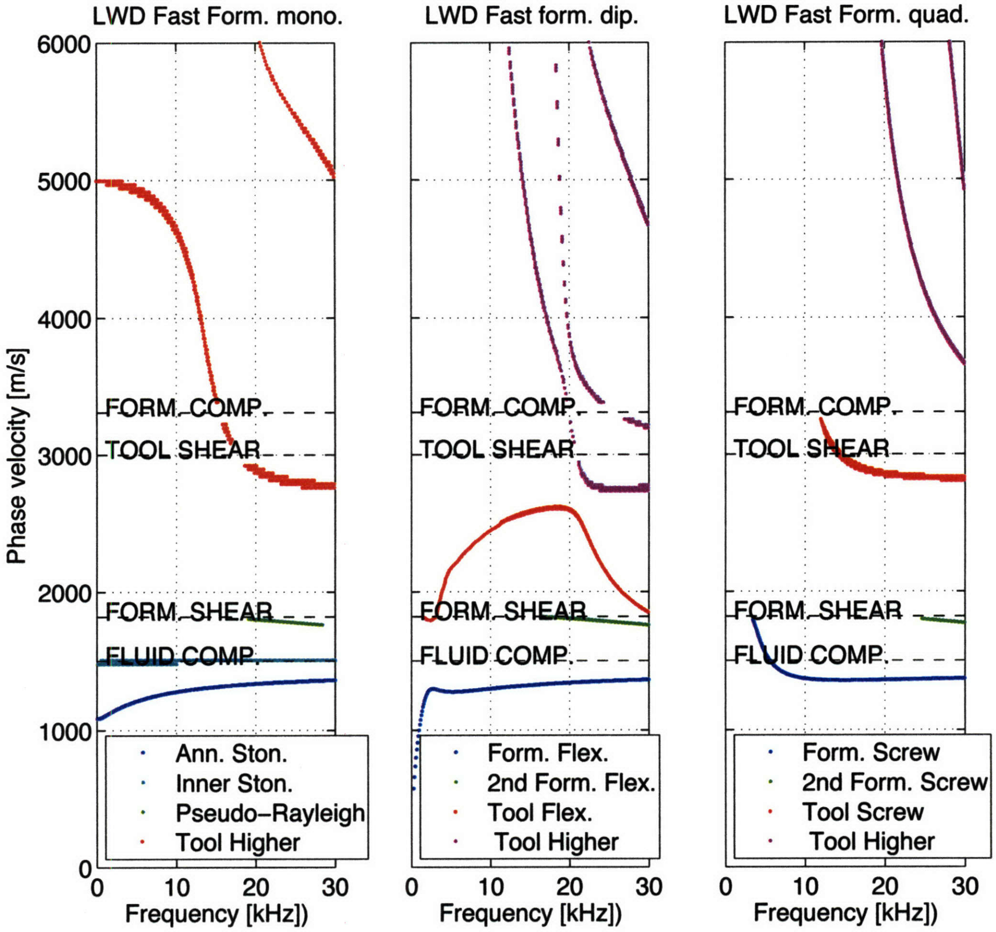

Figure 2-4: LWD monopole and Dipole in a fast isotropic formation, full modal interactions

LWD: slow formation, monopole, dipole and quadrupole

In the slow formation only the lowest order radial modes exist and therefore there is no equivalent pseudo-Rayleigh mode or higher order flexural and screw modes in the soft formation. Figure 2-6 shows all the monopole and dipole modes associated with the LWD tool in a slow formation and figure 2-7 shows an enlarged plot of the modes of interest to formation shear velocity evaluation. They are very similar to those seen in the fast formation examples in section 2.3.2 but are at lower phase velocities due

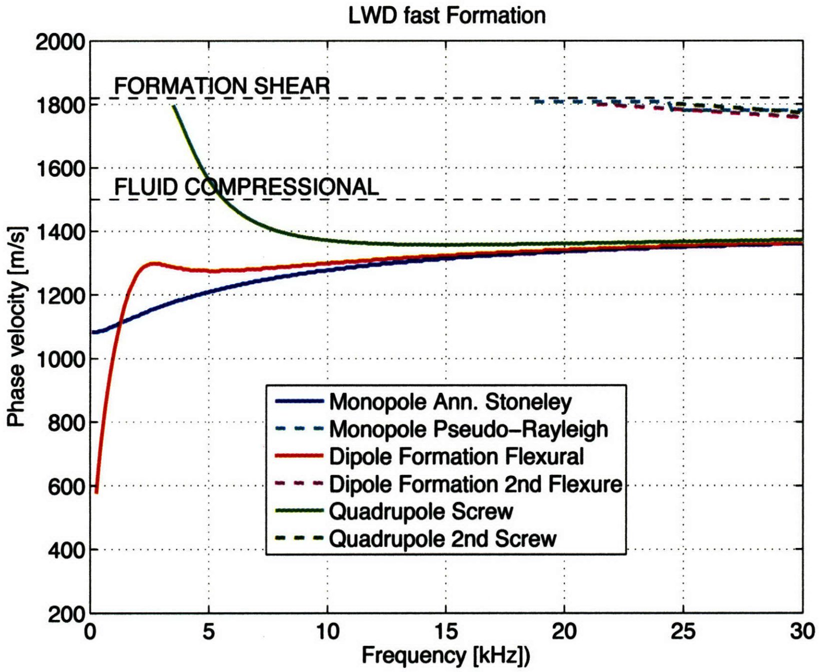

Figure 2-5: LWD monopole and Dipole in a fast isotropic formation, close up modes influenced by formation shear velocity

to the change in formation parameters.

2.4 Velocity processing methods

Understanding how the phase velocities of the modes changes with frequency is important to extract compressional and shear velocities from the data. However, the waveforms measured by the array of receivers contain contributions from several excited modes, so that interpreting this data is not necessarily straightforward. There are two main methods for extracting velocities from the recorded waveforms: time-domain methods and frequency-domain methods. Time-domain methods have the advantage of being fast, robust, and simple to program, however they are only truly accurate for non-dispersive modes. To account for dispersion, corrections to the time-domain data can be applied, but these corrections are not always accurate. These corrections work best with data that has a narrow range in frequency, so that substantial filtering of the data is often necessary. Frequency-domain methods are ideally

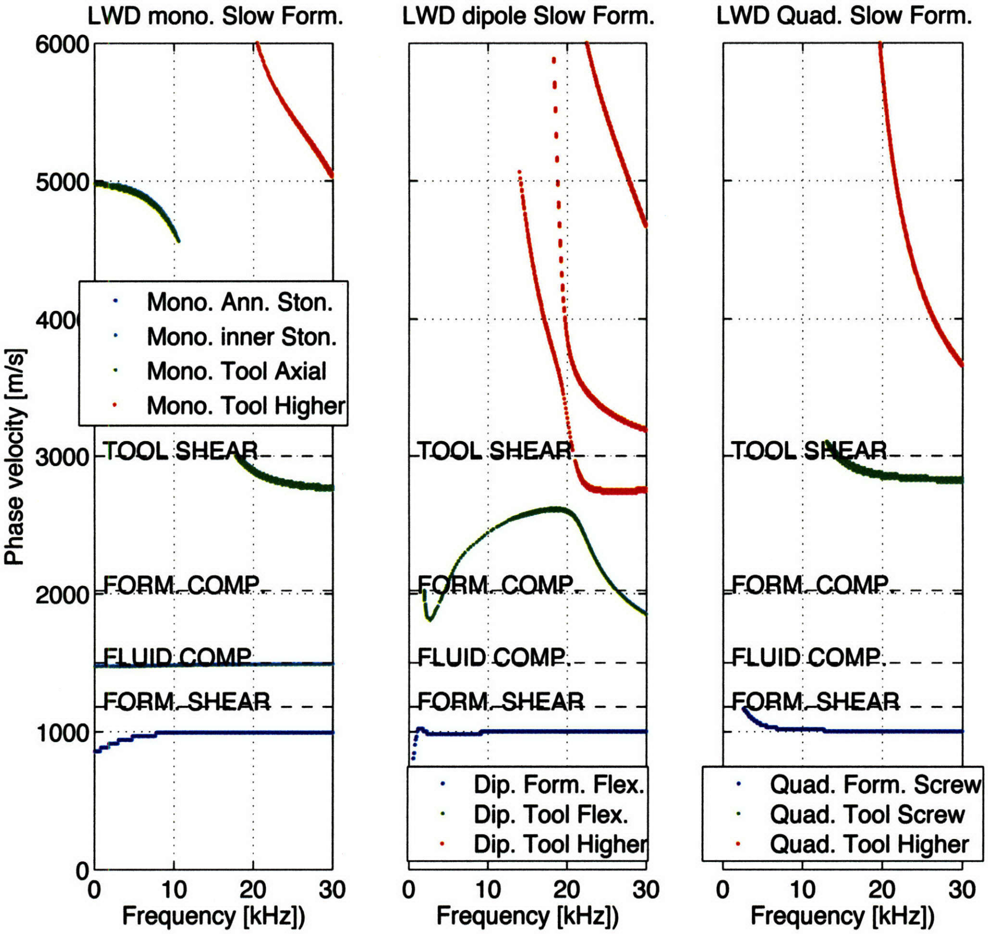

Figure 2-6: LWD monopole and Dipole in a slow isotropic formation, full modal interactions

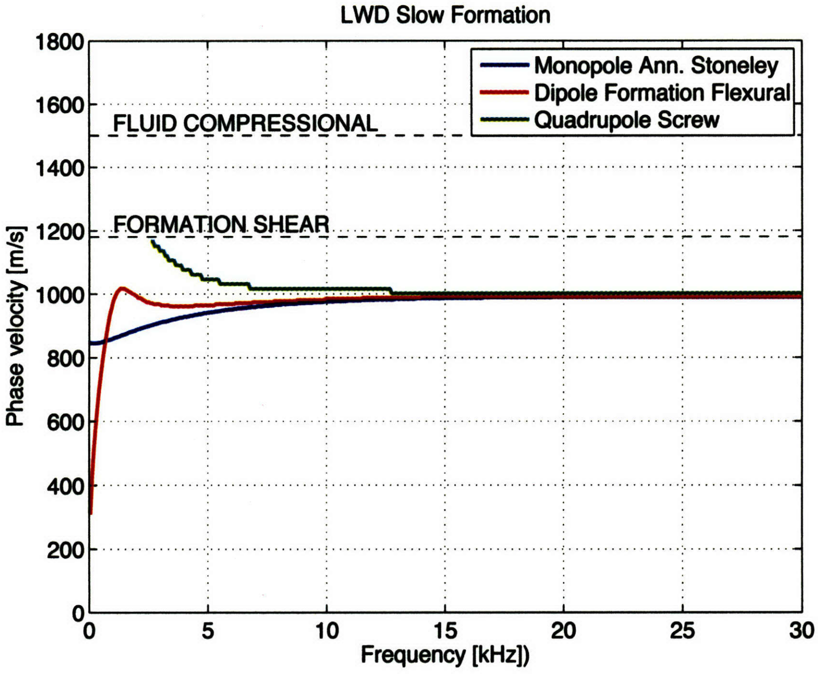

Figure 2-7: LWD monopole and Dipole in a slow isotropic formation, close up modes influenced by formation shear velocity

suited for dispersion curve analysis but are computationally expensive and require careful interpretation.

2.4.1 Time-domain methods

The very first acoustic logging tools used in the industry had only two receivers and formation velocities were estimated by knowing the distance between receivers and the time-difference between first arrivals. This simplistic method is highly effective for the first break compressional arrival with a high signal to noise ratio. Shear velocities are very hard to estimate using this method as the shear arrival is obscured by the initial compressional arrival in the seismic coda. Modern tools have an array of receivers and time-domain semblance methods are used to extract formation velocities Kimball and Marzetta (1984). These methods still work best if each seismic arrival is isolated from the waveform before processing. This can be achieved by filtering either in the time or frequency-domain. Isolating the correct arrival requires detailed understanding of the waveforms.

2.4.2 Frequency-domain methods

The advantage of frequency-domain methods is that they extract the full dispersion curve over the range of frequencies excited by the tool. This helps not only to determine what arrivals are present in the data, but also allows one to pick the correct formation velocities for dispersive modes. Frequency-domain methods can be divided into two types of analysis: model-based analysis and data-based analysis. Model-base analysis such as Prony's method fit an assumed model to the data. They are only truly effective if the correct model is used, for example, in Prony's method an exponential functional form is assumed for the propagation function from one spatial point to another corresponding to a single mode. One then chooses the number of modes to include in fitting this model to the data, so that the number of modes relevant to the interpretation is key and is not derived from the data but rather assumed at the outset.

Data-based approaches such as frequency-semblance methods do not assume an underlying model but rather directly lead to estimates of the compressional and shear velocities from the data. However these methods are very sensitive to noise present in the data, and require expert interpretation so that spurious results due to noise contaminating the data are not mistaken as actual formation velocities.

Chapter 3

LWD and wireline data comparison and analysis

3.1 Introduction

The high cost of operations during oil exploration requires that borehole measurements be made not only accurately but also as quickly as possible. In recent years this has meant a shift from traditional wireline tools, which operate only after a well has been drilled, to newer LWD (logging while drilling) or MWD (measurements while drilling) tools. The sonic logging tools are one class of tool which have been developed to operate in this manner. While the basic characteristics of both the wireline and LWD tools remain similar, there are differences in tool design and measurement methods that must be considered when interpreting their respective waveforms. The LWD tools typically have a larger diameter than the wireline and therefore reducing the annulus between the tool and formation. Each tool is designed to operate in specific frequency ranges to maximize certain modal responses and this must also be considered when extracting velocities. Additionally the offset between the source and first receiver in the LWD tool is approximately half of the offset in its wireline counterpart. This is important when logging in very fast formations (Vp>4 kms^{-1}) as modal arrivals may not be well separated.

Other differences include transducer design and damping mechanisms, used to reduce noise traveling along the tool. In Chapter 2 we discussed the mode shapes of the respective tools and saw how the geometry of the tool and the formation properties affect the measurement. It is obvious from the modes that, depending on the formation, we cannot necessarily directly compare velocity picks between tools without accounting for modal dispersion. Table 3.1 shows which arrival is used to estimate compressional and shear velocities for the wireline and LWD tools and what frequency ranges and source-receiver offsets are typically used.

The aim of this chapter is to compare velocity analyses, as calculated from LWD and wireline waveforms in the same borehole. An independent study of the formation velocities, as measured by each of the tools, will give a better understanding of their respective capabilities and show what methods are appropriate for extracting formation velocities. The analysis here is further complicated by radially non-homogeneous formations which cause dispersion in head waves and increase or decrease the dispersive characteristics in the normally dispersive modes. These issues are addressed by modeling the effects of a radial velocity gradient for each tool and comparing it with signatures seen in the data. While there is a body of work documenting waveform processing for both tools in homogeneous and non-homogeneous formations, there have been few studies that document comparisons of the two tools, Boonen and Tepper (1998). LWD sonic data analyses, without a wireline comparison, have been published by Goldberg et al. (2003), Tang et al. (2002) and Market et al. (2002) and sonic wireline published works include Chen (1988), Winbow (1988),Brie and Saiki (1996) and Huang (2003). Radially varying formations for the wireline case have been studied by Chan and Tsang (1983), Baker (1984)and Schmitt (1988a).

In sections 3.2 and 3.3 we compare the compressional and shear speeds as calculated by time and frequency semblance algorithms for the data set. Using modeling techniques, section 3.4 looks at the effects of tool frequency ranges and geometry on the measurement penetration into the formation. Section 3.5 shows markers in the

	Wireline	Logging While Drilling LWD
Source-Receiver Offset	3.35m (11ft)	1.37m (4.5ft)
Compressional Velocity	Estimated from a head wave i.e. direct compressional speed frequency range 15-30 kHz	Estimated from a head wave i.e. direct compressional speed frequency range 12-15 kHz
Shear Velocity	Estimated from a slightly dispersive arrival which assymptotes to formation shear velocity at low frequency frequency range 80Hz-5kHz	Estimated from a head wave in fast formations and a dispersive modal arrival, to which a correction must be added, in slow formations frequency range 5-8kHz

Table 3.1: Overview of methods velocity extraction, the tool frequency range and source-receiver offset for Wireline and LWD data used in this chapter.

data set that are a result of the tool measurement depth and the chapter summary is in section 3.6.

3.2 Standard velocity processing of the data using time semblance (STC)

Our data set consists of both LWD and wireline data collected over the same interval in the same well. At each depth the tool source excites an acoustic response from the formation and an array or receivers along the tool records the result. Depending on the sampling rate and type of measurement made the waveforms are typically 5-40 microseconds long. It is these waveform arrays that are then processed at each depth to estimate formation speed. This is known as full waveform logging as the entire wavetrain can be used in the processing, although typically the shear, compressional and modal arrivals are separated out and analyzed individually by looking at certain speeds and arrival time ranges. There are both monopole and dipole logs measured by the wireline tool and dipole logs from the LWD tool. The wireline data was collected, before the well was cased, approximately ten days after the drilling was completed. It should be noted that all the tool dimensions and source frequency ranges used in this chapter are for the two particular tools used in this data set.

To extract the pertinent formation velocity using time domain methods, the waveforms are filtered in a certain frequency band and semblance time coherence, STC Kimball and Marzetta (1984), is used to calculate the velocities at which there is coherent energy across the array. This analysis is performed at each depth to give a log of formation velocities. Before comparing the formation shear and compressional velocities from each tool it is important to qualify which modes are present in the data, and how waveform processing extracts the velocities, as summarized in table 3.1. Figure 3-1 shows some typical waveforms as measured by the wireline tool using a dipole source.

For the compressional measurement, the wireline used in this data set uses a monopole source operating between 8 and 20 kHz and the LWD tool, for this data set, uses a dipole source between 12 and 15 kHz. Both tools aim to measure the compressional head wave which is assumed to be non-dispersive, meaning that the calculated speeds are the formation compression velocities and no further processing of the data is needed.

For the formation shear measurement, both tools use a dipole source to excite the borehole flexural mode. This mode can be measured in both fast and slow formations, unlike the shear head wave which is only recorded in a fast formation. The wireline

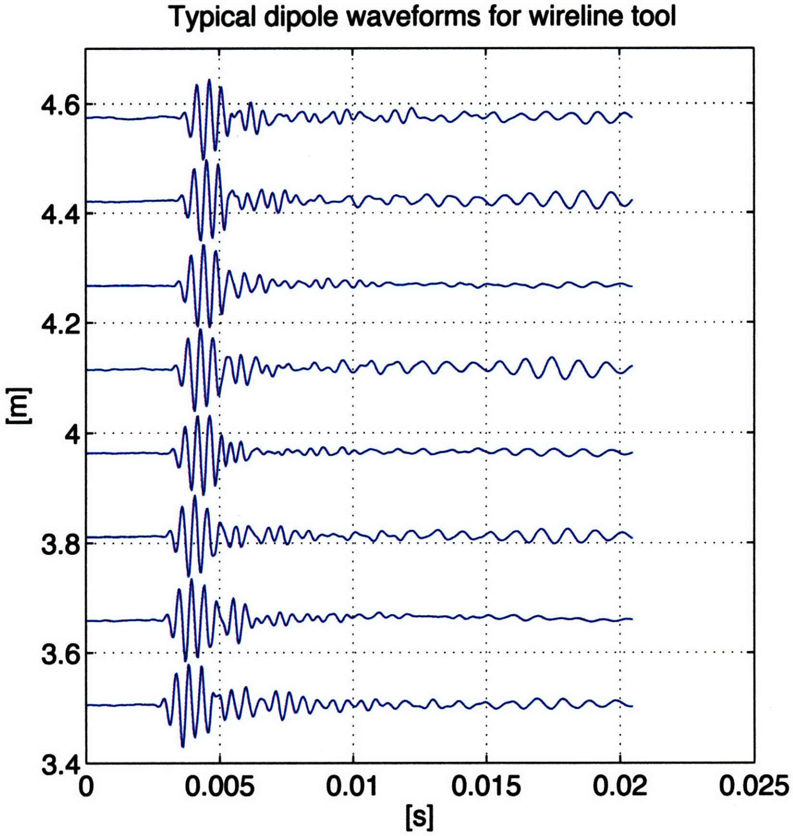

Figure 3-1: Typical dipole waveforms as measured by a wireline tool

tool operates between 80Hz and 5 kHz and the LWD tool between 3 and 8 kHz. The borehole flexural mode is dispersive and consistently asymptotes to the shear wave velocity at low frequencies for the wireline case. For the LWD geometry the small annulus between the tool and borehole wall cause the frequency band where the mode is most dispersive to shift to lower frequencies than its wireline counterpart where noise from circulation of drilling mud is also present. Additionally the tool flexural mode interacts with the borehole flexural mode at low frequencies causing it to tend to much lower velocities than the formation shear speed, as seen in chapters 2 and 4. Using the LWD data between 5 and 8 kHz excludes the noise from mud circulation and ensures that the tool flexural modes is not interacting with the borehole flexural mode, but means a velocity correction must be made to account for the lower modal shear speed in this frequency range. This correction is taken from forward modeling based on the formation density and compressional velocity, the size of the borehole, borehole fluid properties and the dispersed shear velocity picked from the flexural mode.

In the following sections 3.2.1 and 3.2.2 we show the formation shear and compressional speeds as calculated by the service provider using standard industry STC processing. It should be noted that we were able to reproduce this result with very good agreement ($< 2\%$) using the same methods. Figure 3-2 shows the gama ray and caliper measurements over the same interval. We can see from the caliper that the borehole diameter is fairly consistent throughout the log, except at the very top and bottom of the log. Large variations in borehole size can lead to erroneous velocity estimations in frequency domain processing as the diameter of the borehole determines the cutoff frequency of the higher order modes and affects the frequency range of greatest dispersion. If one assumes a constant borehole diameter it is sufficient to pick one band of frequency for the velocity pick. If however there is great variation in borehole diameter it may shift the frequency band where the interpretation is most accurate. The caliper here shows a difference of the order of 1cm which is not large enough to be of concern when processing the data. The gamma ray log is useful to determine changes in lithology over the length of the borehole. We can see from the correlation between the velocity and gamma ray logs that the changes in velocity are lithologically driven. The gamma ray indicates that the formation is a shaley sand, with the cleanest sands around 6000 ft (zone A) .

3.2.1 Shear Velocities from Data Set

The wireline tool has two arrays of receivers placed orthogonally on the tool, referred to as the upper and lower arrays. These arrays give two formation velocity measurements 90^o apart azimuthally. If the tool is operating optimally and the data quality is good, the differences between the velocities measured by the orthogonal receivers can be attributed to either borehole ellipticity/irregularity or formation anisotropy. The difference between the upper and lower dipole measurements can be seen in figure 3-3. Assuming the borehole is circular, the formation appears to be mostly isotropic to slightly anisotropic ($< 2\%$) with the exception of the zone between depths x6000 and x6200 ft where there are a few outliers around 10%. This is an important consideration when comparing the LWD and wireline tools as the they turn while descending/ascending the borehole, and take the acoustic measurements regardless of azimuthal orientation. When comparing between tools, we consider areas where the percentage difference between the velocity measurements are larger than the difference between the upper and lower dipole measurements. This is to avoid formation anisotropy being the largest component in the velocity differences. If we consider that the LWD measurement can be either greater, less than or the same as the wireline measurement we can see all three types of bias in the data. The larger singular differences between the two measurements are likely due to mismatching in depths of the tools measurements. The rate at which the borehole is drilled is not constant and so the LWD takes measurements as a function of time. This leads to uneven spatial sampling along the borehole. Conversely, wireline tools take measurements as a function of depth and so are evenly sampled along the z-axis. For the purposes of calculating the difference between the two logs the LWD data was interpolated to

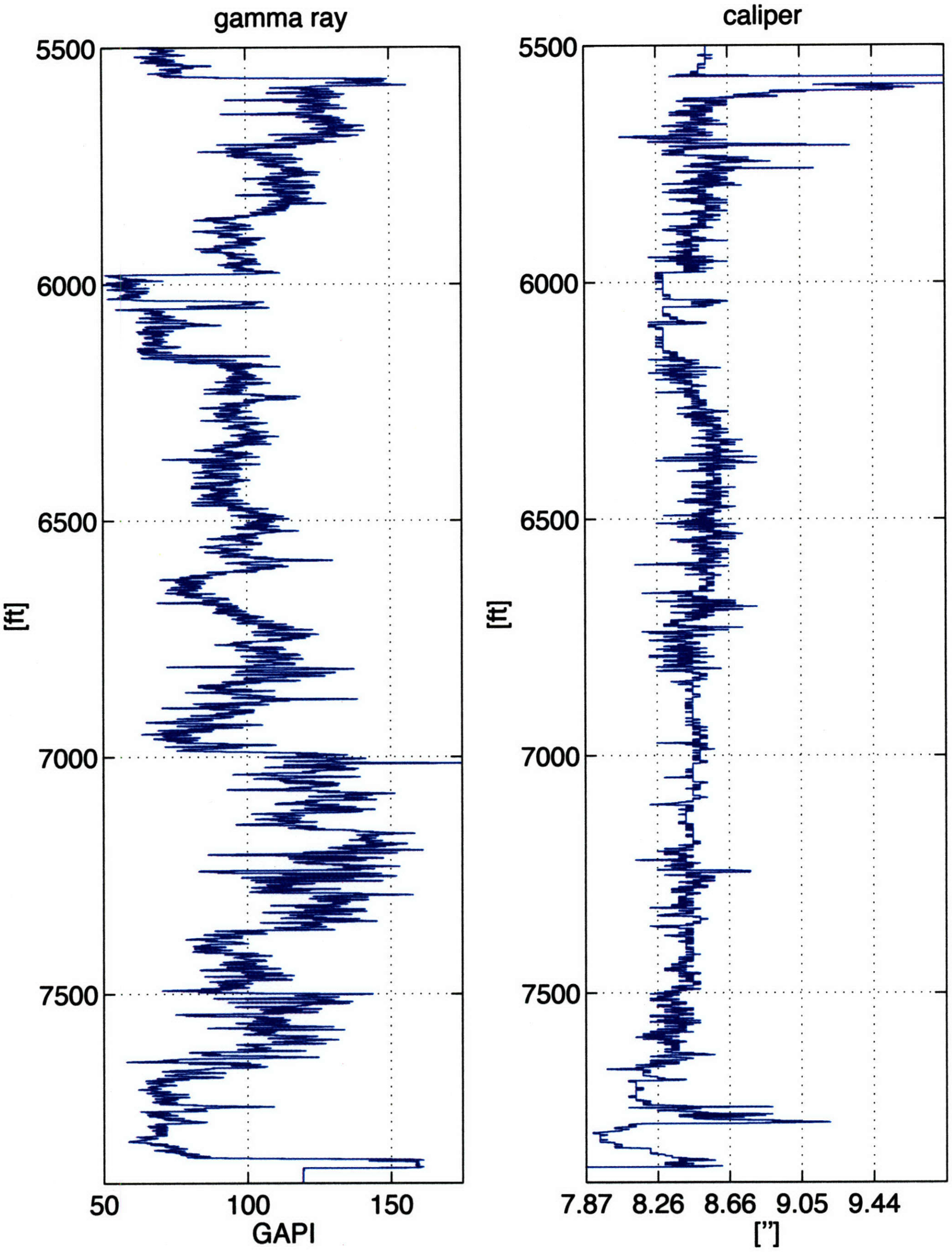

Figure 3-2: Gamma ray and caliper measurements.

have samples at the same depths as the wireline, which can lead to the large spikes seen in the right hand plot.

The zone between x6000 ft and x6200 ft shows the LWD is measuring velocities slower than the wireline. The zones above and below this region at x5500 ft to x6000 ft and x6200 ft to x6500 ft show the LWD measuring velocities faster than the wireline. Lastly the zone below x7100ft shows the LWD and wireline to be closer in velocity estimation. For the first zone, x6000 ft, the degree of anisotropy approaches the differences measured by the two tools but for the rest of the zones, the anisotropy estimated from the difference between upper and lower dipole cannot account for the discrepancies. For the remainder of the thesis we will refer to these regions as zones A, B and C, with zone A referring to data between x6015 and x6030 ft, zone B for data between x6390 and x6405 ft and zone C for data between x7090 and x7100ft.

3.2.2 Compressional Velocities from Data Set

The compressional velocities taken from time semblance picks can be seen in figure 3-4. The two measurements show similar profiles with some slight differences. Apart from spikes in the data due to depth mismatching the other, and more significant, difference between the two velocity profiles is a consistent bias of around 2.5% with the LWD tool measuring a slightly lower velocity. There was a 10 day delay between measurements and it it possible that some of the measured properties may have changed over this period due to fluid invasion, mudcake formation etc., referred to as alteration, Boonen and Tepper (1998). But the consistent bias along the log, that does not change with changes in formation, could suggest it is not related to formation properties.

Time lapse acoustic logs often show a difference in measurements, as pore and drilling mud fluid equilibrate down hole. This is especially problematic where shales are present as they can swell, altering both the geometry of the borehole and the acoustic properties, Blakeman (1982), Wu et al. (1993). Although alteration is a

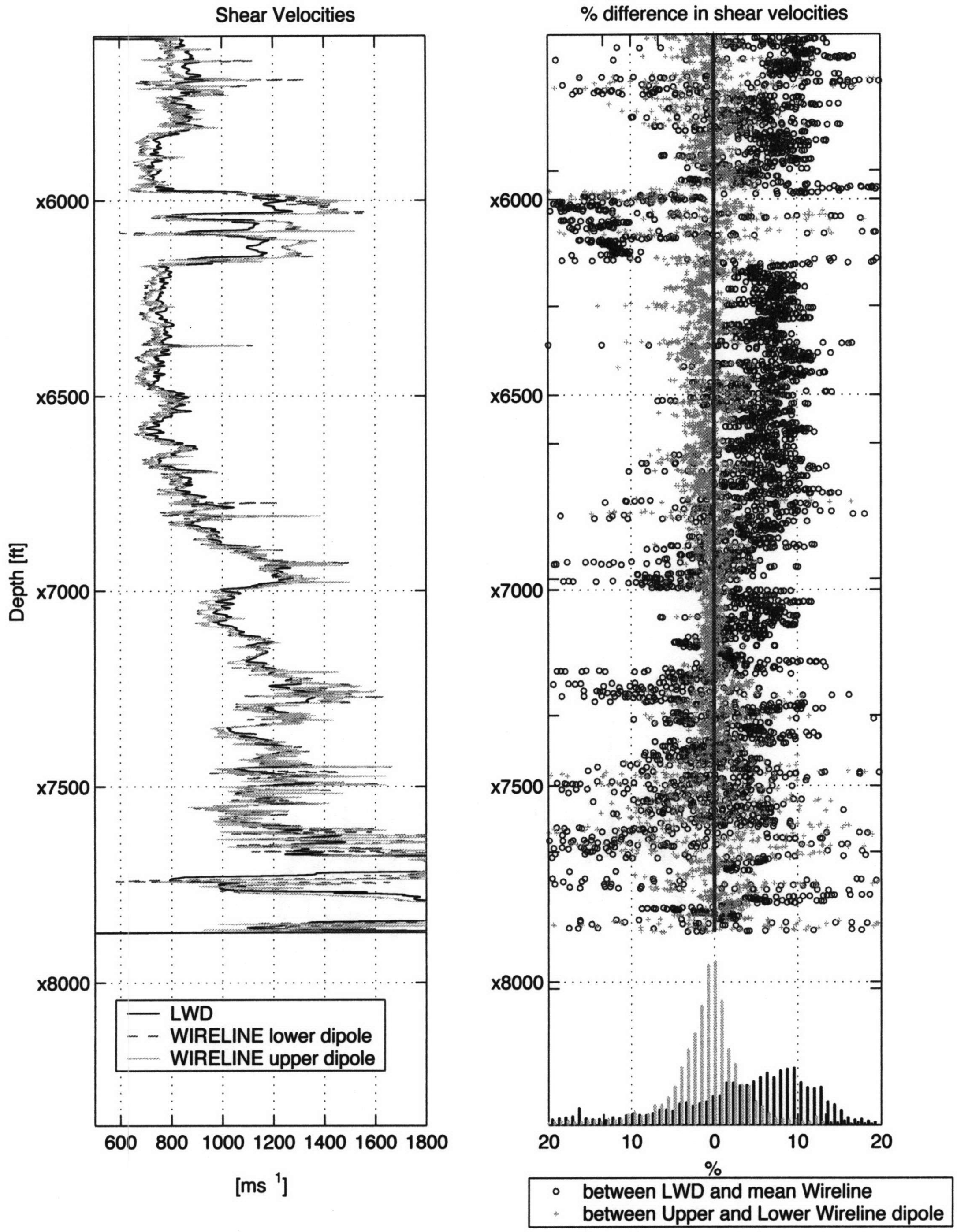

Figure 3-3: Shear velocities for Wireline and LWD data (calculated from time semblance), percent difference between wireline and LWD velocities (LWD-Wireleine), and percent difference between LWD upper and lower dipoles (upper-lower). The histograms on the right hand side show the percentage distribution of the difference between the LWD and wireline shear velocities picked from time semblance (dark) and, the percentage distribution of the difference in velocities as measured by the upper and lower wireline dipoles (light). Note the shift of bias from LWD measuring a slower velocity at x6000 ft, to the LWD measuring a faster velocity between x6200 ft, and x7100 ft and a mean bias of zero below x7100ft. (LWD is the reference)

possible scenario which can account for the small discrepancies in velocities, it seems unlikely the whole formation would produce a similar bias. If the bias was due to alteration, and thus formation related, one would expect to see the difference between the logs vary less uniformly as a function of depth. The peak of the distribution of the velocity differences are similar to those between the lower and upper dipole shear measurements, but the distribution has a larger variance indicating that there are regions where the tool velocity differences are greater than those attributable to formation anisotropy and therefore are the result of another mechanism.

3.3 Processing waveforms using a frequency semblance approach and comparing with time semblance results

Industry's preferred method of velocity analysis is semblance time coherence (STC) because it is fast, robust and needs very little input from the interpreter. The algorithm relies on a uniform event move-out in the waveforms, and is therefore accurate for non-dispersive to slightly dispersive modes. It could however, give erroneous results for dispersive waveforms. This issue is usually overcome by filtering the data in a narrow frequency band before the semblance processing and then correcting the velocity pick from forward modeling. This correction is sufficient if the mode is well understood, but as we will see later in this chapter, there are many parameters which can alter the shape of a mode making standard corrections difficult to calculate accurately.

One way around this problem is to perform the semblance calculation in frequency rather than time. A full frequency semblance allows us to plot the phase velocity as a function of excited frequencies, giving more information about the mode and consequently formation properties. The downside to extracting the full mode is that it is computationally expensive and the result is harder to interpret. There is no quick

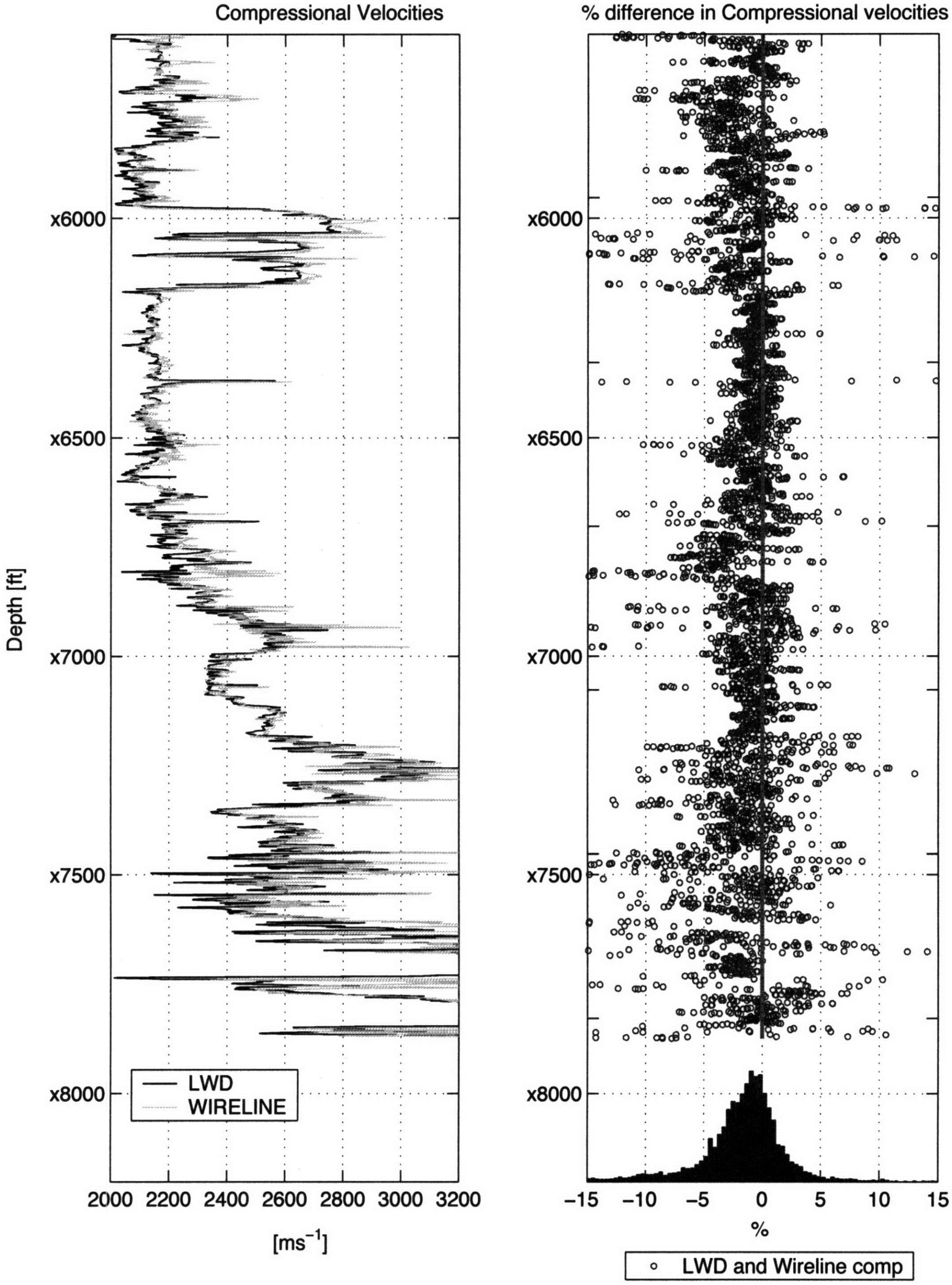

Figure 3-4: Compressional velocities for Wireline and LWD data and percent difference between wireline and LWD velocities, as calculated from time semblance processing. The histogram on the histogram on the right plot shows the percentage distribution of the difference between the wireline and LWD velocity picks. (LWD is the reference)

algorithm to pick the correct phase velocity and each plot must be interpreted individually. While this method is currently unsuitable for large amounts of data it can be a useful interpretation tool if performed at a few key depths. The algorithm used in this paper to extract the frequency semblance log is described in Rao (2005).

The uncertainty associated with these methods can be quite large depending on the spread of the coherent region on the semblance figure. For completely undispersed noise free wave forms the time semblance result is well defined. The presence of noise or dispersion causes a spread of the coherence in semblance space, therefore increasing the uncertainty of the velocities.

We have isolated three zones of interest from the velocity logs picked from time semblance, centered around x6026 ft, x6400 ft and x7100 ft, zones A, B and C. For each zone we reprocess some of the waveforms from using both time and frequency semblance analysis for both the compressional head wave and formation flexural mode.Figures 3-5 , 3-6, 3-7 , 3-8, 3-9 and 3-10 show the compressional and shear velocity picks from reprocessed data in zones A, B and C both in time and frequency. In these plots the both the LWD and wireline data are shown and a distribution of the differences between the velocity estimations are shown as a histogram in the lower portion of the plot. It can be seen for most of the data that the mean difference between the two measurements is reduced when the frequency processing is used. Figures 3-11, 3-12 and 3-13 show semblance plots from one depth within each of the zones. It should be noted however that the discrepancies between the measurements fall into the region of uncertainty as given by the coherent semblance blobs seen in figures 3-11 to 3-16 suggesting that any difference between the two velocity estimations can be accounted for by the uncertainty inherent to processing methods. While we do not discount that the measurements overlap in the region of uncertainty in some of the zones, we still believe that the physical tool properties play a significant role in the depth of investigation. We therefore model cases consistent with the biases seen in the three reprocessed zones as the changes in velocities between the two processing methods are consistent.

From the modal analysis seen in chapter 2 and the knowledge that the refracted arrivals are non-dispersive we know what to anticipate for radially homogeneous formations. The discrepancies between the tool measurements in zones A, B and C indicate that the formation may not have the same radial velocity profile in all zones. This can be inferred by the different biases between the tool measurements in the three zones. We assume, and will go on to show in section 3.4, that the tools measurements penetrate into the the formation at differing radial depths. It is therefore important to understand the character of the formation radial velocity profile. The frequency and time semblance comparisons shown in this section are useful for two reasons. Firstly we see the difference in velocities as picked by the two methods and secondly we extract the full mode from the data, allowing us to see any deviation from a radially homogeneous model. Because the compressional refracted arrival, in hard formations, should be non-dipersive for the radially homogeneous case it is the easier arrival to analyze in terms of unexpected dispersion. The formation shear flexural mode is also affected by a radial velocity gradient in the formation but is harder to interpret as it is already a dispersive mode. The main objective of this section is to show the difference between the time and frequency semblance velocity picks saving the discussion of radial velocity profiles for the following section and referring to them here only qualitatively.

3.3.1 Compressional head wave in zones A, B and C, time and frequency semblance.

First we compare the wireline monopole at all three depths in the semblance plots, shown in figures 3-11, 3-12 and 3-13. Table 3.3.1 gives the time and frequency semblance picks for each of the three chosen depths. It is important to compare not only the difference between the time and frequency velocity picks for each tool but also to look at the change in bias for the tool measurements when processed with fre-

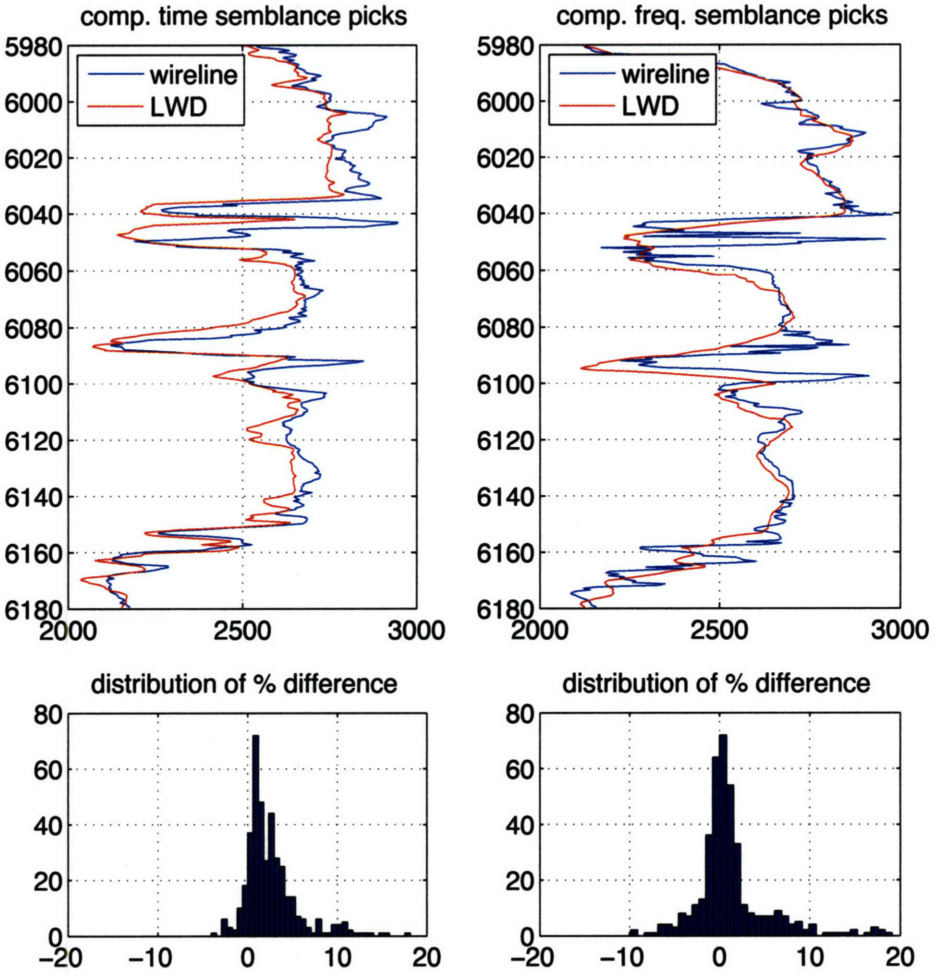

Figure 3-5: Time and frequency semblance compressional velocity picks for wireline and LWD data in zone A. The histograms represent the distribution of differences between the tools measurements with LWD used as the reference. The mean difference between the two tools velocity picks over the shown depths is given in the title of the historgram.

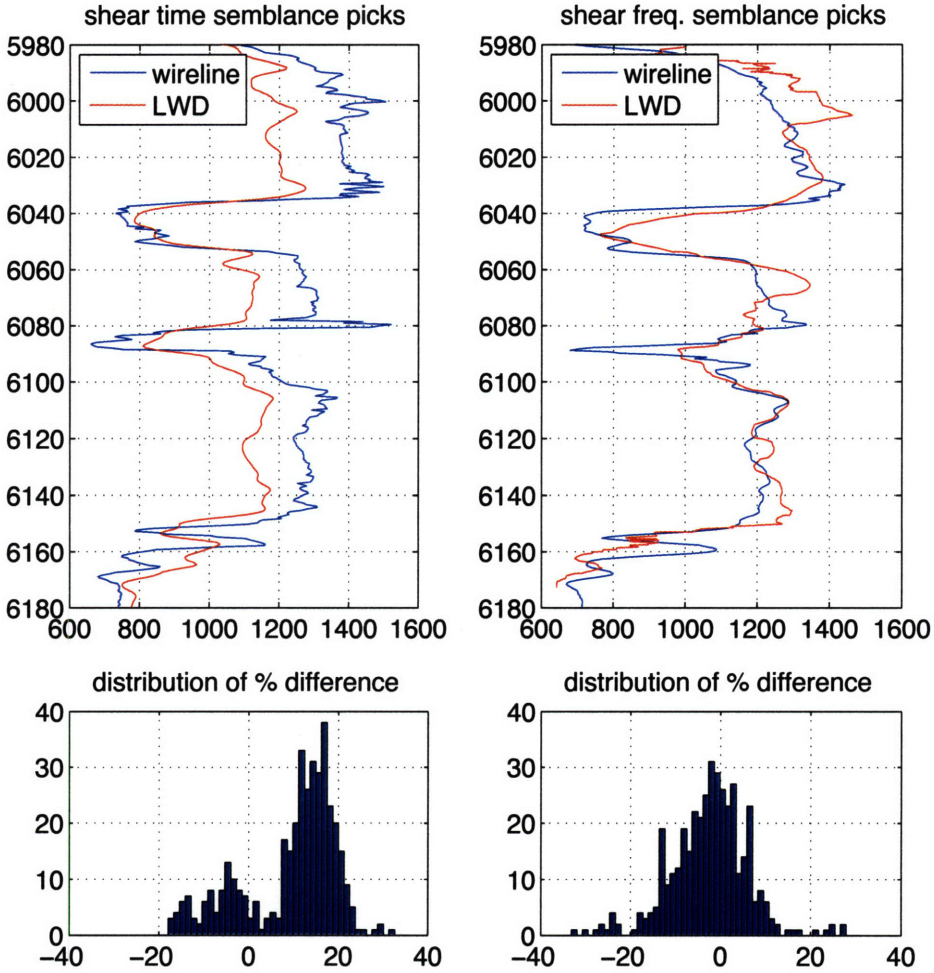

Figure 3-6: Time and frequency semblance shear velocity picks for wireline and LWD data in zone A. The histograms represent the distribution of differences between the measurements, with LWD used as the reference. The mean difference between the two velocity picks over the shown depths is given in the title of the historgram.

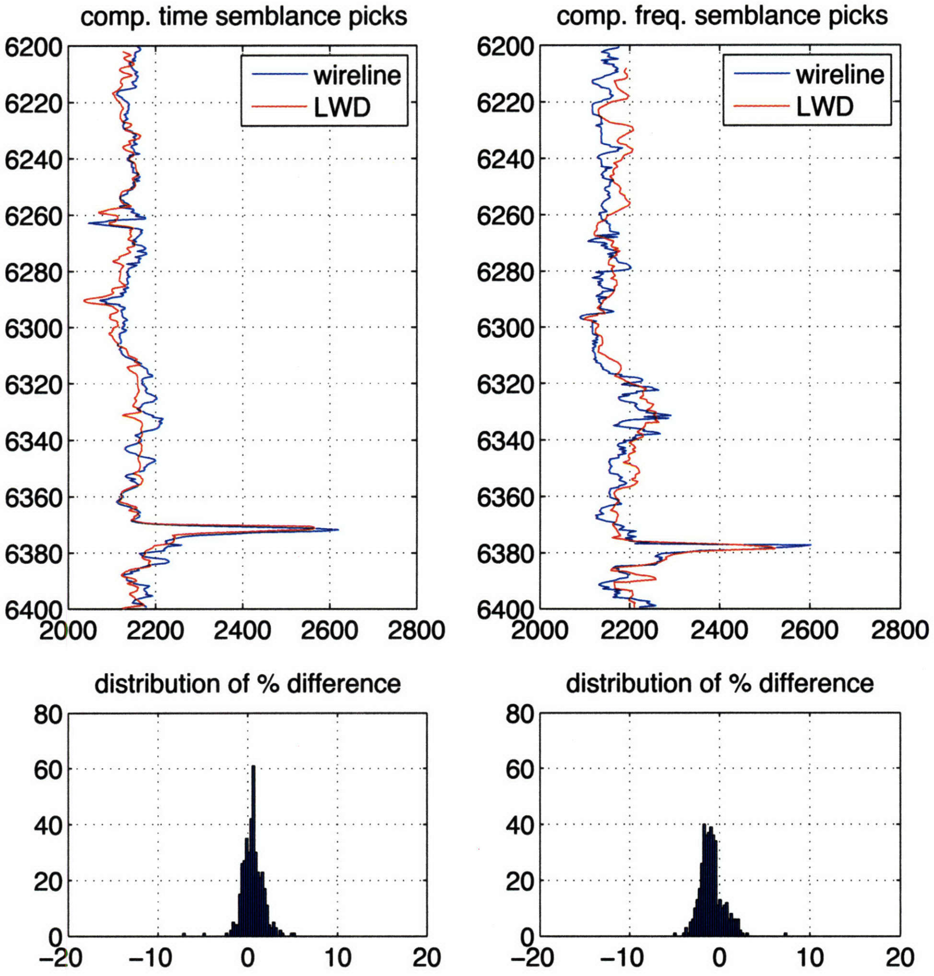

Figure 3-7: Time and frequency semblance compressional velocity picks for wireline and LWD data in zone B. The histograms represent the distribution of differences between the measurements, with LWD used as the reference.The mean difference between the two velocity picks over the shown depths is given in the title of the historgram.

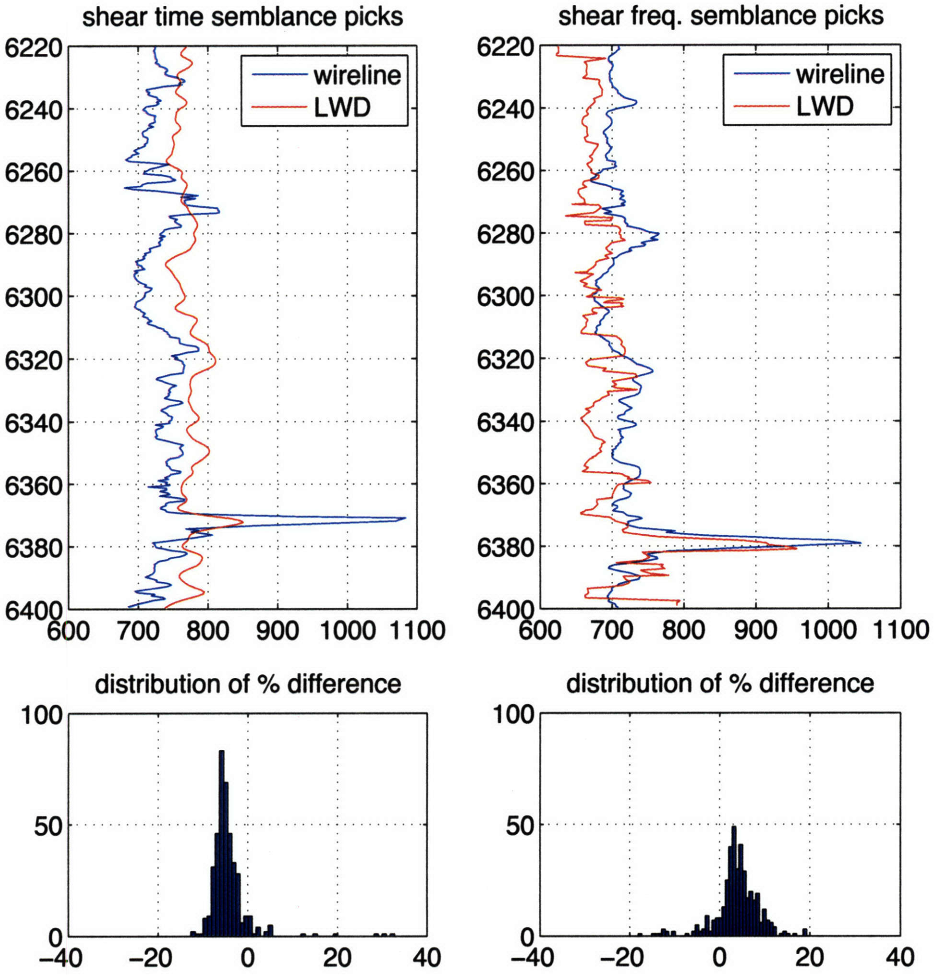

Figure 3-8: Time and frequency semblance shear velocity picks for wireline and LWD data in zone B. The histograms represent the distribution of differences between the measurements, with LWD used as the reference. The mean difference between the two velocity picks over the shown depths is given in the title of the historgram.

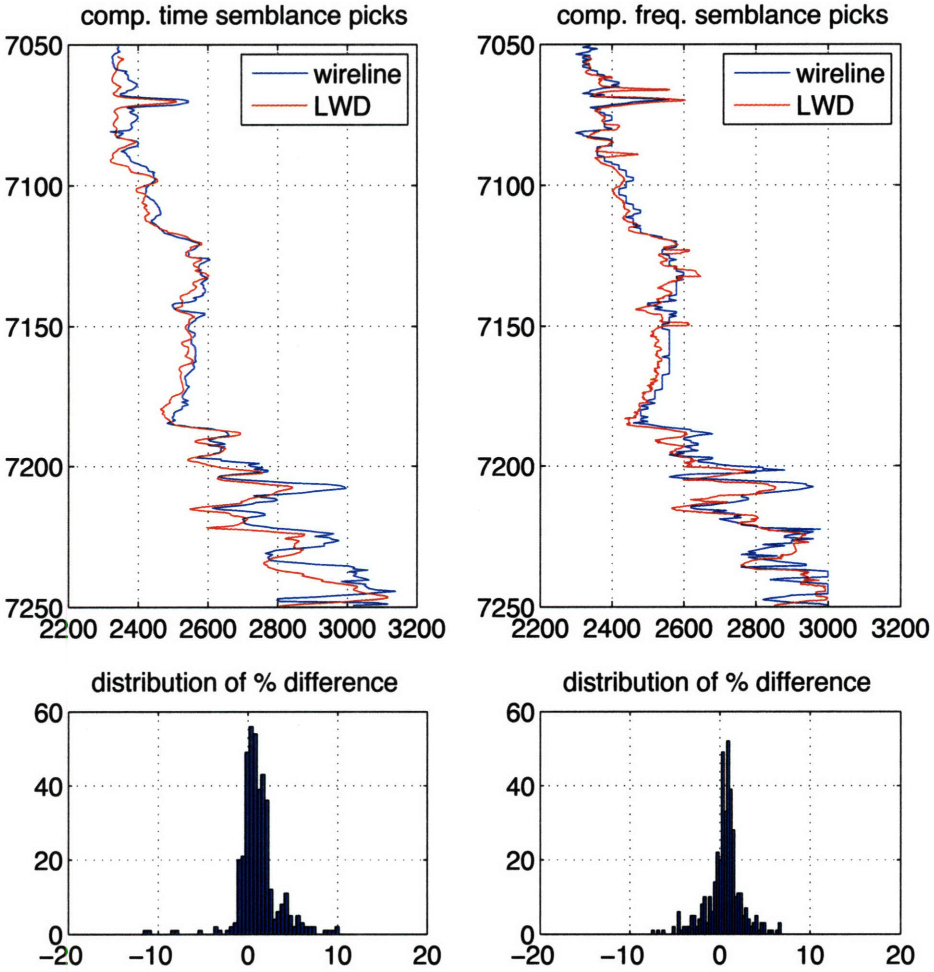

Figure 3-9: Time and frequency semblance compressional velocity picks for wireline and LWD data in zone C. The histograms represent the distribution of differences between the measurements, with LWD used as the reference. The mean difference between the two velocity picks over the shown depths is given in the title of the historgram.

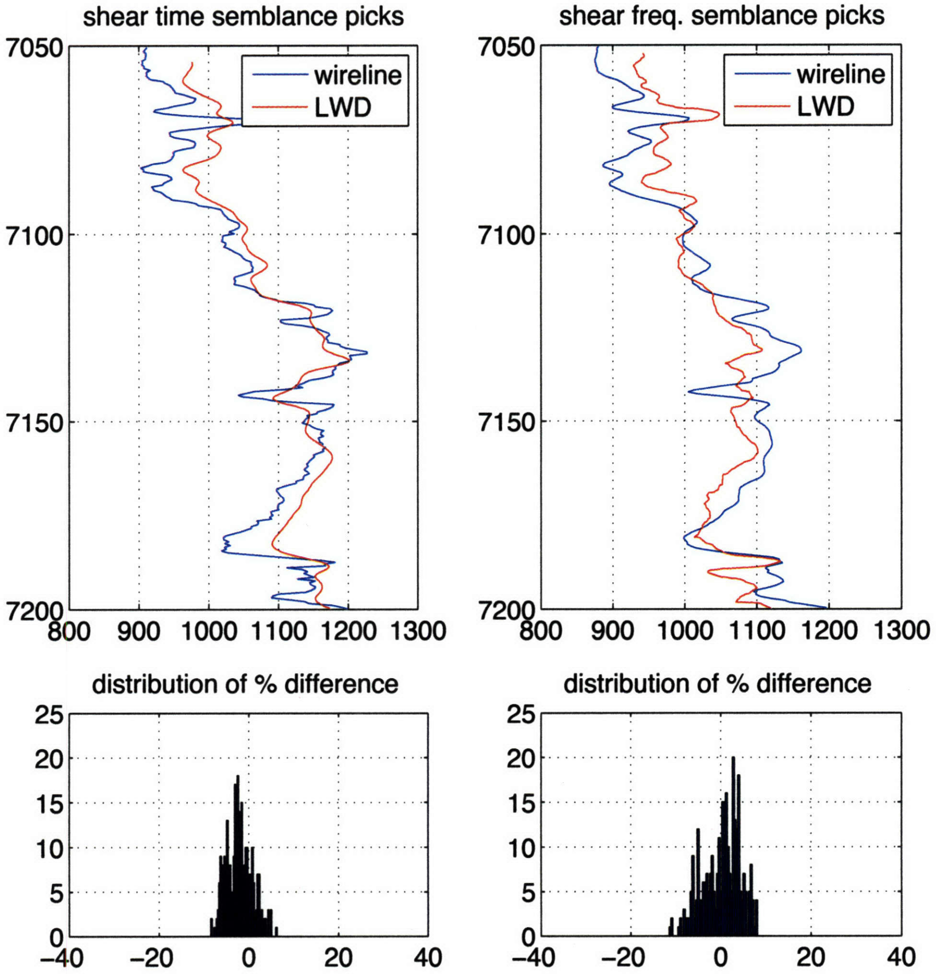

Figure 3-10: Time and frequency semblance shear velocity picks for wireline and LWD data in zone C. The histograms represent the distribution of differences between the measurements, with LWD used as the reference. The mean difference between the two velocity picks over the shown depths is given in the title of the historgram.

quency opposed to the time semblance. For example at x6026ft the LWD measured a slower velocity than the wireline when the time semblance velocity was calculated but with the frequency semblance method the LWD now measures a faster velocity. At x6400ft and x7100ft the bias does not change. This bias shift can also be seen at certain depths in the reprocessed sections in figures 3-5, 3-7 and 3-9.

We now compare the semblance plots qualitatively. For x6026 ft, the phase velocity for the compressional refracted mode increases very slightly with frequency, indeed this can also be seen on the time semblance as the second later arrival, although it is not quite so obvious. At x6400 ft we see the opposite behavior: the dispersion indicates that the higher frequencies are decreasing in phase velocity, this is again apparent on the time semblance, and a second small area of coherence can be seen at around 2 ms. This is typical of STC results when a dispersive waveform is present. At the third depth of x7100 ft, the mode appears to be constant in phase velocity, which is what is expected from the compressional head wave. Assuming that lower frequencies see further into the formation than high frequencies, the plots suggest that there is a fast to slow radial velocity gradient at x6026 ft, a slow to fast radial velocity gradient at x6400 ft and no radial velocity variation at x7100 ft. For the LWD high frequency dipole, which is also measuring the compressional refracted wave. The frequency plots show a similar trend to the wireline but they are not so pronounced. The time semblance, however do not show dispersion.

3.3.2 Formation flexural mode in zones A, B and C, time and frequency semblance.

The shear dipole flexural mode is somewhat more complicated to interpret. When the LWD tool is present the mode follows the shape of the tool mode at low frequencies.

	WIRELINE time pick [m/s]	WIRELINE freq. pick [m/s]	LWD time pick [m/s]	LWD freq. pick [m/s]	Formation radial velocity profile near → far
Zone A x6026ft	2833	2820	2783	2850	Fast → Slow
Zone B x6400ft	2180	2139	2150	2105	Slow → Fast
Zone C x7100ft	2450	2431	2442	2422	radially homogeneous

Table 3.2: Compressional Velocity. Comparison of time and frequency velocity semblance picks for LWD and wireline.

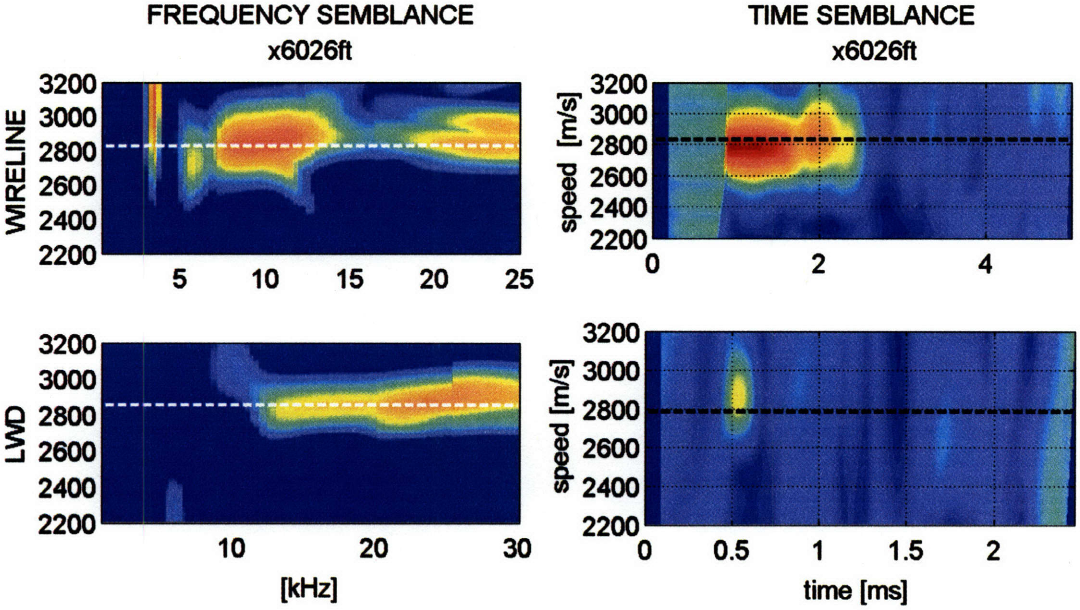

Figure 3-11: Compressional velocity picks in Zone A using frequency and Time semblance analysis. The wireline data are shown in the top row and the LWD in the bottom row. The white dashed lines on the left hand column indicate the compressional velocity as picked from frequency semblance. The black dashed lines on the right hand column denote the industry pick from time semblance.

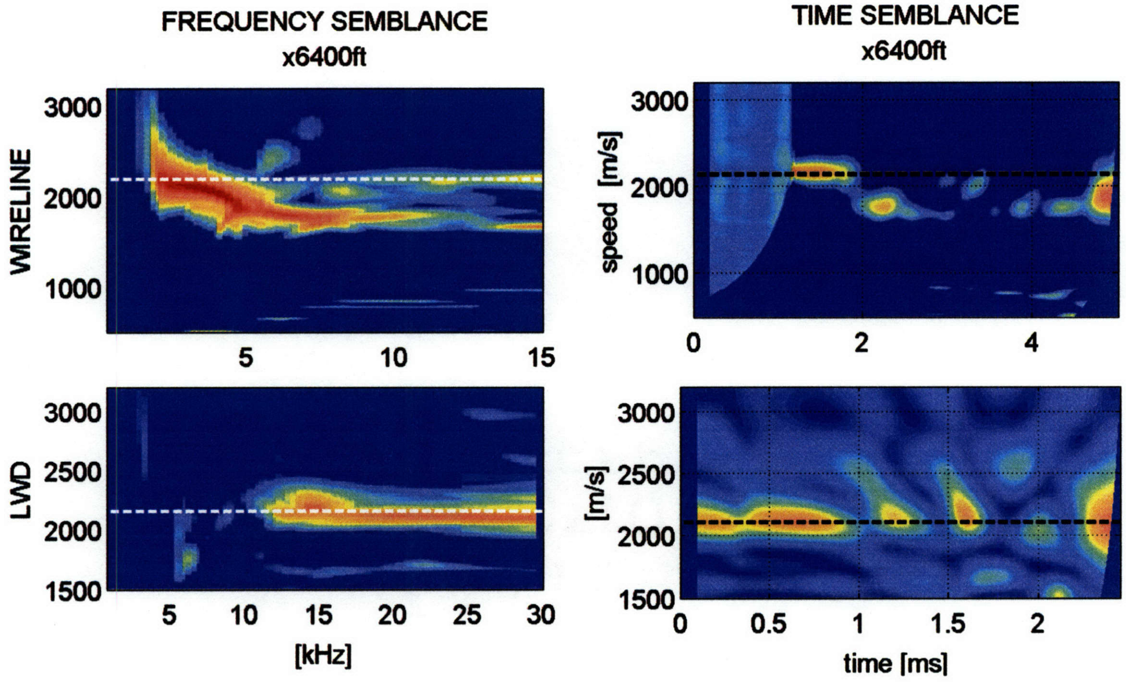

Figure 3-12: Compressional velocity picks in Zone B using frequency and Time semblance analysis. The wireline data are shown in the top row and the LWD in the bottom row. The white dashed lines on the left hand column indicate the compressional velocity as picked from frequency semblance. The black dashed lines on the right hand column denote the industry pick from time semblance.

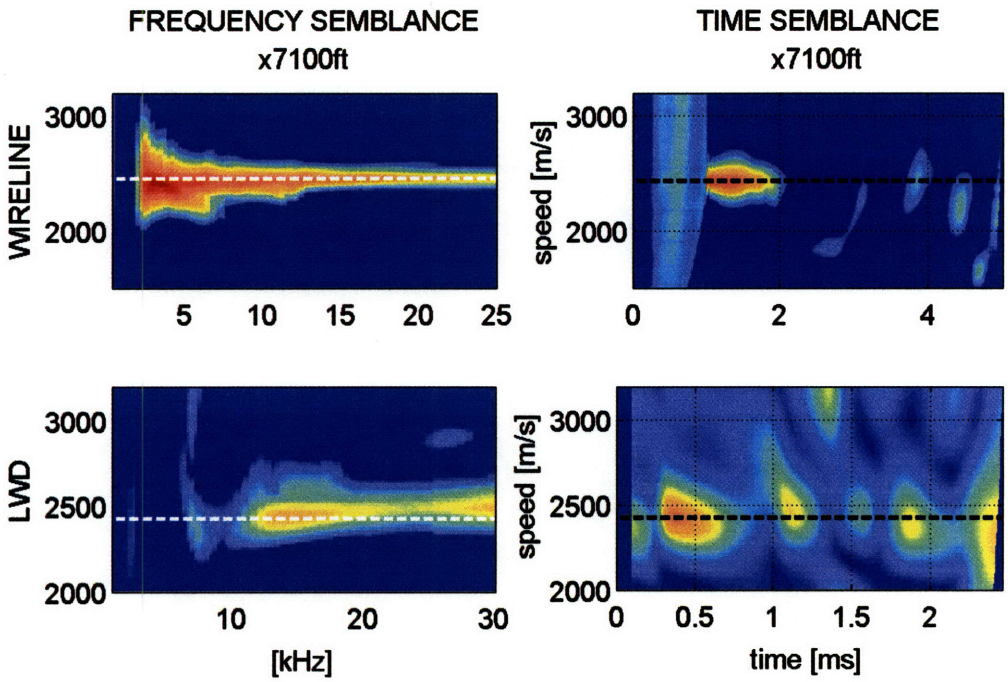

Figure 3-13: Compressional velocity picks in Zone C using frequency and Time semblance analysis. The wireline data are shown in the top row and the LWD in the bottom row. The white dashed lines on the left hand column indicate the compressional velocity as picked from frequency semblance. The black dashed lines on the right hand column denote the industry pick from time semblance.

	WIRELINE time pick [m/s]	WIRELINE freq. pick [m/s]	LWD time pick [m/s]	LWD freq. pick [m/s]	Formation radial velocity profile near → far
Zone A x6026ft	1350	1463	1430	1258	Fast → Slow
Zone B x6400ft	720	683	715	680	Slow → Fast
Zone C x7100ft	1026	1026	1017	1017	radially homogeneous

Table 3.3: Shear Velocity. Comparison of time and frequency velocity semblance picks for LWD and wireline.

Figures 3-14, 3-15 and 3-16, show the formation flexural mode in time and frequency semblance, for the three depths of interest, for both the wireline tool (top row) and LWD tool (bottom row). Table 3.3.2 shows the velocity picks for the two methods for the LWD and wireline data at the three depths of interest. Once again it is important to not the change of bias between the LWD and wireline measurement when the frequency semblance method is used for the data in zone A.

In the wireline frequency semblance figures (left hand side, top row), (figures 3-14, 3-15 and 3-16) the formation flexural mode for a homogeneous formation is overlain on the figure, it is the white solid line. Again, comparing across the depths, we can see for the wireline in zone A that the semblance plot indicates some radial velocity variation. Between 2 and 4 kHz the semblance indicates an increase in phase velocity which is not consistent with the dipole flexural mode, which should be flat in this region. In zone B the semblance shows the flexural mode behaving as expected but does not show any coherence above 4kHz.In zone C ft the semblance plot follows the overlain dipole flexural mode all the way out to 10 Khz and indicates that the formation is indeed homogeneous at this depth.

Lastly we qualitatively compare the LWD formation flexural mode across all three depths. This is the hardest plot to interpret due to the complicated interaction of dipole flexural and tool modes. The modal phase velocity was picked at 4Khz and a static correction (calculated from forward modeling) added, which gave a first estimate of the formation shear velocity. This formation velocity was then used to generate the dipole (white line), quadrupole (green line) and hexapole (black line) modes for a homogeneous case and these were then compared with the original semblance plot. The shear velocity was then adjusted and the modes of the homogeneous model re-calculated until a good fit was found. In zone A, figure 3-14, the dipole and hexapole modes were both excited. This can also be seen on the time semblance plot with two areas of coherence at 1 and 2 ms. This could cause confusion if a single velocity is to be picked from the time semblance as in the standard processing chain. In zone B, figure 3-15, the area of coherence is again diminished as it was in the wireline dipole case. Here it appears that the dipole and quadrupole have been excited. Lastly in zone C, the dipole appears to be the only excited mode, as can be clearly seen between 4 and 10 kHz. The time semblance is not easy to interpret, as it has two clear areas of coherence at different phase velocities. The excitation on the hexapole is somewhat unusual and may be caused by the tool not being centered in the borehole.

3.4 Depth of Investigation for wireline and LWD tools

Before we further compare the LWD and wireline logs with velocities picked from frequency semblance, we take a closer look at the effects on the waveforms of radial velocity gradients surrounding the borehole. From the initial analysis of the data seen in the last section we identified three scenarios, one of increasing velocity, one

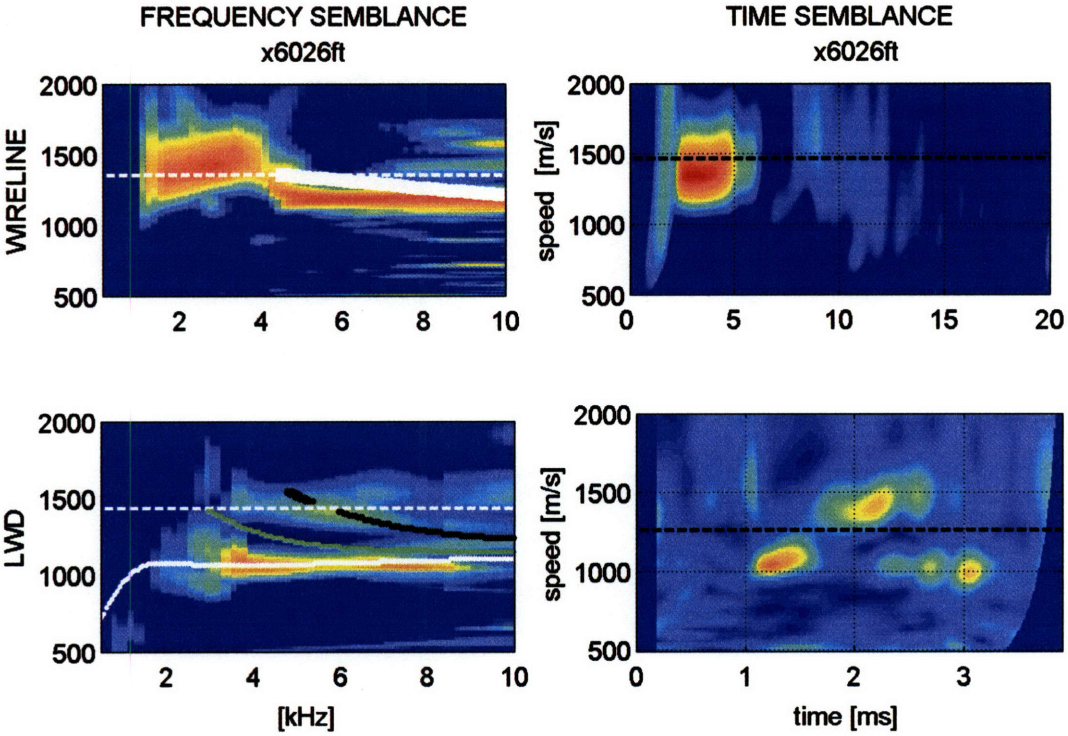

Figure 3-14: Shear velocity picks in Zone A using frequency and time semblance analysis. The wireline data are shown in the top row and the LWD in the bottom row. The white dashed lines on the left hand column indicate the shear or compressional velocity as picked from frequency semblance. The black dashed lines on the right hand column denote the industry pick from time semblance. The calculated modes for the appropriate tool are overlaid for the frequency semblance images in the dipole shear cases, the white solid line indicates the dipole mode, the green solid line indicates the quadrupole mode and the black line the hexapole mode.

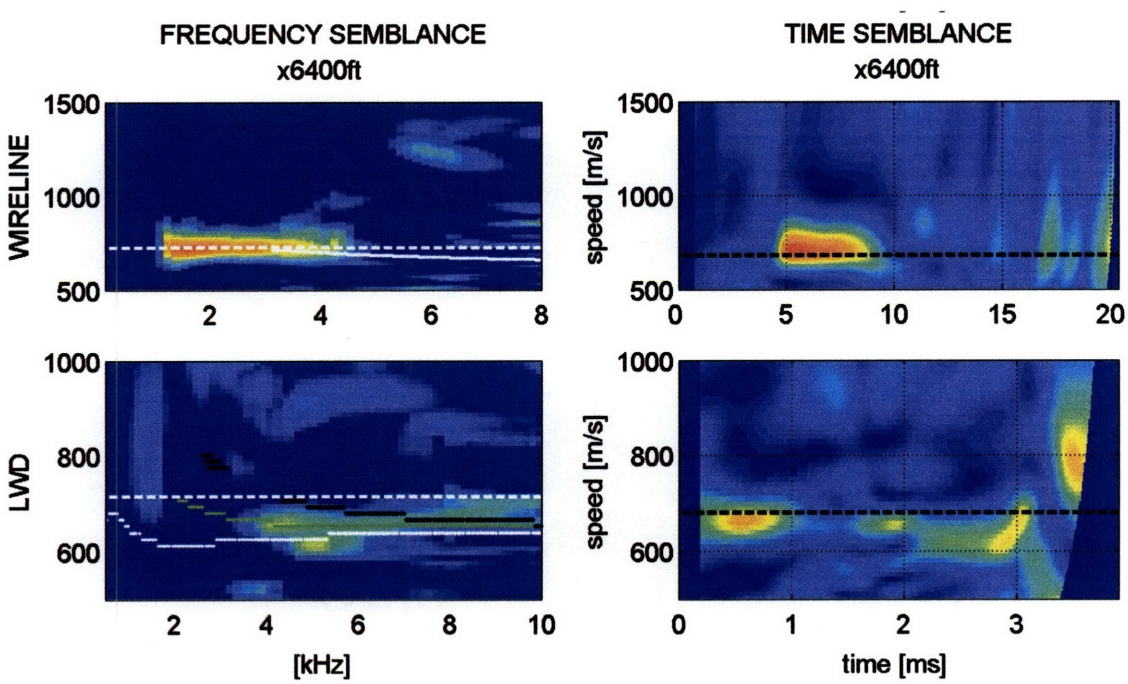

Figure 3-15: Shear velocity picks in Zone B using frequency and time semblance analysis. The wireline data are shown in the top row and the LWD in the bottom row. The white dashed lines on the left hand column indicate the shear or compressional velocity as picked from frequency semblance. The black dashed lines on the right hand column denote the industry pick from time semblance. The calculated modes for the appropriate tool are overlaid for the frequency semblance images in the dipole shear cases, the white solid line indicates the dipole mode, the green solid line indicates the quadrupole mode and the black line the hexapole mode.

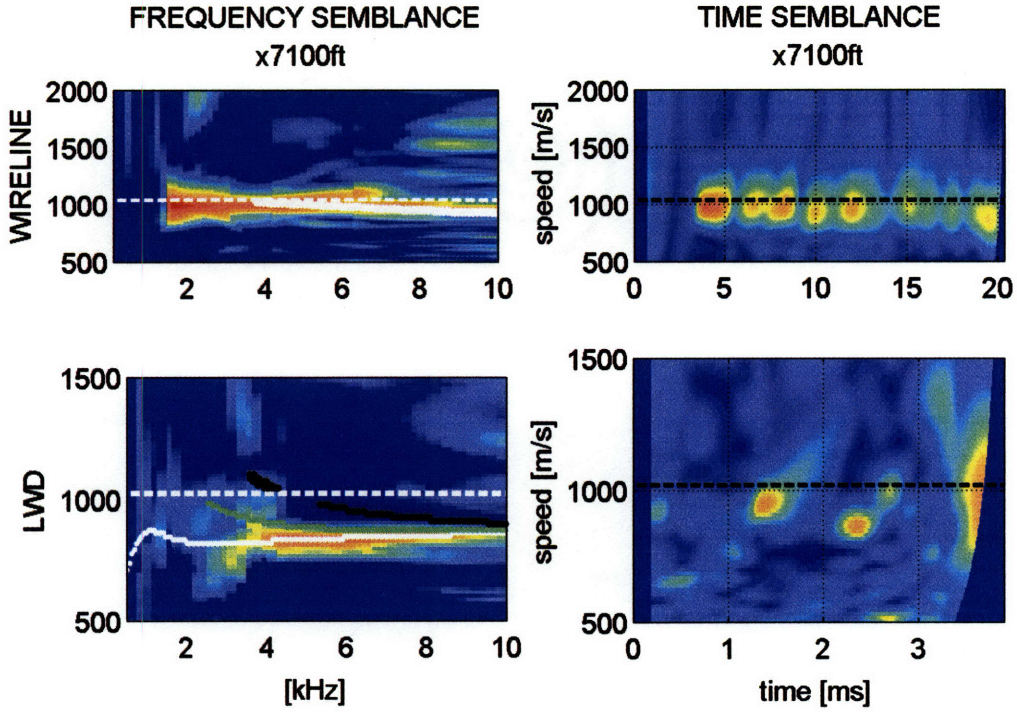

Figure 3-16: Shear velocity picks in Zone B using frequency and time semblance analysis. The wireline data are shown in the top row and the LWD in the bottom row. The white dashed lines on the left hand column indicate the shear or compressional velocity as picked from frequency semblance. The black dashed lines on the right hand column denote the industry pick from time semblance. The calculated modes for the appropriate tool are overlaid for the frequency semblance images in the dipole shear cases, the white solid line indicates the dipole mode, the green solid line indicates the quadrupole mode and the black line the hexapole mode.

of decreasing velocity and one where the formation is radially homogeneous. In this section we model the response of the tool corresponding to these scenarios.
Both tools measure in a different frequency range and have different offsets between the source and first receiver. This implies that there will be a difference between the tools' respective depths of investigation for any refracted arrivals. As a general rule of thumb, waves penetrate deeper into the formation as the source receiver separation increases, Baker (1984). Also the increased wavelength of lower frequencies implies that they will probe deeper into the formation, Plona et al. (2002). These general approximations point to the fact that the tools are measuring the formation at different radial distances from the borehole wall. These effects can be separated into those caused by the radial geometry and frequency of the tool and those caused by the radial geometry, frequency and source receiver offset combined. In this section we have modeled both scenarios to break down their respective effects on the measured borehole response.

3.4.1 Effects of frequency and radial variation on depth of investigation

To formally quantify the respective tool's depth of investigation due to frequency and radial variation we calculate the phase velocities of the compressional head wave and flexural mode by solving the wave equation in a radially layered borehole and surrounding formation. Each layer has a compressional velocity and shear velocity and density corresponding to the type of material. The boundary conditions are defined for fluid-solid and solid-solid interfaces depending on the layers and as many layers as needed to model the radial velocity profile can be added.

Radial variations in velocity around the borehole wall can be either increasing or decreasing with radial distance. Figure 3-17 and 3-18 show the radially increasing velocity models for the fast (hard) and slow (soft) formations modeled in this section. We have not shown similar plots for the decreasing velocity case as these models were just a flip from left to right of the formation parameters shown in figures 3-17 and 3-18. The last layer, i.e. the layer furthest from the borehole, extends to infinity. For the LWD model there was an additional steel layer within the borehole with an inner radius of 2.4 cm and an outer radius of 8.6 cm. The borehole radius is 10.5 cm [8.75"], which is similar to the radius of the borehole in the real data. A formation density of 2600 g/cm^3 is used throughout the model. Each velocity layer in the model is 10 cm.We will follow the terminology of Baker (1984) where an increasing radial velocity it termed "damaged" and a decreasing radial velocity is "flushed". In this terminology both of these terms refer to an invaded zone which is distinct from alteration. Alteration is used to describe changes in shale over a period of time as described by Blakeman (1982) and Hornby and Chang (1985). The goal of this paper is not to describe the processes responsible for a radial velocity gradient but to show how they can be recognized in the logged data.

In the following sections we will look at each model separately. We have four cases, radially increasing velocites, fast and slow formations and radially decreasing velocities, fast and slow formation. For the increasing models we look at both the compressional head wave and formation flexural waves. For the radially decreasing model we examine only the formation flexural mode as the measured refracted head wave is trapped in the inner layer and behaves as if there is a homogeneous formation surrounding the borehole.

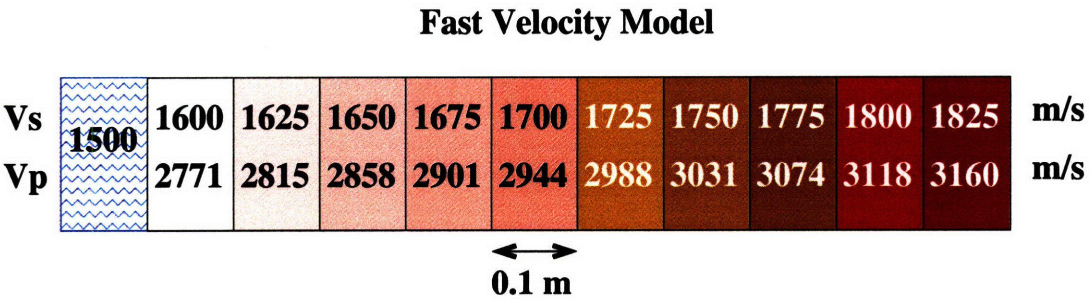

Fast Velocity Model

Vs	1500	1600	1625	1650	1675	1700	1725	1750	1775	1800	1825	m/s
Vp		2771	2815	2858	2901	2944	2988	3031	3074	3118	3160	m/s

Figure 3-17: Radially increasing fast formation velocity model.

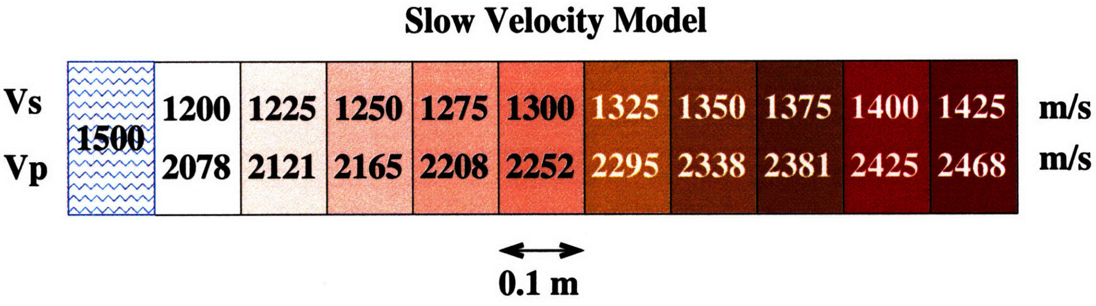

Slow Velocity Model

Vs	1500	1200	1225	1250	1275	1300	1325	1350	1375	1400	1425	m/s
Vp		2078	2121	2165	2208	2252	2295	2338	2381	2425	2468	m/s

Figure 3-18: Radially increasing slow formation velocity model

Damaged model, radially increasing velocity.

Compressional refracted arrival.

Figure 3-19 shows the effects of radially increasing velocity model on the wireline and LWD compressional head wave. For the compressional velocities, where the tools aim to measure the refracted compressional arrival, there is no dispersion associated for this wave in a homogeneous model. In the homogeneous case the picked velocity does not change with frequency. The velocities are indicated on figure 3-19 by the solid and dashed horizontal lines, at 2078 and 2468 for the slow model, and 2771 and 3160 for the fast model. The effects of radial layering are clearly seen in the case of the 10 layer model. The normally non-dispersive refracted arrival is now strongly dispersive and asymptotes to the far borehole velocity at low frequencies and the near borehole velocity at high frequencies. These refracted waves are distinct from the leaky-P mode which shows similar dispersive characteristics but whose cutoff frequency is higher, at around 6 kHz, and asymptotes to the fluid velocity at high frequencies. This form of dispersion in a compressional arrival would therefore be highly indicative of a formation with a radially increasing velocity profile and is similar to the compressional arrival seen in figure 3-13 for the wireline frequency semblance analysis. It is difficult to interpret the data more quantitatively as the shape of the dispersion caused by the radial velocity gradient is highly dependent on the layer width, number of layers and contrast between layers.

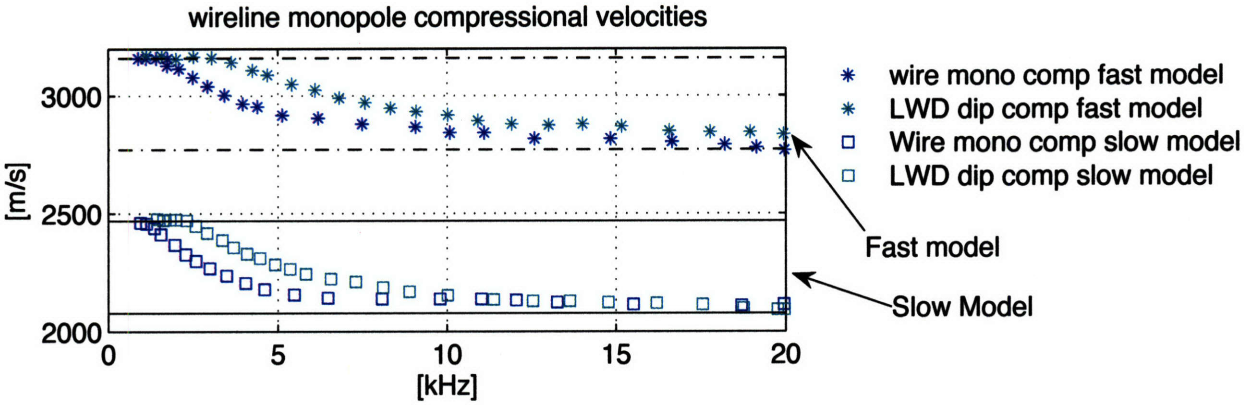

Figure 3-19: Calculated dispersion curves for the compressional wave for the wireline and LWD tools using the layered model shown in figures 3-17 and 3-18. The dashed lines indicate the compressional refracted mode for the homogeneous case using the parameters in the first and last layer in each model and the blue stars show the dispersion calculated for the faster 10 layer model, while the blue squares show the curves for the slower ten layer model.

Formation shear flexural mode for wireline and LWD.

In this section we look at the effects of the radially increasing velocity models on the formation flexural modes for both the wireline and LWD case. Figure 3-20 shows the results from the modeling using the same models shown in figures 3-17 and 3-18 but with 1cm layers. The shear flexural mode's depth of investigation cannot be estimated using the same method. The flexural mode is already dispersive in a homogeneous medium, so that when the layered model is added there are additional dispersive effects. To overcome the problem of separating the dispersive effects, and to get an estimate of the depth of investigation, an alternative method was used. The dashed lines in figure 3-20 show the wireline and LWD dipole shear flexural modes for 5 homogeneous model cases, for both the fast (upper curves) and slow models (lower curves). The velocities in the homogeneous cases are those used in the 1st, 3rd, 5th, 7th and 9th layers. The stars show the respective formation flexural mode for the 10 layer velocity model shown in figure 3-17 and 3-18. The dashed lines, starting from the lowest line in each fast and slow model case, can be identified with depths of investigation of 1cm, 3cm, 5cm, 7cm and 9 cm respectively. For the wireline dipole case we can see that at frequencies below 2 kHz the tool is probing 10 cm or more into the formation, at 3 kHz the tool is probing 8 cm, at 5 kHz 4cm and by 10 kHz it is around 1cm. This is true for both the fast and slow models for the wireline dipole flexural mode. The LWD flexural mode however probes much closer to the borehole wall at all frequencies. From the dispersion shown in the bottom plot of figure 3-20, the LWD tool probes only a little further than the slowest layer surrounding the borehole wall for both the fast and slow velocity model. At low frequencies (1-2 kHz) the LWD tool probes about 2 cm into the formation, by 3kHz the depth of investigation is only as far as the first layer in the model, which is 1cm. This is a qualitative argument and the absolute values of the depth of investigation only serve to illustrate the trends of the tool sensitivities. The parameters used in these models were comparable to those found in the data set allowing us to draw comparisons, which may not be appropriate in an absolute sense for other data sets.

Flushed model, radially decreasing velocity

In this section we reverse the order of the layers in model used in the previous section to create a flushed model ie the velocity in the layers decreases away from the borehole. We have computed the dispersion curves for the slower velocities, for the LWD and wireline dipole. We do not show the dispersion curves for the wireline monopole or LWD high frequency dipole as these modes probe only the first layer and show no dispersion. This is because the waves are refracted away from the borehole and so only a leaky compressional mode is recorded by the tool. This will be discussed more in the next section where the full synthetic seismogram is shown and some of the effects of the flushed model can be seen.

Formation flexural mode for wireline and LWD

In a similar analysis to the flexural modes seen in the last section we plot the radially varying model results over five homogeneous cases. Figure 3-21 shows the dipole flexural mode for both tools. The dashed lines represent the 1st, 3rd, 5th, 7th, and

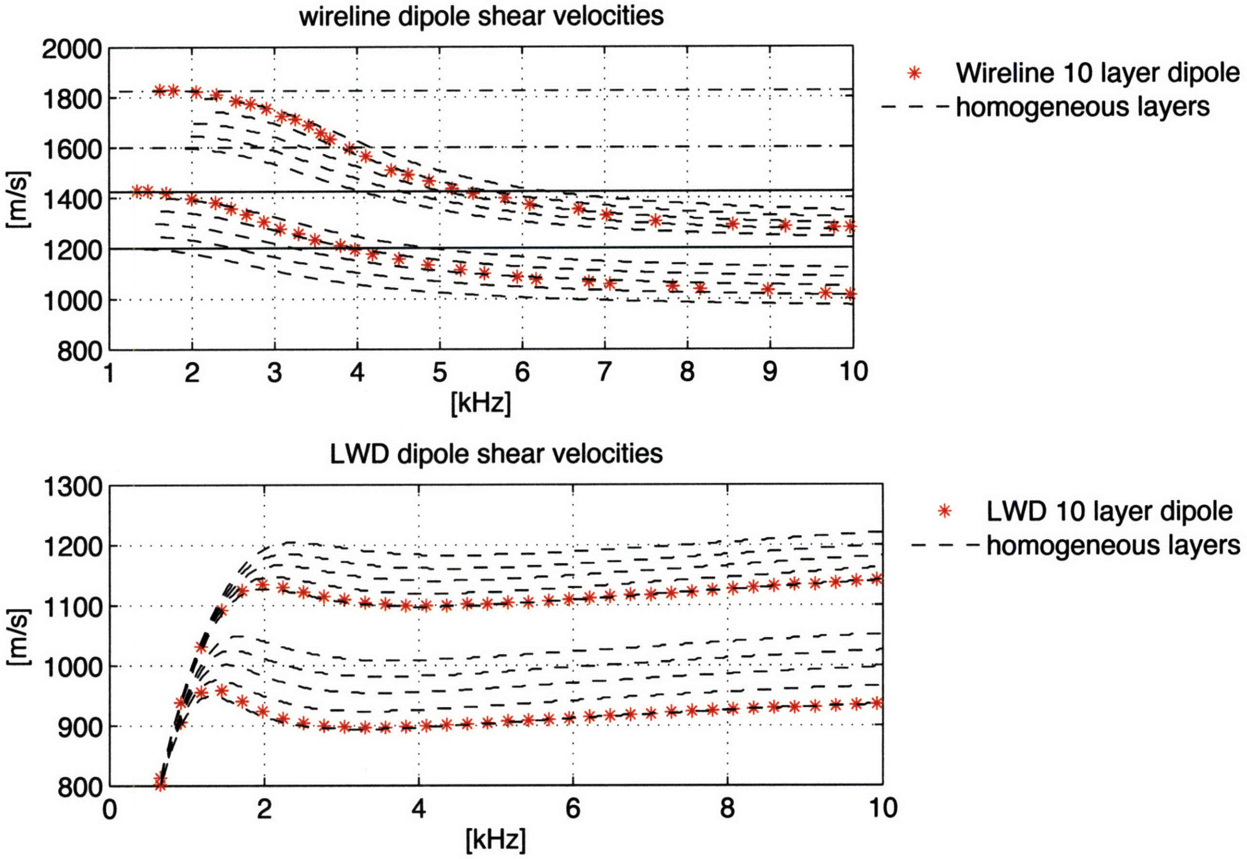

Figure 3-20: Calculated dispersion curves for the shear modes as measured by the wireline and LWD tools using the layered model shown in figures 3-17 and 3-18. The shear flexural mode dispersion is shown in the top plot for the wireline tool and, the bottom plot for the LWD tool. Here the dashed lines indicate the shear flexural mode for a homogeneous model with the properties of the 1st, 3rd,5th,7th and 9th layers in figure 3-17 (higher velocities) and 3-18 (lower velocities), The red stars indicate the dispersion curves as calculated for the 10 layer model but with 1cm layers. Note how, for the LWD case the layered model dispersion (red stars) fall almost exactly on the homogeneous dispersion curve for the parameters in the 1st layer, indicating the tool sees very close to the borehole

9th layer homogeneous models with the 1st layer being the fastest. We can see from overlaying the dispersion curve from the 10 layer model that the mode probes only into the first layer for both tools above 4 kHz. The wireline flexural mode asymptotes to the 10th layer shear velocity, suggesting its depth of investigation is further than 10 cm below 4 kHz.

Given the frequency component of real data measured by the LWD and wireline

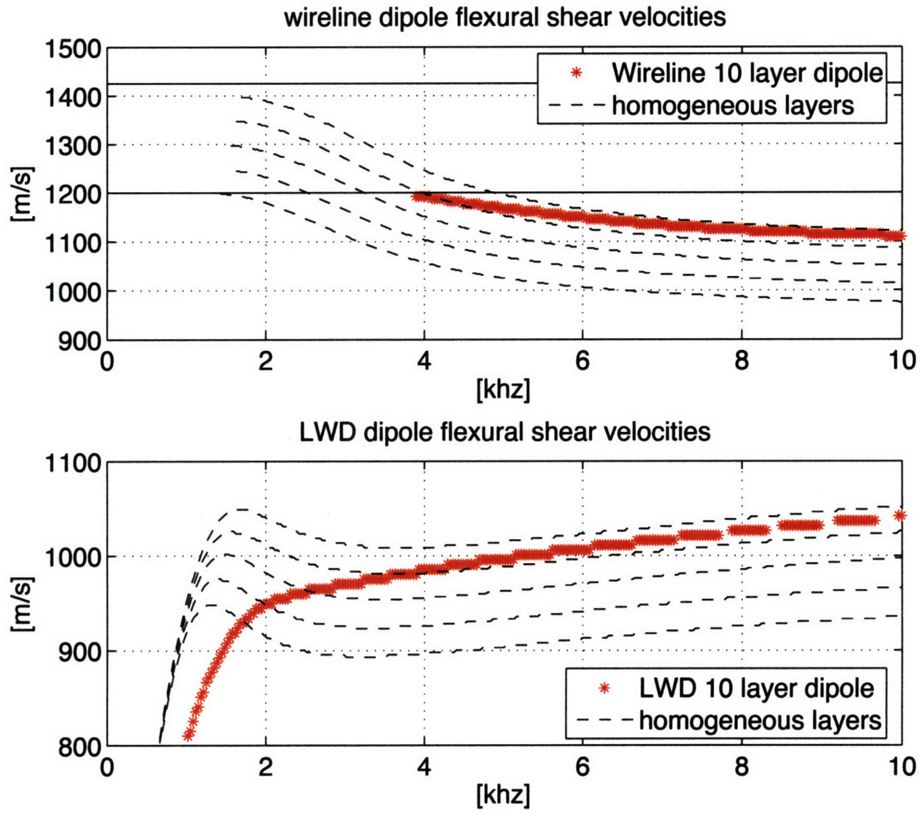

Figure 3-21: Calculated dispersion curves for the shear modes measured by the wireline and LWD tools. These modes are similar to those shown in 3-20 except the 10 layer model was reversed so that the radial velocity is decreasing and 1cm layers were used. The results are for the fast model. The dashed lines show the calculated dispersion for the homogeneous case using the properties in the 1st, 3rd, 5th, 7th and 9th layers in figure 3-17. Note how at higher frequencies, both the wireline and LWD see close to the higher velocities nearest to the borehole wall and therefore do not penetrate very deeply.

tools, the compressional measurements should be comparable. However there may be discrepancies in the shear measurement, depending on the radial velocity profile surrounding the borehole. If the radial velocity is increasing i.e. formation is "damaged", the wireline measurement will be faster. If the radial velocity is decreasing i.e. formation is "flushed", the wireline and LWD will be directly comparable. The comparison is hard to make however, as a reading on the LWD flexural mode below 5 kHz is influenced by the tool mode. This influence happens at higher frequencies for the fast to slow model. As a result the flexural mode for the LWD in the flushed model does not have the peak at around 1.75 KHz like those for the homogeneous case. If the waveforms were filtered below 4 kHz the pick made from time semblance would be too slow and the correction from a forward model of the homogeneous case is insufficient. If it is made at higher frequencies the tool is really only seeing the fastest layer and the would therefore overestimate the formation shear velocity.

Effects of source receiver offset on depth of investigation

In the previous sections we showed the calculated dispersion for a radially layered model. The results showed the phase velocities over all frequencies, but did not include the effects of source-reciever separation. Using a ray-path analogy, the deepest penetration into the formation comes from the greatest source-receiver offset. Studies on the effect of mud cake on borehole seismic signatures use ray-path models to explain changes in acoustic measurements Baker (1984), Blakeman (1982) and Baker and Winbow (1988). The consensus is that any deviation from a radially homogeneous formation can be seen in the data as a function of source receiver offset. The conclusion is that the wireline tool will probe further into the formation at any given frequency due to its longer offset.

In this section we have modeled the two tools using a wavenumber integration scheme that takes into account the source offset on each tool. Because the wireline flexural mode is already probing deeper into the formation we can assume that the source receiver offset will enhance this effect and we do not model it again in this section. The compressional refracted wave however showed the converse behavior and so we have included modeling of this mode. The waveforms generated here not only take into account the borehole geometry and formation parameters but they also include the tool's source (assumed to be a ricker wavelet) and the offset to the first receiver.

Damaged model, radially increasing velocity

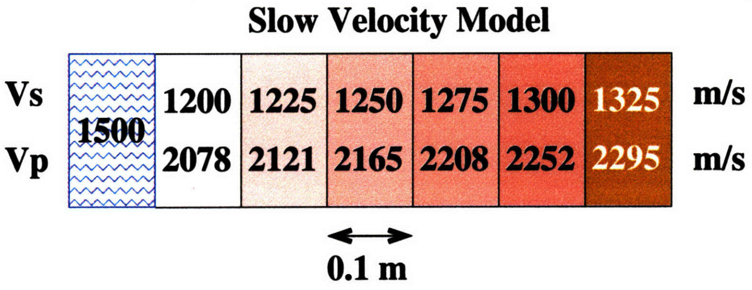

Figure 3-22: Slow velocity model used for depth of penetration studies, i.e. slow formation. Radially increasing velocity.

Figure 3-23 shows the waveforms generated for three models. First a homogeneous formation with Vp=2295 Vs=1325 m/s, second a homogeneous formation with Vp=2078 Vs=1200 m/s and lastly the velocity layers shown in figure 3-22. All models use a borehole radius of 0.105m [≈8.75"] . We have used a broad source spectrum to make the dispersion curves in the bottom plot clear.
In all cases the addition of slower layers around the borehole wall causes a delay in the arrival of the first break. There is an increase in amplitude of the P-wave and an increased ringing in the monopole compressional head wave and the dipole shear flexural mode. Both of which are caused by constructive interference from waves trapped in successive layers. These results are similar to those shown by Baker (1984) and Plona et al. (2002).

By looking at the close up figure of the wireline tool waveforms, it is clear that the layered model waveforms arrive somewhere in between the fast and slow model, but closer to the slow model. The LWD waveforms however show that the layered model does not really differ from the slow homogeneous case. The waveforms overlie each other almost perfectly suggesting that the layered model is behaving as if it were seeing the first layer only. The dispersion curves clearly show the shift from the low frequencies measuring further into the formation and seeing the faster velocities. The homogeneous compressional refracted wave is non-dispersive and follows along the red dashed line for the faster homogeneous model and the green dashed line for the slower. It is worth noting that, at 10 kHz and above, the LWD tool is only probing the slowest layer, which is what we observe in the waveforms.

The wireline tool however probes some distance into the formation out until about 25 Khz. We can conclude from this plot that at very low frequencies both tools penetrate into the furthest layer of the formation but the compressional velocity is typically picked at around 15-20 Khz. This would mean that we could expect the wireline tool to give a faster velocity than the LWD if the formation velocity was increasing radially.

Radially decreasing model

Figure 3-24 is similar to figure 3-23 except that the velocities are reversed, giving a radially decreasing velocity profile (the fast to slow model). Here we see a decrease in the wireline P monopole amplitude and no increased ringing in the coda. The decrease in P amplitude is to be expected: the wave train is leaky and radiates energy into the outer layers. Waves that are in the slower and further layers remain trapped and are not refracted back into the borehole as there is no critical refraction along these boundaries.

The arrival of the refracted wave for the layered model is again in between the fast and slow homogeneous models but this time is closer to the fast arrival. The LWD waveforms show a similar arrival and are also closer to the fast homogeneous model. There is no diminished amplitude for the LWD dipole case. The dispersion curves show that the wireline tool is able to see beyond the first layer into the slower

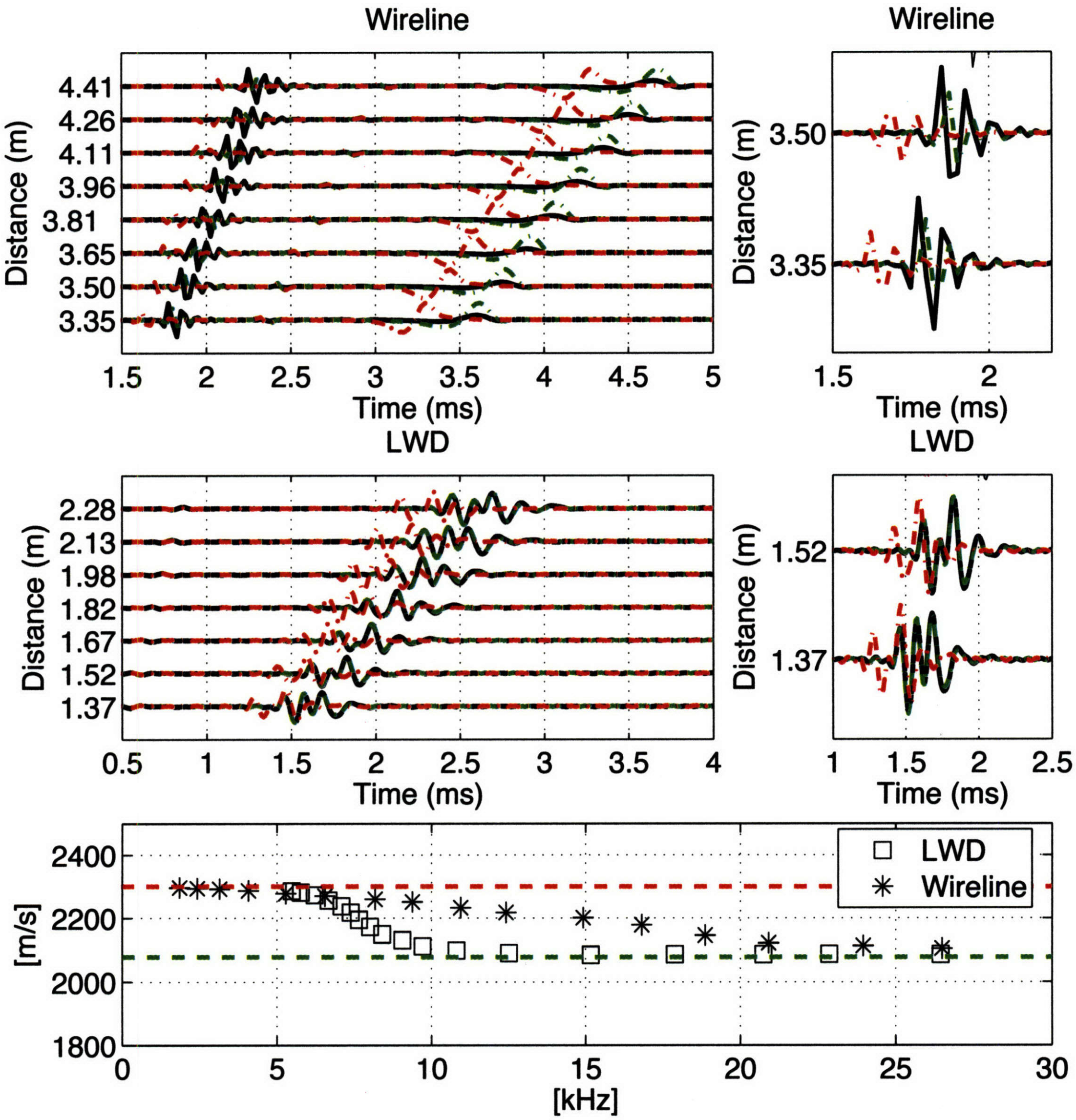

Figure 3-23: Waveforms for the radially increasing velocity model for the wireline and LWD compressional refracted wave.. Homogeneous models; Red, Vp=2295 Vs=1325 and green, Vp=2078, Vs=1200 m/s. Black refer to the layered model shown in figure 3-22. The right hand plots show a close up of the first arrivals shown on the left. Note how the arrival of the layered model in black falls between the fast and slow homogeneous refracted arrivals for the wireline tool but arrives with the slow homogeneous arrival for the LWD case. This suggests that the LWD tool measures close to the borehole wall for the compressional dipole. The bottom plot shows the dispersion curves as extracted from the waveforms. The red and green dashed lines correspond to the expected dispersion curve for the homogeneous cases shown in the waveforms plots. Above 10 kHz the LWD tool sees close to the borehole wall, while the wireline sees further due to the greater source offset.

layers but only at very low frequencies. Above 10 kHz both tools see only the first and fastest layer. The LWD dipole compressional arrival is weak and not observed below 8 Khz and quickly asymptotes to the velocity in the inner and fastest layer.

To summarize this section, we have shown that the tools can measure at different depths into the formation depending on their frequencies and or their source-receiver offsets. Traditional thinking is that both tools should measure the same velocity and any difference between the two measurements was due to temporal changes in formation over the time period between measurements. While we do not discount that there are effects on the borehole over time there are also arguments for the tool measurement radial penetration. In an effort to summarize the salient points seen in the preceding section we have created table 3.4. Here we briefly compare the expected tool bias for the three proposed models in zones A, B and C, i.e increasing radial velocity, decreasing radial velocity and radially homogeneous.

3.5 Signatures from the real data

We have established that the tools have differing depths of investigation and that differences in processing may account for small differences between the measured velocities in each tool. In this section we re-process waveforms taken from zones A, B and C. Figure 3-25 shows the velocity picks from the time semblance thin solid lines, and the frequency semblance picks, dashed lines with markers. As mentioned in a previous section the frequency semblance is computationally expensive so that only seven depths were picked and processed for each zone. If we return to the earlier hypothesis that there is a radially increasing velocity gradient in the first zone, we can reinterpret the velocity picks given the modeled results in section 3.4.1. The compressional mode shows that there is better agreement between the LWD and wireline tool using the frequency semblance. The velocities were picked at 15kHz and so there

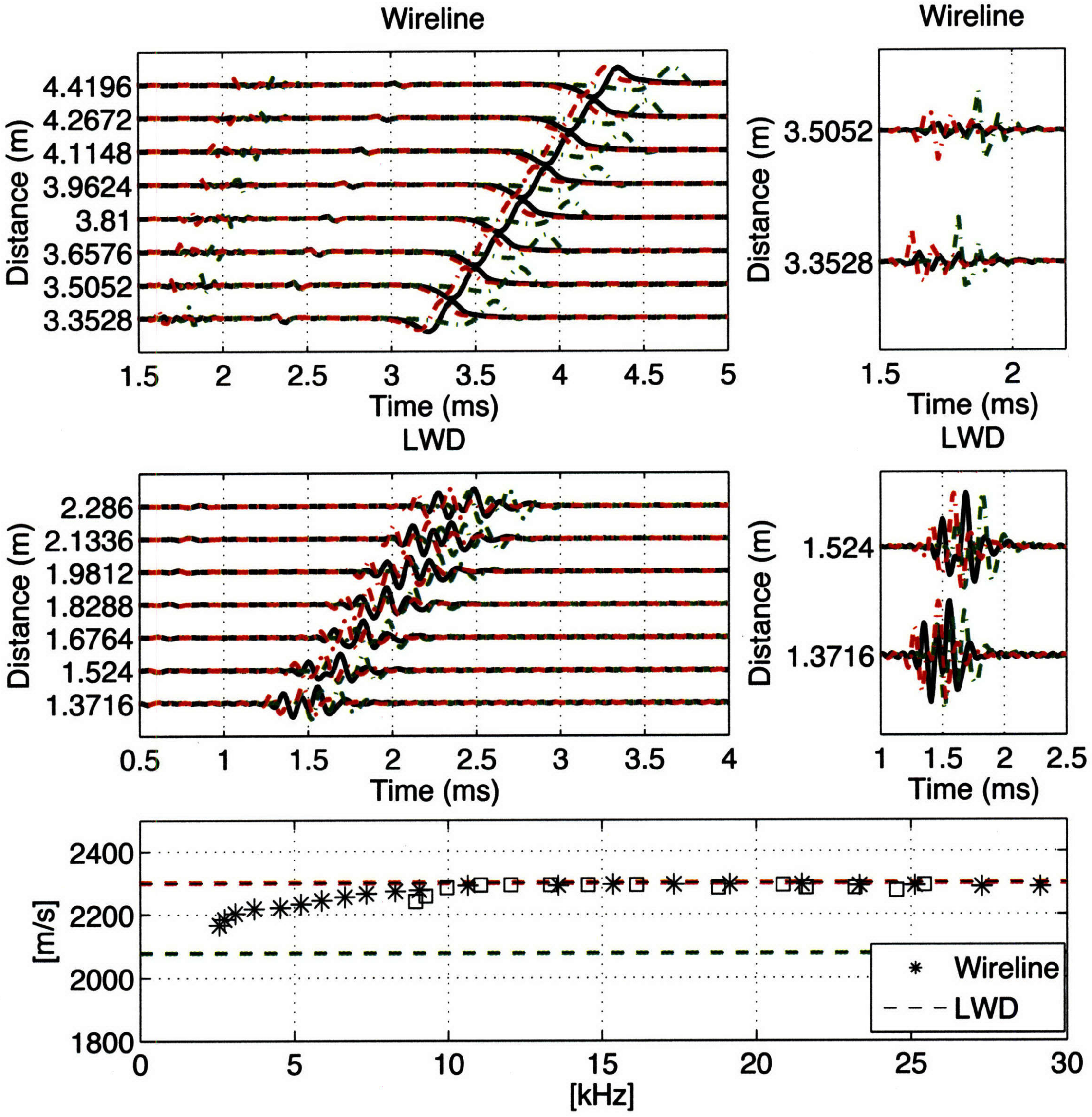

Figure 3-24: Waveforms for the radially decreasing velocity model. Homogeneous models; Red, Vp=2295 Vs=1325 and green, Vp=2078, Vs=1200 m/s. Black is the first six layers of the model shown in 3-22 with their order reversed. The plots on the right hand side show a close up of the first two traces shown on the left. Note how the monopole compressional wireline arrival is greatly reduced in amplitude. Both tool arrivals for the layered cases arrive between the homogeneous cases, indicating the tools see further between the model extremes. The bottom plot shows the dispersion curves as extracted from the above waveforms. For the radially decreasing velocity case both tools see very close to the borehole wall above 10 kHz.

Radial velocity profile near → far borhole wall.	fast → slow	slow → fast	homogeneous
Compressional velocity	LWD $\approx$ Wireline due to leaky nature of compressional mode in this type of formation, both tools see close to borehole wall	Wireline $\geq$ LWD depending on frequency band of measurement. As a result of longer source-receiver offset.	LWD = Wireline
Shear velocity	LWD $\approx$ Wireline assuming the appropriate correction is made for the the LWD dispersion. If not Wireline > LWD (due to underestimating LWD correction)	Wireline > LWD due to both mode shape and increased source-receiver offset	LWD = Wireline assuming appropriate correction to LWD.

Table 3.4: Summary of section 3.4 in regards to the proposed radial velocity profiles seen in zones A, B and C

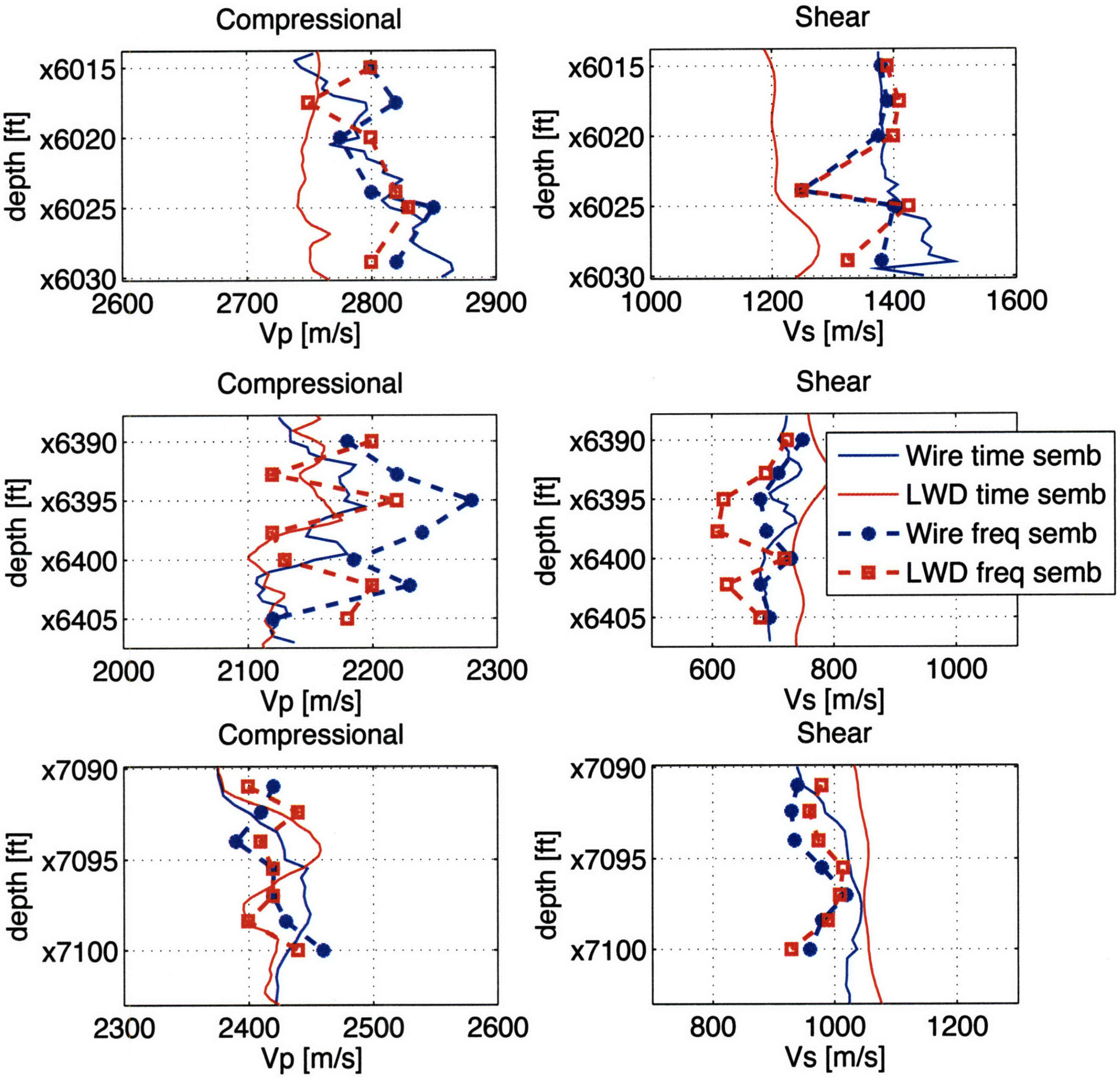

Figure 3-25: Velocity picks from time and frequency semblance in the three zones of interest. The dashed lines indicate the frequency semblance velocity picks and the this solid lines show the time semblance velocity picks.

should be good agreement at this frequency. It would have been informative to also compare the velocities at lower frequencies to see if they diverge with the wireline tool measuring lower velocities. This analysis is not possible with the current data, as the excited frequencies do not extend below 12 kHz for the LWD case. The frequency semblance in figure 3-11 show a lowering velocity at around 6kHz which is consistent with the modeled case in section 3.4.1.

The shear velocity picks for this zone can be seen in the upper right hand plot in figure 3-25. Here the LWD and wireline tools have very good agreement using the frequency semblance picks. This is much improved over the large 15% difference that is seen in the picks from the time semblance. The frequency semblance picks were made at 4kHz for both the wireline and LWD. From figure 3-21 we can see that the two measurements should agree at this frequency. At 5 kHz both tools are seeing only into the first few centimeters around the borehole and when the tool dispersion correction is applied to the LWD velocity pick both tools are measuring the same formation velocity.

In zone B, $\approx$ x6400 ft, the hypothesis is that the surrounding formation is damaged, i.e. an increasing radial velocity profile. Here the re-processed velocity picks for the compressional refracted wave show that the wireline is probing a faster velocity layer. The results from section 3.4.1 show that this should be the case for a radially increasing velocity model. The dispersion curves in figure 3-23 indicate that the wireline tool is probing further into the formation and is therefore sensitive to a faster velocity layer. The shear velocity picks show a similar behavior with the wireline again measuring slightly faster velocities. Returning to figure 3-20 we can deduce that the LWD flexural mode is only sensitive to velocities very close to the borehole wall, however the wireline tool in the slow to fast model sees further into the damaged zone. Again these velocity picks were taken at 5 kHz.

In zone C, at x7100 ft, there appears to be a formation that has a homogeneous velocity profile. The velocity picks from the frequency and time semblance are seen in the third row of figure 3-25. In the homogeneous case both the LWD and wireline tool should show good agreement for both the compressional and shear pick. There should be no dispersion seen in the refracted wave and the flexural waves for both the LWD and wireline should have only the dispersion effects caused by the geometry of the tool and borehole. Lastly we expect that the time and frequency semblance picks should also show good agreement.

The frequency semblance reveals subtleties in the data that are otherwise missed with the time semblance approach. Without the correct velocities it is hard to interpret this data set in terms of the tool measurement penetrations discussed in section 3.4. For a final verification of the radial profiles we have picked the velocities from the time semblance for the first and last 4 receivers in each of the zones of interest. It is well established, for the refracted waves, that the greater the offset between source and receiver, the greater the depth of penetration of the waveforms. This means that the velocity pick from the last four receivers should see further into the borehole wall than the first four. The difficulty with this type of analysis is that the signal to noise ratio is significantly reduced by using only four waveforms in the semblance codes. The time semblance still gives meaningful results, provided the data quality is good, but the frequency semblance can be much more difficult to interpret. Because of this restriction, figure 3-26 shows the compressional refracted picks for the LWD and wireline tools from the time semblance only. It is the relative velocities between the first and last receivers rather than the absolute value of the velocity pick that is important. Returning once more the three models hypothesized from the frequency semblances seen in figures 3-11 to 3-16 we can compare our expectation with the velocities seen in figure 3-26. If the semblance velocity pick from the first four receivers is greater than that from the last four we assume a radially decreasing model, if the first four show a slower velocity than the last four we assume a radially increasing velocity and if the first and last receivers show similar velocities we assume a homogeneous velocity profile. Zone A shows a radially decreasing velocity behavior, the second set of depths at zone B show a radially increasing behavior and the last depths at zone C show a more homogeneous velocity profile, which all concur with our initial predictions from section 3.3.

3.6 Discussion and Conclusions

Separating the elements of the case study into parts we can draw several conclusions. The first of which is that the method of velocity analysis greatly impacts the measurement in areas where the velocity around the borehole is not homogeneous. The comparison between the time and frequency semblance picks is shown in section 3.3 and figures 3-5 to 3-10. We see that while there are still discrepancies between the wireline and LWD measurements, they are reduced when frequency domain processing methods are applied. It is noted that the dispersive effects of a radial velocity gradient can cause errors in the time semblance pick which are accounted for with the frequency semblance.

Secondly it is advantageous to have the full shape of the mode in the region of the excited frequencies as this can reveal information about the formation velocity profile. The differences between the wireline and LWD measurements after processing in the frequency domain can be explained in terms of varying radial velocity profiles. If the time domain velocity picks are used there is not model that can correctly explain the differences in tool measurement at all depths in the data. This is further validation that the frequency domain methods give a more accurate estimate of formation velocities. We have not proposed a mechanism for these velocity gradients but have shown that if they exist it is likely that the wireline and LWD tools will measure different velocities. This second conclusion is very important when comparing the two data sets. It would be a mistake to expect the tool measurements to concur exactly as they are effectively measuring at differing radial depths and small deviations between velocity picks are to be expected. In section 3.4, where we attempt to quantify the depth of investigation we show how the differing velocity profiles also alter the mea-

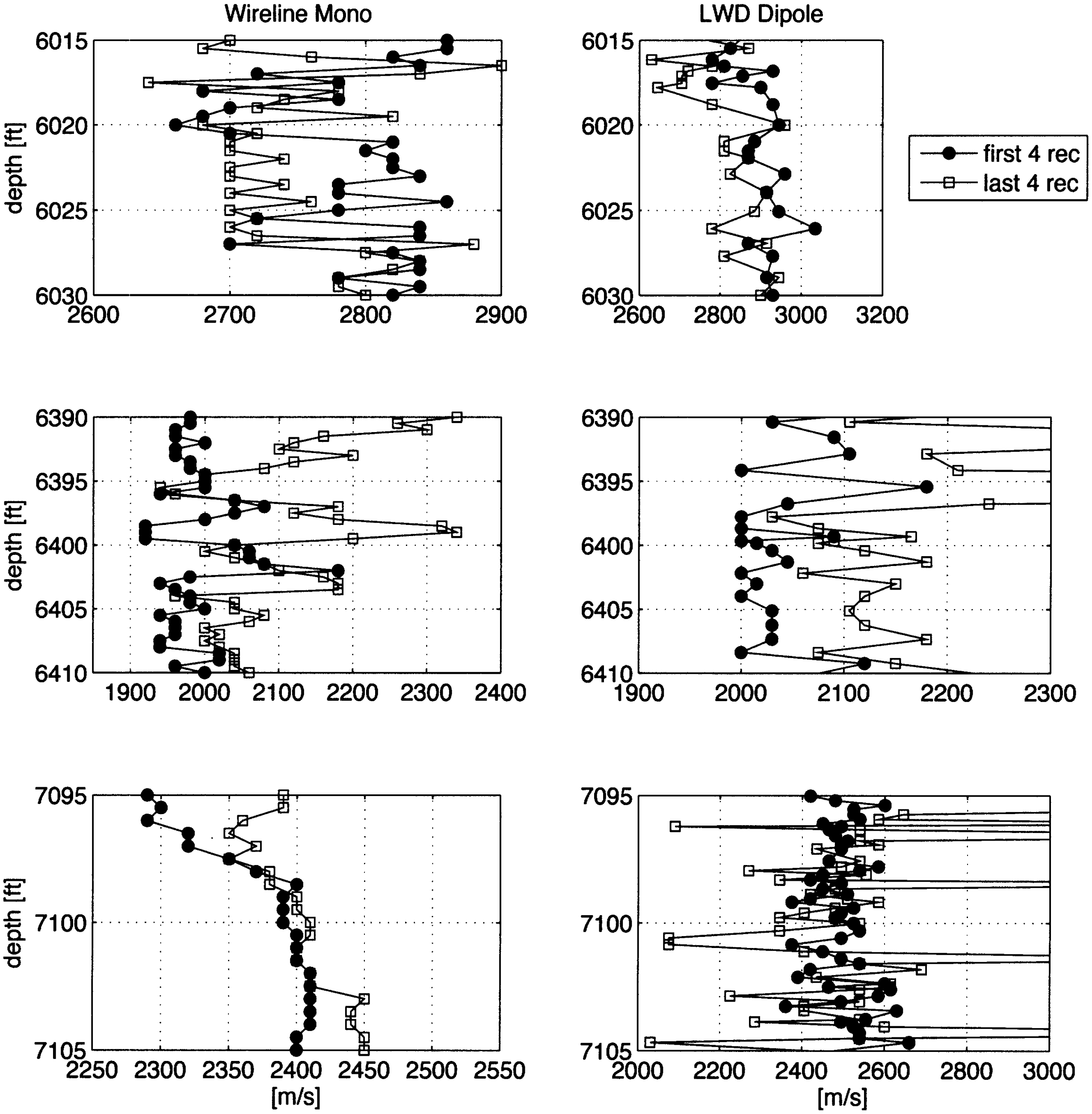

Figure 3-26: Velocity picks from time semblance of compressional refracted wave using the first 4 receivers and last the 4 receivers. The closed circles show the first velocity time semblance pick using the waveforms from the first four recievers and the open circles show the picks from the last four receivers. Because the last four receivers have a greater source receiver offset we assume their penetration into the borehole wall is greater. This figure shows that the radial velocity gradient is seen to increase in the first zone (top plots), decrease in the second zone (center plots) and is homogeneous in the third zone (bottom plots).

surement penetration. In the case of the fast to slow model, the refracted P wave become trapped in the high velocity zone surrounding the borehole therefore reducing the amplitude of the measured refracted wave by the tool. In the case of the radially increasing velocity profile this is not the case and the P response measured by the tool is not attenuated. It is of further interest to note the effects of the tool geometry on the modes, without taking into account the source offset distance, as in section 3.4.1. Here we see that the LWD tool actually probes further into the formation for the P-wave but this situation is reversed when the z-axis of the tool is included in the model.

In final conclusion, we note that neither tool appears more accurate than the other, each tool has a measurement depth of penetration defined by the tool geometry and frequency range, which is further conditioned by the surrounding formation properties. What is important to note when comparing velocity picks form the tools is that overall trends in the data agree and that the waveforms have been processed accurately. A full frequency semblance, although computationally expensive can be a useful interpretive tool if calculated a few times throughout the log. This can help isolate zones which may need further interpretation when reading the time semblance velocity picks. One quick check for velocity gradients is to process near and far receiver sets and compare the results, providing data quality is good.

A similar data set taken in a fast formation would be useful for further analysis to verify the differences in velocity as measured by the two tools for the compressional refracted wave. The data set used in this paper is somewhat unique, it is unlikely that a borehole would be logged with both type of tool as cost of operations is high and two velocity analyses are somewhat redundant from an interpretation point of view. New generation LWD tools are capable of measuring at lower frequencies for the shear dipole flexural mode so further analysis with this type of data would prove useful.

Chapter 4

Mode analysis for LWD geometry in transversely isotropic media.

This chapter describes the method used for calculating the modes for the logging while drilling, LWD, tool geometry in an isotropic and transversely isotropic medium. The methodology follows closely that of the model discussed in appendix A but is considerably more complex. If the reader is unfamiliar with the method, it is suggested that he/she read appendix A as a primer for this chapter. We develop a mode analysis algorithm for the general layered case which can have an arbitrary number of cylindrical layers with any combination of fluid and solid boundaries. The outermost layer may also be transversely isotropic. The formulation of the algorithm in this manner allows us to model both the wireline and LWD geometry in an arbitrarily layered medium which has applications in later chapters. Figure 4-1 shows the case for the LWD tool in a multi-layered medium with a transversely isotropic outer layer with an option for interior isotropic formation layers. Throughout this chapter we will model a system comprising of the sequence: fluid, isotropic solid, fluid, transeversly isotropic solid. We will derive only the equations necessary for the transversely isotropic case as these can be reduced to the isotropic case by using the appropriate elastic constants in the set of equations given in 4.5. An excellent review of the material can be found in Tang and Cheng (2004), which contains similar derivations of both the transversely isotropic and isotropic cases. The original treatment of the work can be found in many borehole geophysics papers including Cheng and Toksöz (1981), Paillet and White (1982) , Chan and Tsang (1983), Kurkjian and Chang (1986) and Schmitt (1989).

In our derivation we follow closely the work of Ricks (1994) and Rao V.N (1999), where Hankel functions of the first kind ($H_n^{(1)}(x)$) and Bessel functions of the first kind ($J_n(x)$) are used in place of the usual modified Bessel functions of the first ($I_n(x)$) and second ($K_n(x)$) kind in the potential equations used to solve the borehole system. In theory any two Bessel functions can be chosen to represent the potential solutions to the wave equation but the Hankel funtions of the first kind and the Bessel function of the first kind give the greatest stability in wavenumber over a large range of frequencies and borehole geometries Ricks (1994).

4.1 Solution of the wave equation in transversely isotropic medium using cylindrical coordinates.

The general wave equation is given by,

$$\nabla . \sigma + \rho \omega^2 \mathbf{u} = 0 \tag{4.1}$$

where σ is the stress tensor, ρ the denstiy and $\mathbf{u}$ the displacement vector. Helmholtz's theorem states that the wave equation solution is separable into three scalar potentials Φ, χ and Γ,

$$\mathbf{u} = \nabla \Phi + \nabla \times (\chi \hat{\mathbf{z}}) + \nabla \times \nabla \times (\Gamma \hat{\mathbf{z}}) \tag{4.2}$$

Expanding equation 4.2 into cylindrical coordinates, i.e. radial, azimuthal and vertical components, u, v and w and writing it in terms of the scalar potentials, we have the displacements

$$
\begin{aligned}
u &= \frac{\partial \Phi}{\partial r} + \frac{1}{r}\frac{\partial \chi}{\partial \theta} + \frac{\partial^2 \Gamma}{\partial r \partial z} \\
v &= \frac{1}{r}\frac{\partial \Phi}{\partial \theta} - \frac{\partial \chi}{\partial r} + \frac{1}{r}\frac{\partial^2 \Gamma}{\partial \theta \partial z} \\
w &= \frac{\partial \Phi}{\partial z} + \left[\frac{\partial^2}{\partial z^2} - \nabla^2\right]\Gamma
\end{aligned}
\tag{4.3}
$$

The stress-strain (Hookes' law) relationship in cylindrical coordinates for the transversely isotropic case is written as

$$
\begin{pmatrix} \sigma_{rr} \\ \sigma_{\theta\theta} \\ \sigma_{zz} \\ \sigma_{\theta z} \\ \sigma_{rz} \\ \sigma_{r\theta} \end{pmatrix} = \begin{pmatrix} c_{11} & c_{11}-2c_{66} & c_{13} & 0 & 0 & 0 \\ c_{11}-2c_{66} & c_{11} & c_{13} & 0 & 0 & 0 \\ c_{13} & c_{13} & c_{33} & 0 & 0 & 0 \\ 0 & 0 & 0 & c_{44} & 0 & 0 \\ 0 & 0 & 0 & 0 & c_{44} & 0 \\ 0 & 0 & 0 & 0 & 0 & c_{66} \end{pmatrix} \begin{pmatrix} e_{rr} \\ e_{\theta\theta} \\ e_{zz} \\ e_{\theta z} \\ e_{rz} \\ e_{r\theta} \end{pmatrix} \tag{4.4}
$$

which can be reduced to the isotropic case by setting

$$
\begin{aligned}
c_{11} &= \lambda + 2\mu \\
c_{66} &= \mu \\
c_{33} &= c_{11} \\
c_{13} &= c_{11} - 2c_{66} \\
c_{44} &= c_{66}
\end{aligned}
\tag{4.5}
$$

The strain elements in equation 4.4, in terms of the cylindrical displacements Auld (1990), are;

$$\begin{aligned}
e_{rr} &= \frac{\partial u}{\partial r} \\
e_{\theta\theta} &= \frac{u}{r} + \frac{1}{r}\frac{\partial v}{\partial \theta} \\
e_{zz} &= \frac{\partial w}{\partial z} \\
e_{r\theta} &= \frac{1}{2}\left(\frac{1}{r}\frac{\partial u}{\partial \theta} - \frac{v}{r} + \frac{\partial v}{\partial r}\right) \\
e_{\theta z} &= \frac{1}{2}\left(\frac{1}{r}\frac{\partial w}{\partial \theta} + \frac{\partial v}{\partial z}\right) \\
e_{rz} &= \frac{1}{2}\left(\frac{\partial w}{\partial r} + \frac{\partial u}{\partial z}\right)
\end{aligned} \tag{4.6}$$

Expanding 4.4, using 4.3 and 4.6, gives three wave equations:

$$\begin{gathered}
c_{11}\nabla^2\Phi + (c_{13} + 2c_{44} - c_{11})\frac{\partial^2\Phi}{\partial z^2} + \rho\omega^2\Phi + \\
\frac{\partial}{\partial z}\left[(c_{11} - c_{13} - c_{44})\nabla^2\Gamma + (c_{13} + 2c_{44} - c11)\frac{\partial^2\Gamma}{\partial z^2} + \rho\omega^2\Gamma\right] = 0
\end{gathered} \tag{4.7}$$

$$\begin{gathered}
\frac{\partial}{\partial z}\left[(c_{13} + 2c_{44})\nabla^2\Phi + (c_{33} - c_{13} - 2c_{44})\frac{\partial^2\Phi}{\partial z^2} + \rho\omega^2\Phi\right] \\
+\left(\frac{\partial^2}{\partial z^2} - \nabla^2\right)\left(c_{44}\nabla^2\Gamma + (c_{33} - c_{13} - 2c_{44})\frac{\partial^2\Gamma}{\partial z^2} + \rho\omega^2\Gamma\right) = 0
\end{gathered} \tag{4.8}$$

$$c_{66}\nabla^2\chi + (c_{44} - c_{66})\frac{\partial^2\chi}{\partial z^2} + \rho\omega^2\chi = 0 \tag{4.9}$$

We find that for the isotropic case the three scalar wave equations are separable and distinct, however in the transversely isotropic case equations 4.7 and 4.8 are coupled. The displacement potentials for a multipole wave of order n can, in the isotropic case, be written as

$$\left.\begin{array}{c}\Phi\\ \chi\\ \Gamma\end{array}\right\} = e^{ikz}e^{in\theta}\left\{\begin{array}{c}AH_n^{(1)}(q_pr) + BJ_n(q_pr)\\ CH_n^{(1)}(q_{sh}r) + DJ_n(q_{sh}r)\\ EH_n^{(1)}(q_{sv}r) + FJ_n(q_{sv}r)\end{array}\right. \tag{4.10}$$

Where A, C, E are the amplitude coefficients of the outgoing waves, B, D, F are the amplitude coefficients of the incoming waves, n is the multipole order, k is the axial wavenumber, θ is the azimuthal angle, z is the vertical axis, J_n is the Bessel function of the first kind and $H_n^{(1)}$ is the Hankel function of the first kind and q_p, q_{sv} and q_{sh} are the radial wavenumbers for the compressional waves, the shear waves polarized in the vertical direction and the shear waves polarized in the horizontal direction respectively.

For the isotropic layers the solutions are those given in equation 4.10. In a fluid we use the same solution but only the Φ potential is relevant as there is no shear wave generated. Note for the isotropic case the modes described by χ and Γ are degenerate because the velocities of the shear vertical, S_v, and shear horizontal, S_h, are equal. For the transversely isotropic case these velocities are distinct and the potential equations for Φ and Γ are coupled. Using the isotropic solutions as a starting point we can substitute them into equations 4.7, 4.8 and 4.9 to find the appropriate potential equations for the transversely isotropic case. Only the outer unbounded layer can be transversely isotropic in the model described in figure 4-1. In this case we only need to consider the outgoing waves in the potential wave equations, i.e. A_n, C_n and E_n. This is a consequence of an imposed radiation condition. We define the last layer in the system as semi-infinite, which implies that there are no incoming waves and we therefore need only define the outgoing potentials.

$$\left.\begin{array}{c}\Phi\\ \chi\\ \Gamma\end{array}\right\} = e^{ikz}e^{in\theta}\left\{\begin{array}{c}AH_n^{(1)}(q_pr)\\ CH_n^{(1)}(q_{sh}r)\\ EH_n^{(1)}(q_{sv}r)\end{array}\right. \tag{4.11}$$

We wish to find the corresponding radial wavenumbers, q_p, q_{sv} and q_{sh}, for each potential following an analysis like that found in chapter two of Tang and Cheng (2004). The substitution leads to

$$(q^2+k^2)(-c_{66}q^2-c_{44}k^2+\rho\omega^2)(Uq^4-V\omega^2q^2+W\omega^4)=0 \tag{4.12}$$

where

$$\begin{aligned} U &= c_{11}c_{44} \\ V &= \rho(c_{11}+c_{44})-(c_{11}c_{33}-c_{13}^2-2c_{13}c_{44})\left(\frac{k^2}{\omega^2}\right) \\ W &= c_{33}c_{44}\left(\frac{\rho}{c_{44}}-\frac{k^2}{\omega^2}\right)\left(\frac{\rho}{c_{33}}-\frac{k^2}{\omega^2}\right) \end{aligned} \tag{4.13}$$

The solution for the radial wavenumber for the S_h wave, which is uncoupled, is found when $(-c_{66}q^2-c_{44}k^2+\rho\omega^2)=0$, therefore

$$q_{sh}=\sqrt{\frac{\rho\omega^2-c_{44}k^2}{c_{66}}} \tag{4.14}$$

The solution for the S_v and P wavenumber is found when $(Uq^4+V\omega^2q^2+W\omega^4)=0$ which leads to two solutions known as the quasi-compressional and quasi-shear waves.

$$\begin{aligned} q_p &= i\omega\sqrt{\frac{-V+\sqrt{V^2-4UW}}{2U}} \\ q_{sv} &= i\omega\sqrt{\frac{-V-\sqrt{V^2-4UW}}{2U}} \end{aligned} \tag{4.15}$$

This coupling leads to Φ and Γ being defined as the following

$$\left.\begin{array}{c}\Phi\\ \Gamma\end{array}\right\} = e^{ikz}e^{in\theta}\left\{\begin{array}{l} AJ_n(q_pa)H_n^1(q_pr)+b'EJ_nH_n^1(q_{sv}r) \\ a'AJ_n(q_pa)H_n^1(q_pr)+EJ_nH_n^1(q_{sv}r)\end{array}\right. \tag{4.16}$$

where,

$$
\begin{aligned}
a' &= -\frac{\omega}{ik\bar{\beta}} \frac{(c_{13}+2c_{44})k^2 + c_{11}q_p^2 - \rho\omega^2}{c_{44}k^2 + (c_{11}-c_{13}-c_{44})q_p^2 - \rho\omega^2} \\
b' &= -\frac{ik\bar{\beta}}{\omega} \frac{c_{44}k^2 + (c_{11}-c_{13}-c_{44})q_{sv}^2 - \rho\omega^2}{(c_{13}+2c_{44})k^2 + c_{11}q_{sv}^2 - \rho\omega^2}
\end{aligned} \tag{4.17}
$$

Here a' and b' are made to have the dimension of length by multiplying by $\frac{\omega}{\bar{\beta}}$ and $\frac{\bar{\beta}}{\omega}$ respectively, where $\bar{\beta}$ is the average shear velocity of the model.This ensures that all the potential equations will be consistent and is discussed further in the next section. We now have the formulation for the potentials in each type of layer, either fluid, isotropic solid or transversely isotropic solid. Returning to the original model we can define the potentials in each layer to build the system of equations that can be solved simultaneously. We consider a model with j layers and $j-1$ interfaces. The jth layer in the model is defined by it's material properties, e.g. isotropic, transversely isotropic, fluid, solid etc. and the boundary conditions at each interface are determined by the the type of material on either side of the boundary.

4.1.1 Normalization of displacement potentials

In terms of displacement potentials, the total displacement is written as

$$
\mathbf{u} = \nabla\Phi + \nabla \times (\chi\hat{z}) + \nabla \times \nabla \times (\Gamma\hat{z}) \tag{4.18}
$$

so that, because the left hand side has units of displacement, the potentials Φ, χ must have units of length squared, while Γ has units of length cubed. For ease of comparison of the magnitude of the displacement constants, we choose to write the

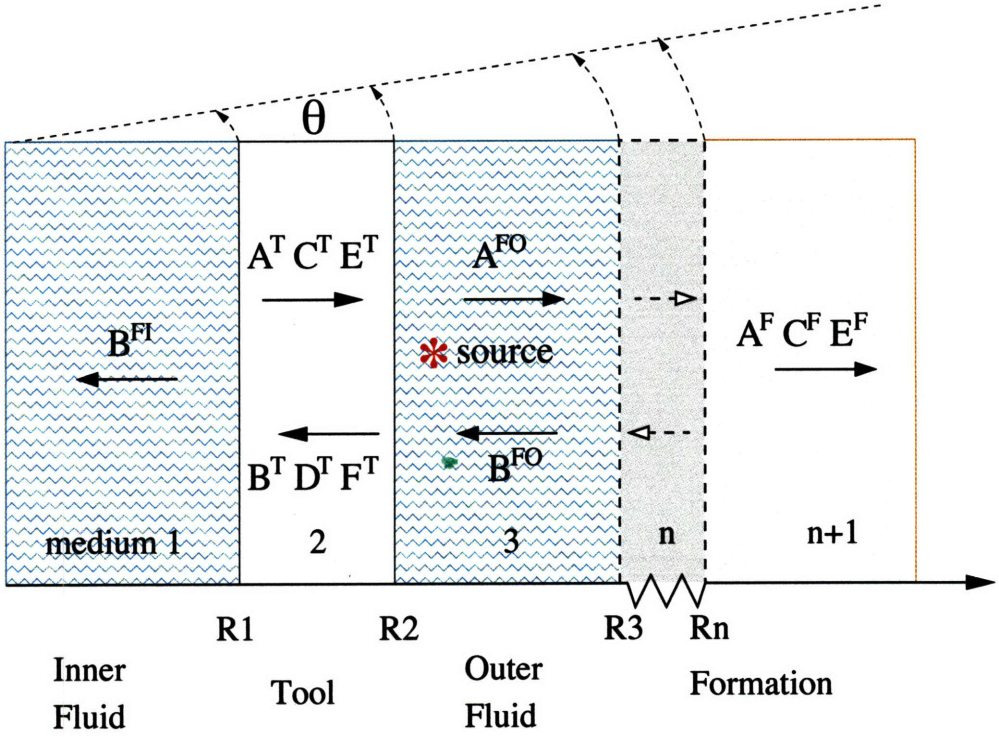

Figure 4-1: Radial model; A, C and E denote the amplitudes of the compressional, shear-Sv and shear-Sh of the outgoing waves and B,D and E denote the amplitudes of the respective incoming waves. The fluid layers are acoustic, needing only one constant, and the tool is isotropic. The nth layer, if added to the model, consists of one or more isotropic solid layers and the n+1 layer is either an isotropic or transversely isotropic radially semi-infinite solid.

displacement potentials in medium j as

$$\begin{aligned}
\Phi &= e^{in\theta}e^{ikz}\left(\frac{\bar{\alpha}}{\omega}\right)\left[\tilde{A}_n(k,\omega)H_n^{(1)}(q_p r) + \tilde{B}_n(k,\omega)J_n(q_p r)\right] \\
\chi &= e^{in\theta}e^{ikz}\left(\frac{\bar{\alpha}}{\omega}\right)\left[\tilde{C}_n(k,\omega)H_n^{(1)}(q_{sh} r) + \tilde{D}_n(k,\omega)J_n(q_{sh} r)\right] \\
\Gamma &= e^{in\theta}e^{ikz}\left(\frac{\bar{\alpha}}{\omega}\right)\left(\frac{\bar{\beta}}{\omega}\right)\left[\tilde{E}_n(k,\omega)H_n^{(1)}(q_{sv} r) + \tilde{F}_n(k,\omega)J_n(q_{sv} r)\right] \qquad (4.19)
\end{aligned}$$

where $\bar{\alpha}, \bar{\beta}$ are the average compressional and shear velocities of all layers. In such formulation, the coefficients $\tilde{A}_n(k,\omega) \cdots \tilde{F}_n(k,\omega)$ all have units of length and their magnitude can be directly compared with each other. For the TI case, where there are two shear velocities for the final layer, we choose the shear vertical, Sv, as $\bar{\beta}$.

Furthermore, as described in detail in Ricks (1994) it is essential for numerical stability to further normalize the displacement potentials. A valid solution to the acoustic wave equation can be generated from any set of functions of wavenumber and frequency for the constants $\tilde{A}_n(k,\omega) \cdots \tilde{F}_n(k,\omega)$. We are thus free to multiply or divide by any function of k, ω. For numerical stability the goal is to avoid any exponentially large or small numbers that would lead to computational overflow or prevent matrix inversion because of the near singular value of some of its elements. Thus, we choose the parametrization for the potentials in layer j, i.e., for $R_j \geq r \geq R_{j-1}$,

$$\Phi = e^{in\theta}e^{ikz}\left(\frac{\bar{\alpha}}{\omega}\right)\left[A_n(k,\omega)\frac{H_n^{(1)}(q_p r)}{H_n^{(1)}(q_p R_{j-1})} + B_n(k,\omega)J_n(q_p r)H_n^{(1)}(q_p R_j)\right] \qquad (4.20)$$

$$\chi = e^{in\theta}e^{ikz}\left(\frac{\bar{\alpha}}{\omega}\right)\left[C_n(k,\omega)\frac{H_n^{(1)}(q_{sh} r)}{H_n^{(1)}(q_{sh} R_{j-1})} + D_n(k,\omega)J_n(q_{sh} r)H_n^{(1)}(q_{sh} R_j)\right] \qquad (4.21)$$

$$\Gamma = e^{in\theta}e^{ikz}\left(\frac{\bar{\alpha}}{\omega}\right)\left(\frac{\bar{\beta}}{\omega}\right)\left[E_n(k,\omega)\frac{H_n^{(1)}(q_{sv}r)}{H_n^{(1)}(q_{sv}R_{j-1})} + F_n(k,\omega)J_n(q_{sv}r)H_n^{(1)}(q_{sv}R_j)\right] \tag{4.22}$$

For imaginary values of $q = q_{p,sh,sv}$, i.e. for large wavenumber k, the Bessel function $H_n^{(1)}(qr)$ is exponentially large while $J_n(qr)$ is exponentially small. With the above normalization, and in the large wavenumber region of evanescent waves, this ensures that no exponentially large or small displacement potential is obtained near either boundaries as $r \rightarrow R_{j-1}$ or $r \rightarrow R_j$.

To summarize, the displacement potentials in the LWD model shown in Fig. 4-1, are given by the following.

Inner Fluid: j=1

$$\Phi^{FI} = e^{in\theta}e^{ikz}\left(\frac{\bar{\alpha}}{\omega}\right)\left[B_n^{FI}J_n(q_p^{FI}r)H_n^{(1)}(q_p^{FI}R_j)\right] \tag{4.23}$$

Tool: j=2

$$\left.\begin{array}{c}\Phi^T\\ \chi^T\\ \Gamma^T\end{array}\right\} = e^{in\theta}e^{ikz}\left(\frac{\bar{\alpha}}{\omega}\right)\left\{\begin{array}{c} A_n^T\frac{H_n^{(1)}(q_p^T r)}{H_n^{(1)}(q_p^T R_{j-1})} + B_n^T J_n(q_p^T r)H_n^{(1)}(q_p^T R_j)\\ C_n^T\frac{H_n^{(1)}(q_{sh}^T r)}{H_n^{(1)}(q_{sh}^T R_{j-1})} + D_n^T J_n(q_{sh}^T r)H_n^{(1)}(q_{sh}^T R_j)\\ \left(\frac{\bar{\beta}}{\omega}\right)\left[E_n^T\frac{H_n^{(1)}(q_{sv}^T r)}{H_n^{(1)}(q_{sv}^T R_{j-1})} + F_n^T J_n(q_{sv}^T r)H_n^{(1)}(q_{sv}^T R_j)\right]\end{array}\right. \tag{4.24}$$

Outer Fluid: j=3

$$\Phi^{FO} = e^{in\theta}e^{ikz}\left(\frac{\bar{\alpha}}{\omega}\right)\left[A_n^{FO}\frac{H_n^{(1)}(q_p^{FO}r)}{H_n^{(1)}(q_p^{FO}R_{j-1})} + B_n^{FO}J_n(q_p^{FO}r)H_n^{(1)}(q_p^{FO}R_j)\right] \tag{4.25}$$

Transversely Isotropic Formation: j=4

$$\left.\begin{array}{c}\Phi^F\\ \chi^F\\ \Gamma^F\end{array}\right\} = e^{in\theta}e^{ikz}\left(\frac{\bar{\alpha}}{\omega}\right)\left\{\begin{array}{c} A_n^F\frac{H_n^{(1)}(q_p^F r)}{H_n^{(1)}(q_p^F R_{j-1})} + b'E_n^F\frac{H_n^{(1)}(q_{sv}^F r)}{H_n^{(1)}(q_{sv}^F R_{j-1})}\\ C_n^F\frac{H_n^{(1)}(q_{sh}^F r)}{H_n^{(1)}(q_{sh}^F R_{j-1})}\\ \left(\frac{\bar{\beta}}{\omega}\right)\left[a'A_n^F\frac{H_n^{(1)}(q_p^F r)}{H_n^{(1)}(q_p^F R_{j-1})} + E_n^F\frac{H_n^{(1)}(q_{sv}^F r)}{H_n^{(1)}(q_{sv}^F R_{j-1})}\right]\end{array}\right. \tag{4.26}$$

4.2 Boundary Conditions

The boundary conditions are determined by the type of interface, e.g. fluid-fluid, fluid-solid, fluid-vacuum etc. The boundary conditions at each interface are the continuity of radial displacement and stress, and the vanishing of shear stresses written as,

$$\begin{aligned} u^{lhs}(R_j) &= u^{rhs}(R_j) \\ \sigma_{rr}^{lhs}(R_j) &= \sigma_{rr}^{rhs}(R_j) \\ \sigma_{r\theta}^{lhs}(R_j) &= \sigma_{r\theta}^{rhs}(R_j) \\ \sigma_{rz}^{lhs}(R_j) &= \sigma_{rz}^{rhs}(R_j) \end{aligned} \tag{4.27}$$

Where R_j is the radius of the interface and lhs and rhs denote the medium to the left and right hand side of the interface. These four equations let us relate the displacement coefficients on the left to those on the right. Applying these boundary conditions at the three interfaces in our model, figure 4-1 gives rise to a system of twelve equations with twelve unknown displacement coefficients $\mathbf{C_n} = \left\{B^{FI}, A^T, B^T, C^T, D^T, E^T, F^T, A^{FO}, B^{FO}, A^F, C^F, D^F\right\}$. In matrix notation we can write it as follows

$$\mathbf{M_n C_n} = \mathbf{S_n} \tag{4.28}$$

where $\mathbf{S_n}$ defines the vector of displacement and stresses due to the presence of a source. To find the dispersion characteristics of the modes in the system we solve the system in the absence of source

$$\mathbf{M_n C_n} = 0 \tag{4.29}$$

which implies that

$$\det \mathbf{M}(k, \omega) = 0 \tag{4.30}$$

where the elements of M can be found in appendix B. The calculation itself is relatively straight forward from an algorithm standpoint. Once the equations and boundary conditions are correctly established the main areas of difficulty are the book-keeping aspects. As a general overview the computation follows the basic recipe of;

1) establish the number and type of layers to fix the number of constants needed to be solved for.

2) establish the interface types in the model and therefore the boundary conditions and relevant equations.

3) Build the matrix **M**.

4) The modes can be seen on the plot of $|\mathbf{M}|$ as a function of frequency and wavenumber, either in phase or magnitude, and can be extracted using root search methods.

4.3 Modeling Results

In this section we present the results for both wireline and LWD cases in isotropic and TI formations. Cases were chosen to represent both fast and slow formations. The elastic constants for the stiffness matrix are taken from Thomsen (1986) for the Mesaverde Shale, for the fast formation, and the Pierre shale, for the slow formation. Table 4.3 gives the parameters used in each case. The shear vertical, Sv, velocities were used as the reference isotropic case. In each model a borehole diameter of 8.75" (0.22m) was used and figure 4-2 shows the radial specifications and material parameters of the modeled LWD tool. We model the wireline case as a fluid filled borehole with no tool. Introducing any steel body into the borehole center will excite a similar set of tool modes to those seen in the LWD case. Although adding a steel pipe would approximate the wireline radial geometry, it does not capture the full damping of the tool modes allowed by the geometry of the tool along the z-axis. As mentioned in the discussion of wireline tools in the introduction, the body of the wireline sonde employs various methods to damp out any tool arrivals making it is reasonable to use the simpler model of a fluid filled borehole to approximate the wireline case. However the radial geometry of the LWD tool must be included because a similarly effective damping of the tool modes is not possible.

	Fast: Mesaverde Shale	Slow: Pierre Shale
V_p $[ms^{-1}]$	3901	2202
V_{Sv} $[ms^{-1}]$	2682	969
V_{Sh} $[ms^{-1}]$	2614	940
ϵ	0.137	0.015
δ	-0.078	0.085
γ	0.026	0.030
C_{11} $[GPa]$	31.53	10.59
C_{13} $[GPa]$	-1.21	7.57
C_{33} $[GPa]$	40.17	10.91
C_{44} $[GPa]$	18.99	2.11
C_{66} $[GPa]$	18.05	1.99
ρ $[kgm^3]$	2640	2250

Table 4.1: Thomsen parameters and equivalent elastic constants for Mesaverde (fast) and Pierre (slow) shales

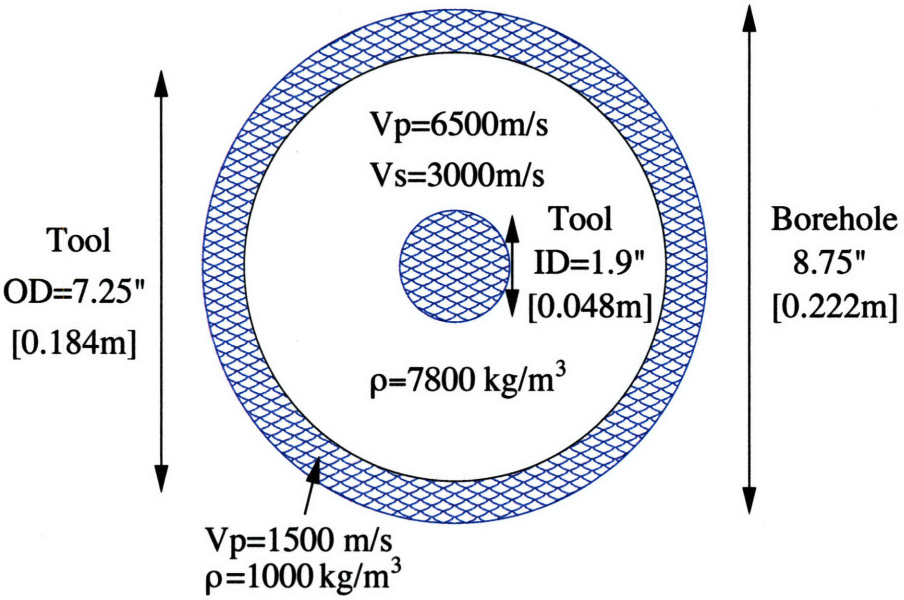

Figure 4-2: Cross sectional view of the model used in the LWD case and the material parameters.

4.3.1 Monopole

Figures 4-3, 4-4, 4-5,and 4-6 show the modal response of the borehole system to a monopole excitation for the wireline and LWD tool radial geometries in slow and fast isotropic and transversely isotropic formations.

Wireline

The Stoneley wave is present in both the slow and fast formations but the higher order pseudo-Rayleigh is only seen in the fast formation. In the slow case the axisymmetric Stoneley mode shows direct dispersion, i.e. the phase velocity decreases with frequency, while in the fast case the Stoneley dispersion is reverse. The zero frequency asymptote of the Stoneley mode is given by;

$$C_{st} = \alpha_1 \left(1 - \frac{r_{tool}^2}{r_{borehole}^2}\right)^{1/2} \left(1 - \frac{r_{tool}^2}{r_{borehole}^2} + \frac{\rho_1 \alpha_1^2}{\rho_2 \beta_2^2}\right)^{-1/2} \tag{4.31}$$

where 1 and 2 refer to the material properties of the borehole fluid and formation respectively.

In the open borehole case this reduces to;

$$C_{st} = \alpha_1 \left(1 + \frac{\rho_1 \alpha_1^2}{\rho_2 \beta_2^2}\right)^{-1/2} \tag{4.32}$$

Schmitt (1988a) and personal communication. The high frequency limit, when the mode sees the borehole wall as an infinite planar fluid-solid interface, is given by the Scholte velocity. The zero frequency asymptote of the Stoneley mode given in equation 4.32, for this particular Pierre Shale formation, is below the fluid compressional velocity and the Scholte wave velocity, which is always less than the shear velocity of the formation, is even lower. These two asymptotes define the direct dispersion seen in figure 4-3. These asymptotes are not the same for the TI case. At low frequencies the difference between the isotropic and TI case is smaller than for high frequencies. This implies that the low frequency phase velocities are less sensitive to the shear horizontal velocities given by the C_{66} in the stiffness matrix than the high frequencies Schmitt (1989), figure 8b.

For the Mesaverde shale, the fast formation, the isotropic and TI cases are much closer in phase velocity at all frequencies and the dispersion is now reversed. In a fast formation the Stoneley mode is poorly coupled to the formation, meaning the bulk of the modes energy is associated with the borehole fluid making it much less sensitive to formation properties. This is evident from the marginal change in phase velocities seen between the isotropic and TI case in figure 4-4. The dispersion is defined by the same low and high frequency asymptotes as previously discussed but here the zero frequency Stoneley phase velocity is less than that of the Scholte velocity, which results in the reverse dispersion.

LWD

Figures 4-5 and 4-6 show the monopole case for the LWD tool in the slow and fast formations given in table 4.3. With the addition of the tool in the borehole both Stoneley wave dispersions are now reverse. Equation 4.31 gives the zero frequency

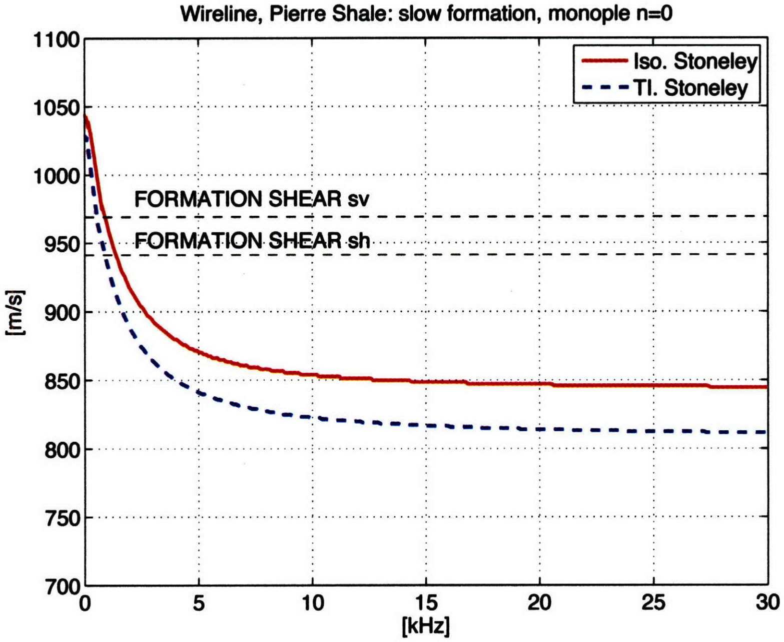

Figure 4-3: Wireline, Monopole Source, dispersion characteristics of the phase velocity of the modes obtained in the presence of a slow isotropic and slow transversely isotropic formation. At very low frequencies (where C > Vs) the Stoneley wave may be "leaky".

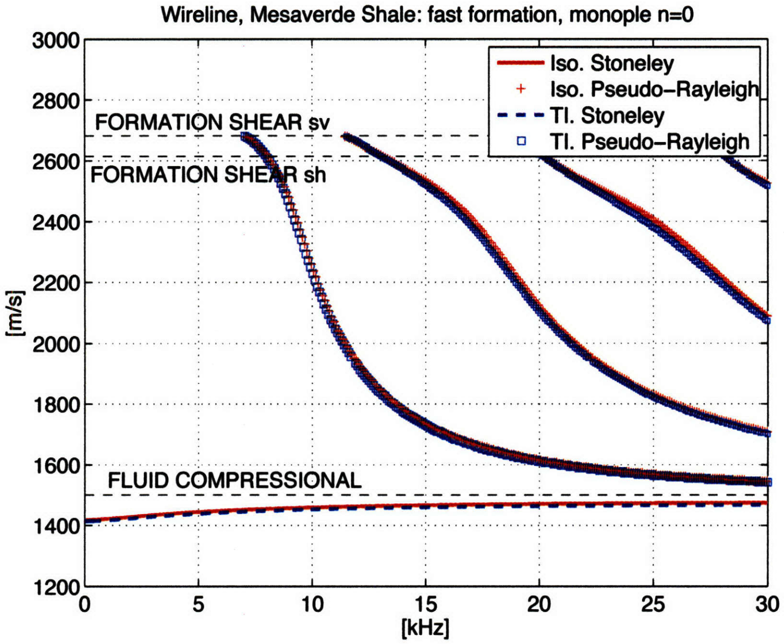

Figure 4-4: Wireline, Monopole Source, dispersion characteristics of the phase velocity of the modes obtained in the presence of a fast isotropic and fast transversely isotropic formation

phase velocity of the Stoneley when a tool is present. By inspection we see that the addition of a tool in the borehole will push the zero crossing lower as the radius of the tool is always less than that of the borehole. The high frequency asymptote is the again the Scholte wave velocity. Again the poor coupling of th"e Stoneley wave to the formation velocities can be seen as the relatively small change in phase velocity between the isotropic and TI cases.

4.3.2 Dipole

Figures 4-7, 4-8, 4-9 and 4-10 show the modal response of the borehole system to a dipole excitation for the wireline and LWD radial tool geometries. The formation parameters used for the fast and slow shales are given in 4.3

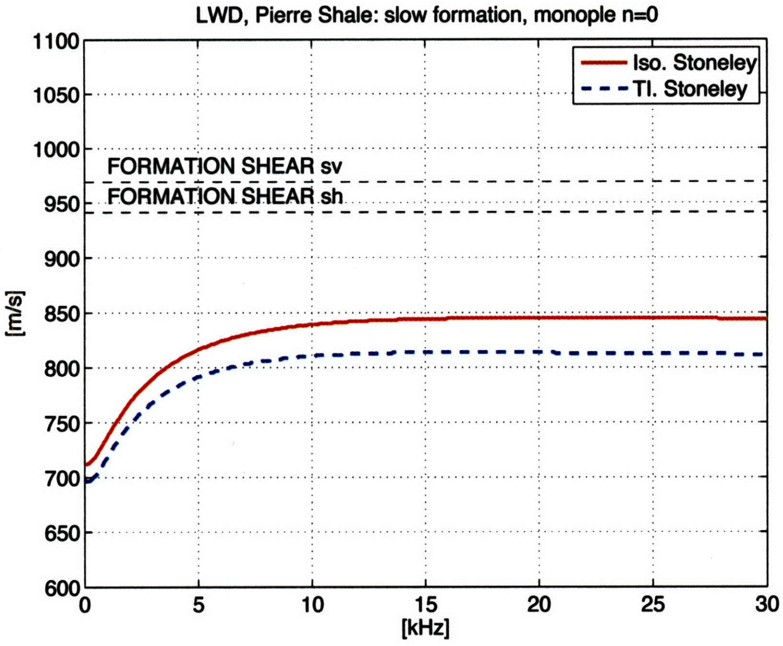

Figure 4-5: LWD, Monopole Source, dispersion characteristics of the phase velocity of the modes obtained in the presence of a slow isotropic and slow transversely isotropic formation

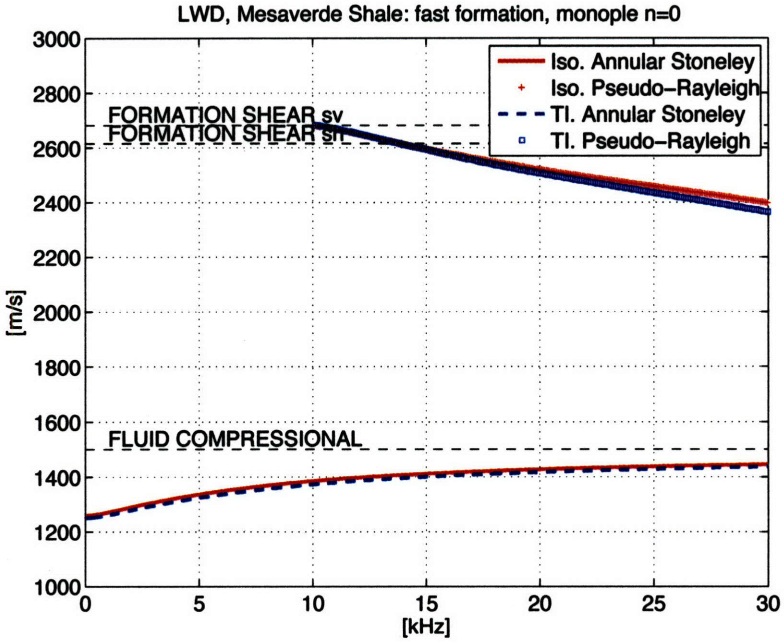

Figure 4-6: LWD, Monopole Source, dispersion characteristics of the phase velocity of the modes obtained in the presence of a fast isotropic and fast transversely isotropic formation

Wireline

The wireline case in the slow formation with a dipole source excited the fundamental flexural mode. This mode exists at all frequencies and is analogous to the fundamental Stoneley mode seen in the monopole case. In the fast formation both the fundamental flexural mode and higher order flexural modes are generated. The higher order flexural modes can be seen in figure 4-8 and have cutoff frequencies corresponding to critical refraction of the waves. Comparing the fundamental flexural mode in the fast formation with that in the slow formation shows again the reduced coupling of modal energy to the formation for the fast formation and, in the slow case, how the higher frequency phase velocities are greater influenced by the slower Sh velocity than the low frequencies. This is evident form the greater difference in phase velocities between the isotropic and TI medium at high frequencies that at low frequencies.

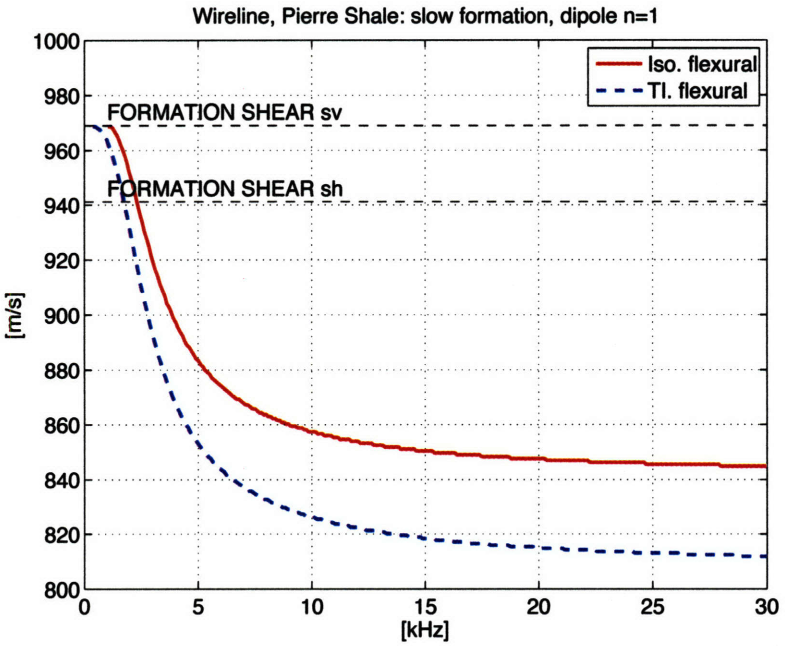

Figure 4-7: Wireline, Dipole Source, dispersion characteristics of the phase velocity of the modes obtained in the presence of a slow isotropic and slow transversely isotropic formation

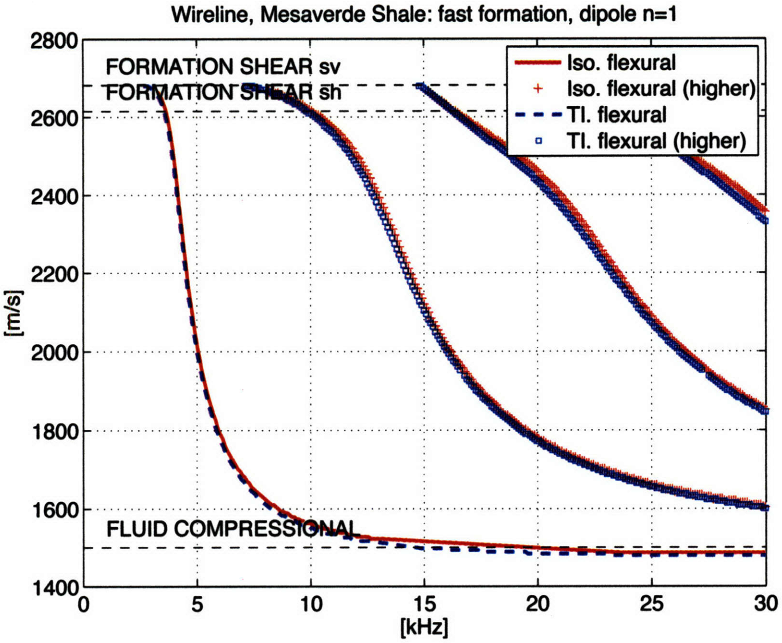

Figure 4-8: Wireline, Dipole Source, dispersion characteristics of the phase velocity of the modes obtained in the presence of a fast isotropic and fast transversely isotropic formation

LWD

In the LWD case the flexural mode is forced to zero phase velocity at zero frequency resulting from the interaction of the tool flexural mode. This can be clearly seen in figures 4-9 and 4-10. The peak of the formation flexural mode is shifted to higher frequencies in the fast formation case. This peak indicates where the tool flexural and formation flexural modes avoid crossing. In the fast formation the peak shifts to higher velocities as the angle of critical refraction increases for faster formation velocities. The high frequency asymptote is the Scholte velocity which is close to the borehole fluid velocity in the fast formation and below the formation shear velocities in the slow formation.

4.3.3 Quadrupole

Figures 4-11, 4-12, 4-13,and 4-14 show the modal response of the borehole system to a quadrupole excitation for the wireline and LWD tool radial geometries in the same

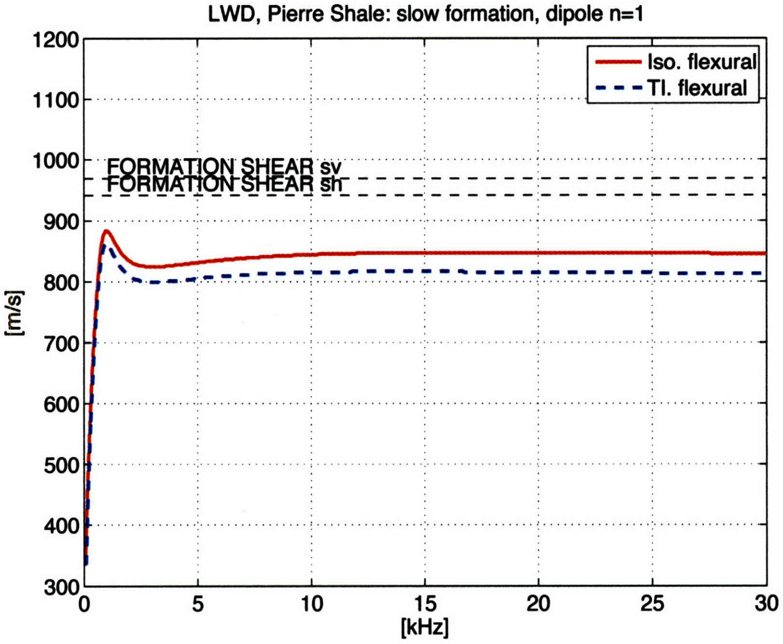

Figure 4-9: LWD, Dipole Source, dispersion characteristics of the phase velocity of the modes obtained in the presence of a slow isotropic and slow transversely isotropic formation

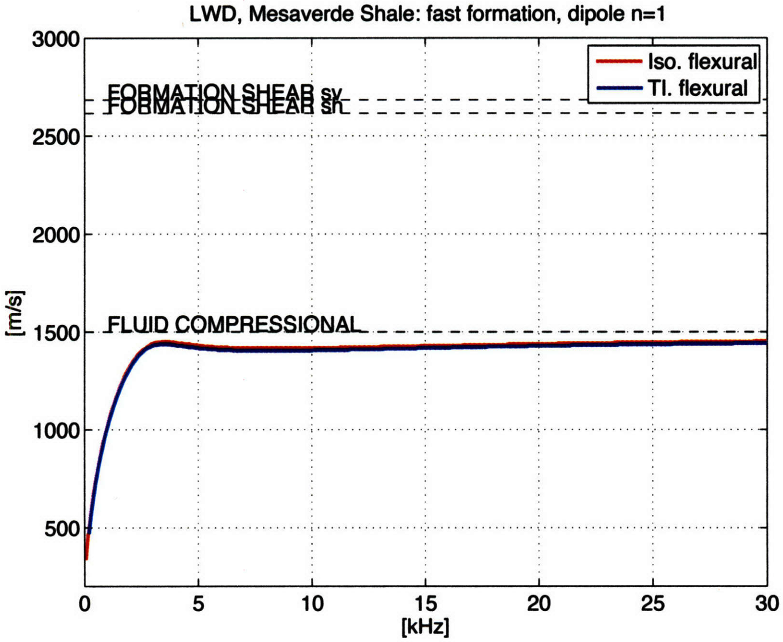

Figure 4-10: LWD, Dipole Source, dispersion characteristics of the phase velocity of the modes obtained in the presence of a fast isotropic and fast transversely isotropic formation

slow and fast formations seen in the above two sections.

Wireline

The fundamental mode excited by a quadrupole source is the screw mode. Figures 4-11 and 4-12 show the screw modes for the wireline case in the slow and fast formations. The fundamental screw modes have no cutoff and asymptote to the shear velocity at low frequencies. The appearance of a cutoff for this mode is due to a coalescence of the pole with the shear refracted wave branch point. The higher screw modes present in the fast formation, analogous to the higher flexural and pseudo-Rayleigh modes do have a cutoff frequency which can be seen in figure 4-12. In both the fast and slow formations the high frequency asymptote is the Scholte velocity but the screw mode asymptotes to this at higher frequencies than for the monopole or dipole cases. Similarly to the monopole and dipole cases, the poor coupling of the interface modes to the formation properties in a fast formation can be seen by the relatively small change in phase velocities between the isotropic and TI cases. The slow formation again demonstrated that it is not only more sensitive to the formation shear velocities but the sensitivity to the Sh velocity increases with frequency.

LWD

The quadrupole excitation for the LWD case is shown in figures 4-13 and 4-14. In both the fast and slow formation the screw mode asymptotes to the formation shear velocity. In the dipole LWD case the tool flexural mode interacts with the formation flexural causing it to zero phase velocity at zero frequency. In the quadrupole case the tool screw mode is at much higher phase velocities and therefore does not interact with the formation screw mode. This suggests that the quadrupole mode is better suited as an estimator of formation shear velocities than the dipole data seen in previous chapters. Similarly to the previous cases we see the relatively small change between the isotropic and TI for the fast formation.

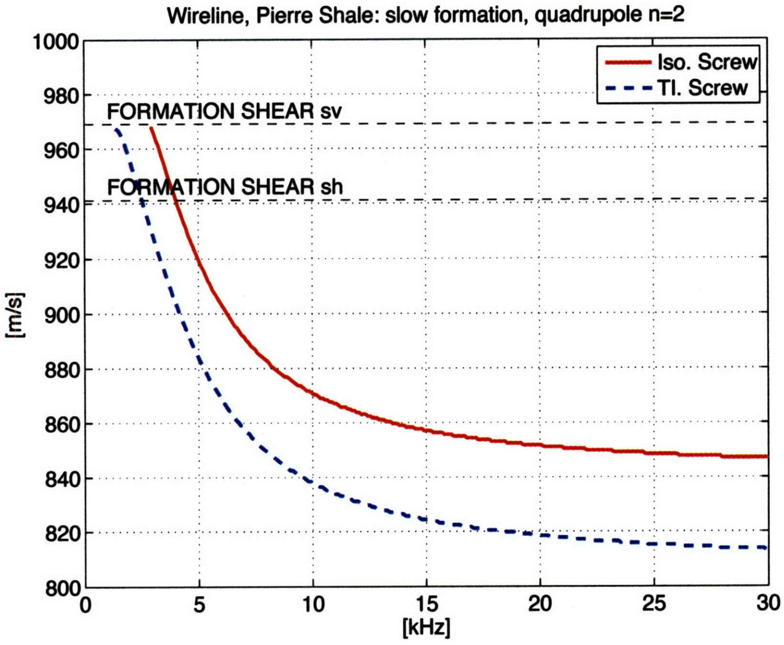

Figure 4-11: Wireline, Quadrupole Source, dispersion characteristics of the phase velocity of the modes obtained in the presence of a slow isotropic and slow transversely isotropic formation

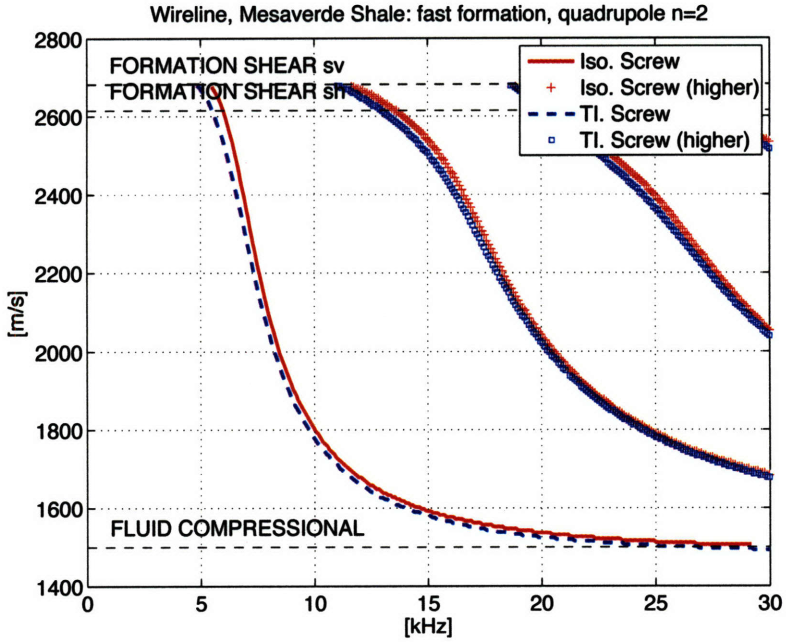

Figure 4-12: Wireline, Quadrupole Source, dispersion characteristics of the phase velocity of the modes obtained in the presence of a fast isotropic and fast transversely isotropic formation

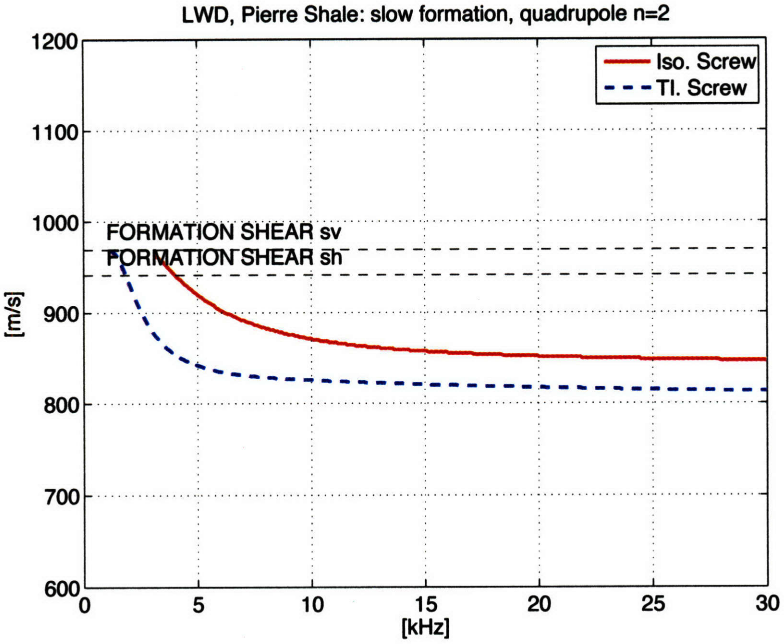

Figure 4-13: LWD, Quadrupole Source, dispersion characteristics of the phase velocity of the modes obtained in the presence of a slow isotropic and slow transversely isotropic formation

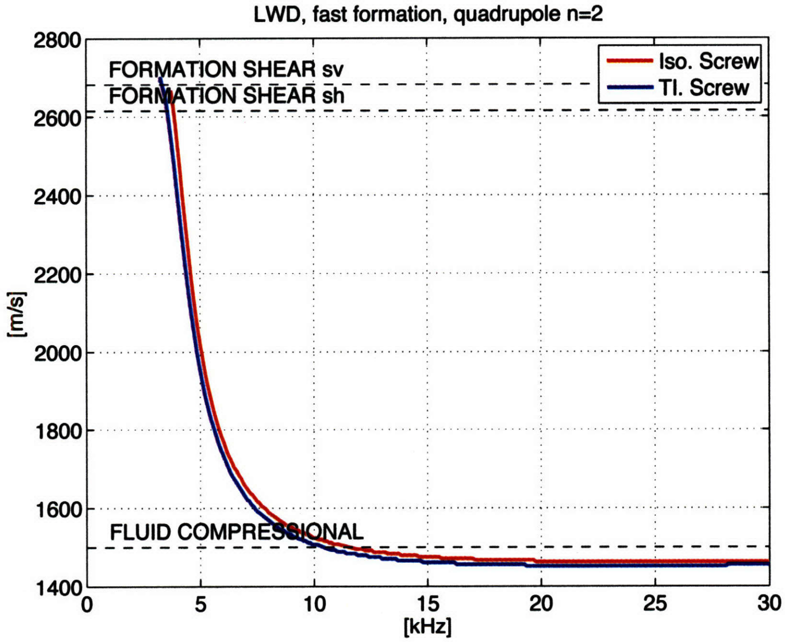

Figure 4-14: LWD, Quadrupole Source, dispersion characteristics of the phase velocity of the modes obtained in the presence of a fast isotropic and fast transversely isotropic formation

4.4 Conclusions

The modeled results shown in the previous sections can be compared in several ways. Firstly comparing slow and fast isotropic and TI formations, we note that the fundamental modes are excited in both cases but the higher order modes are only excited in the fast case. The coupling of the modal energy to the fast formation is poor and therefore relatively insensitive to the TI medium. In the slow formation the the modes are sensitive the to the TI parameters, specifically the Sv, C_{66} at low velocities and the Sh, C_{44} at high velocities.

Secondly comparing the wireline and LWD modes. The presence of a tool in the borehole reduces the fluid annulus, giving the effect of reducing the borehole diameter. In general this means a shifting of modes to higher frequencies as. In the dipole case the formation flexural modes is greatly affected by the presence of the tool flexural mode and shows a dramatic change in mode character compared to its wireline counterpart. The presence of the tool also changes the low frequency asymptote of the monopole Stoneley mode sufficiently so that the direct dispersion seen in the wireline case is now reversed.

Lastly we compare the monopole, dipole and quadrupole modes. In terms of extracting a modal phase velocity that is representative of the formation shear the screw mode (n=2) gives the most direct result in both the wireline and LWD cases. In a fast formation the formation shear is calculated from the refracted shear arrival and further shear modal analysis is unnecessary. In a slow formation there is no refracted shear wave and the shear velocity is estimated from a modal arrival. In the wireline case the dipole flexural mode is sufficient but the interaction of the tool flexural mode in the LWD case complicates the shear velocity pick. The quadrupole screw mode is not affected by the tool flexural mode and so the low frequency asymptote requires no correction. Additionally the low frequency screw mode asymptote is at higher frequencies for the LWD tool, compared with the dipole case, which moves it away from the frequency band at which the drilling noise and mud circulation can cause contamination.

Chapter 5

Conclusions

The goal of this thesis is the determination of formation compressional and shear velocities obtained from two acoustic logging tools, wireline and LWD. The thesis includes: the formation and numerical computation of acoustic wave propagation in a borehole environment for LWD and wireline geometries, the analysis of data from wireline and LWD measurements taken in the same borehole, and comparisons of the results. In addition the modeling is extended to transversely isotropic media such as those commonly found in layered sediments.

We have compared LWD and wireline tools both using actual logging data and numerical modeling of acoustic modes in the borehole. Traditional time-semblance processing of the data leads to differences in estimated velocities for these two tools. We found that for the purpose of comparing the measurements of the wireline and LWD tools, time-semblance analysis could be inadequate. Time semblance methods fail in the presence of dispersive arrivals and only frequency-domain methods reveal the full modal dispersion. We found that a frequency-domain analysis is feasible and reduces the overall difference between the LWD and wireline shear and compressional velocity estimates. The remaining discrepancy can be explained by the different radial depths of penetration of these two tools, which naturally leads to a difference in the velocity estimates when there is a radial gradient in the velocity profile.

The remaining difference in the velocity estimates from wireline and LWD tools data can be explained by radial gradient in the velocity profile of the formation.

This kind of radial velocity gradient causes dispersion in otherwise non-dispersive refracted arrivals and increases or decreases the expected dispersion in modal arrivals. Any method used to process the waveforms for formation speeds that assumes a fixed correction for modal dispersion, or assumes that the head waves are non-dispersive, will incorrectly calculate formation properties. The argument is extended to show that the different operating frequencies and source-receiver offsets of the tools give differing measurement penetration depths, so that discrepancies between the tool logs is expected in certain types of formations.

In chapter 4, we presented a method to model seismic wave propagation in a a radially multi-layered borehole model with an outermost transversely isotropic formation. The inner model layers may be any combination of isotropic solids and fluids. Each layer is defined by its velocities, density and thickness. The TI medium is defined by the five elastic constants, $C_{11}, C_{33}, C_{13}, C_{44}$ and C_{66} or the three Thomsen parameters ϵ, γ and δ. The model allows us to calculate the modal arrivals as a function of phase velocity and frequency. This is used to study the modes of interest when extracting formation properties from acoustic logging data.

The code was used to model the LWD tool in a TI formation and compare it to the wireline case.Inspection of the modal dispersion profiles in fast and slow formations reveals that the LWD measurement, due to its frequency range of operation, is unsuited to differentiate a TI formation from an isotropic one. This limitation is by no means fundamental but results from the presence of acoustic noise at low frequency and the resulting constraint of operating in a range of frequencies sufficiently greater than that of the noise. Sophisticated signal processing, noise reduction and or rejection techniques, as well as improved transducer design would enable the operation of the tool at significantly lower frequencies. Our analysis demonstrates that at a lower frequency of operation, the LWD tool can potentially measure the effect of a TI medium in the fundamental shear modes, especially in the low velocity formations

In summary the future of borehole measurements is pushing towards LWD technology as the savings in exploration time are significant. As this trend progresses, it becomes increasingly important to understand the LWD measurements accurately. Borehole acoustics, although a well developed area of research for wireline tools, is still an active and ongoing area of research for the LWD case. We have made two important contributions in this field with the work presented in this thesis. Firstly, we have made an independent comparison of LWD and wireline data for a formation where traditional processing methods gave significantly different results for velocity estimates in LWD and wireline tools. We have suggested a possible explanation as to why these estimates can differ and how current time-domain based velocity processing methods may be improved by using frequency-domain methods. Secondly, we have a developed a detailed model of the LWD modes in a TI formation. This understanding stemming from this model is consequential to exploration geophysics, as reservoirs lie in sedimentary basins where the thinly layered strata result in a predominantly TI medium.

Appendix A

Simple model using two fluids

In this appendix we derive the equations needed to solve the canonical form of the borehole mode problem using a fluid filled borehole surrounded by a fluid formation. A fluid-fluid model excites only the compressional modes therefore reducing the number of constants and equations needed to describe them. Although this simplifies the mathematics significantly the model gives insight into the more complicated multi-elastic layer problem and is sophisticated enough to illustrate the method of solution for the full LWD case.

The fluid-fluid model is illustrated in figure A-1

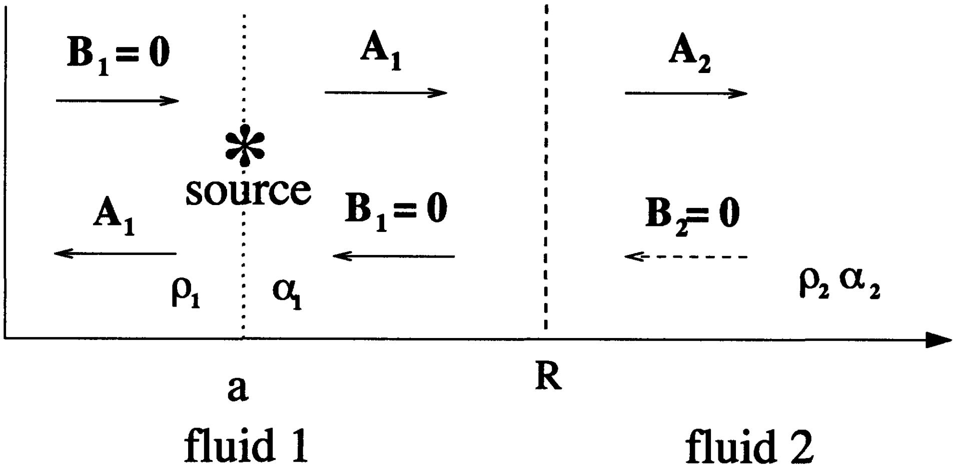

Figure A-1: Fluid-fluid Model

The basic recipe for solving the problem mathematically is the same. First, we assume a potential wavefield in both media which consist of incoming and outgoing waves. Then, boundary conditions are applied at the interface allowing us to solve for the amplitude constants in the potential equations. Once we have the constants, we have the full potential wavefield solution. This can then be used to calculate seismograms. Before the method for seismogram calculation is shown (time vs offset), this section will concentrate on understanding the modes arising from a single interface and how they can be interpreted. In cylindrical coordinates, we have cylindrical waves, whose radial dependence contains Bessel functions. The potential can be separated into the radial dependence given by $A_n K_n(fr) + B_n I_n(fr)$ and the z dependence given by e^{ikz} The third axis in cylindrical coordinates is the azimuthal dependence which is determined by the order of the source e.g. monopole, dipole, quadropole etc., and is given by $\cos n\theta$, where n is the pole order. The formulation assumes a ring source which is comprised from an infinite number of point sources along a ring of radius a. We will discuss the source term further in the next section when calculating the seismograms. The potential solution in medium 1 is written as

$$\Phi_1 = \left[A_1 K_n(f_1 r) + B_1 I_n(f_1 r)\right] e^{ikz} \cos n\theta \tag{A.1}$$

and similarly for medium 2

$$\Phi_2 = \left[A_2 K_n(f_2 r) + B_2 I_n(f_2 r)\right] e^{ikz} \cos n\theta \tag{A.2}$$

where A is the amplitude of the outgoing wave and B the amplitude of the incoming wave, k is the axial wavenumber, and $f = \left(k^2 - k_f^2\right)^{\frac{1}{2}}$ is the radial wave number. The boundary conditions applied at R, are displacement and pressure continuity:

$$\begin{aligned} u &= \frac{\partial \Phi}{\partial r} && \text{(A.3)} \\ \sigma_{rr} &= -\rho\omega^2 \Phi && \text{(A.4)} \end{aligned}$$

are continuous across the interface,

$$u_1 = u_2 \tag{A.5}$$

$$\sigma_{rr,1} = \sigma_{rr,2} \tag{A.6}$$

from A.3, u_i is given by

$$u_i = \cos n\theta e^{ikz}\left(A_i[\frac{n}{r}K_n(f_ir) - f_iK_{n+1}(f_ir)] + B_i[\frac{n}{r}I_n(f_ir) + f_iI_{n+1}(f_ir)]\right) \tag{A.7}$$

and $\sigma_{rr,i}$ is

$$-\rho\omega^2\Phi_i = \left[A_iK_n(f_ir) + B_iI_n(f_ir)\right]e^{ikz}\cos n\theta \tag{A.8}$$

To solve for the eigenmodes of the system, we use the so-called radiation conditions: we set $B_2 = 0$, the wave is only outgoing in medium 2 and $A_1 = 0$, since the wave potential should be finite at $r = 0$. In the absence of a source we can write:

$$[M]\begin{bmatrix} A_2 \\ B_1 \end{bmatrix} = 0 \tag{A.9}$$

where [M] is

$$\begin{bmatrix} -\left[\frac{n}{r}I_n(f_1r) + f_1I_{n+1}(f_1r)\right] & \frac{n}{r}K_n(f_2r) - f_2K_{n+1}(f_2r) \\ \rho_1\omega^2I_n(f_1r) & -\rho_2\omega^2K_n(f_2r) \end{bmatrix} \tag{A.10}$$

Figure A-2 shows the modes for both monopole and higher order directional modes. This simple model illustrates the types of modes present in a cylindrical multilayer system and many features will also be present in the full model including tool and anisotropy. To find the eigenmodes of the system we set the determinant of M to zero. The determinant, set to zero, is given by;

$$-\rho_1\omega^2I_n(f_1r)\left(\frac{n}{r}K_n(f_2r) - f_2K_{n+1}(f_2r)\right) - \rho_2\omega^2K_n(f_2r)\left(\frac{n}{r}I_n(f_1r) + f_1I_{n+1}(f_1r)\right) = 0 \tag{A.11}$$

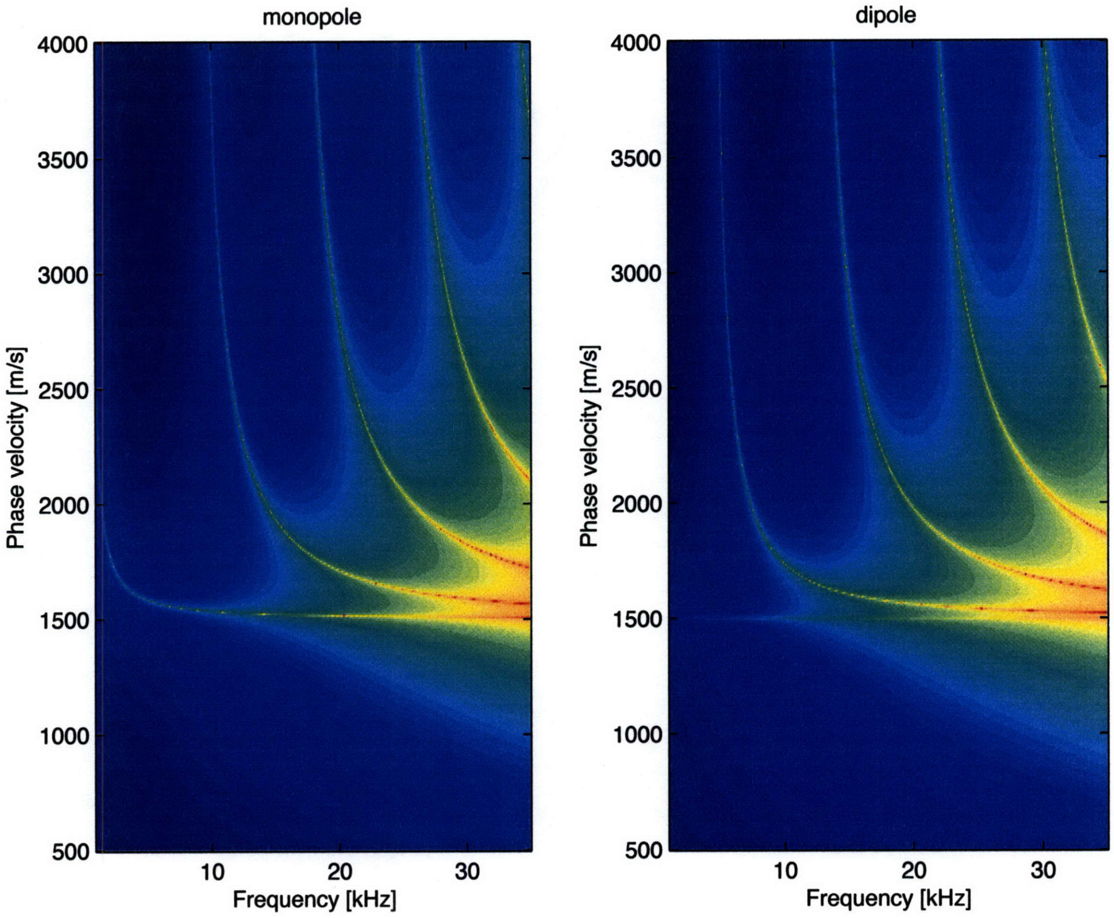

Figure A-2: Eigenmodes for n=0 (odd) and n=1 (even) modes. α_1=1500, α_2=12000, ρ_1=1000, ρ_2=10000, r=0.1

The modes arise when either the first term equals the second term or both terms equal zero independently. Because the system is relatively simple we can derive the modes analytically. The first and simplest mode can be seen at all frequencies at a phase velocity of α_1. This mode is non-dispersive and arises when $f_1 = 0$. (N.B the mode is somewhat obscured at low frequencies for the n=1 case in figure A-2 but it is still present). The modified Bessel function of first kind, I_n is zero at the origin, therefore when $f_1 = 0$ both the first and second terms of equation A.11 will be zero and it therefore follows that the determinant of M will be zero.
For both the monopole and dipole case there are modes which appear above certain discrete cutoff frequencies. If we consider the extreme case where $\rho_2 \gg \rho_1$, i.e. the outer layer is much more dense resulting in a large difference of mechanical impedance, we need only consider the term involving ρ_2 to first order, i.e. $[\rho_2\omega^2 K_n(f_2r)]\left[\frac{n}{r}I_n(f_1r) + f_1 I_{n+1}(f_1r)\right] \simeq 0$.

This occurs when f_1 is imaginary so that the Bessel function I_n is oscillatory and the term $nI_n(f_1r) + (f_1r)I_{n+1}(f_1r)$ has zeros. Physically this corresponds to the waves reflected from the interface interfering constructively, and giving rise to a standing wave-like mode. This happens at discrete frequencies corresponding to fitting increasing number of wavelengths within the borehole. This was described for the pseudo-Rayleigh mode by Schmitt and Bouchon Schmitt and Bouchon (1985). To understand in more details we look at $f_1 = \sqrt{k^2 - k_{\alpha_1}^2}$, which is imaginary when $|k| \leq |k_{\alpha_1}$. Moreover $f_1 = -i|f_1|$, i.e. the root corresponding to $\omega + i\epsilon$ where $\epsilon \to 0$. We thus find $nI_n(f_1r) + (f_1r)I_{n+1}(f_1r) = i^{-n}\left[nJ_n(|f_1r|) - |f_1r|J_{n+1}(|f_1r|)\right]$, which is oscillatory and has zeros which we'll denote by $x_{n,m}$ to denote the mth zero of the expression $F_n(x) = nJ_n(x) - xJ_{n+1}(x)$. For example, we find numerically $x_{0,j} \simeq \{0, 3.85, \cdots\}$, and $x_{1,j} = \{0, 1.85, \cdots\}$. Corresponding to these zeros, we find the modes $|f_1r| = x_{n,m}$, which we can re-arrange to give the wavevector

$$k_{n,m}(\omega) = \frac{1}{\alpha_1}\sqrt{\omega^2 - \left(\frac{x_{n,m}\alpha_1}{r}\right)^2} \qquad \text{(A.12)}$$

and the corresponding phase velocity

$$v_{n,m}(\omega) = \alpha_1 \frac{\omega}{\sqrt{\omega^2 - \left(\frac{x_{n,m}\alpha_1}{r}\right)^2}} \tag{A.13}$$

We can see from A.13 that for ω less than the cutoff frequency the phase velocity is purely imaginary, at the cutoff the mode has infinite phase velocity and finally when ω is large the phase velocity tends to α. These modes and their respective cutoff frequencies can be clearly seen in figure A-2.

Given the phase velocity we can calculate the group velocity which is given by $\frac{d\omega}{dk}$,

$$\omega = v_\phi k$$

differentiating with respect to ω gives

$$\begin{aligned} 1 &= \frac{dk}{d\omega} v_\phi + k \frac{dv_\phi}{d\omega} \\ &= \frac{v_\phi}{v_g} + \frac{\omega}{v_\phi} \frac{dv_\phi}{d\omega} \end{aligned} \tag{A.14}$$

which can be rearranged to give

$$V_g = \frac{v_\phi}{1 - \frac{\omega}{v_\phi}\frac{dv_\phi}{d\omega}} \tag{A.15}$$

By inspection we can see that when the slope of the phase velocity is high and positive the group velocity will be low and vice versa. At the cutoff $V_\phi \to \infty$ and $V_g \to 0$, this represents the radial oscillation of the source, while the wave does not propagate.

A.1 Wave number integration to calculate seismograms

In this section we show how the characteristic equation, shown in the last section, can be used to calculate synthetic seismograms for the model. In order to calculate the seismograms we must define a source. In this case we use a ring source placed at radius a. The source term is defined as

$$\Phi_{source}(k,\omega) = A_{source}(k,\omega) \begin{cases} I_n(fr)K_n(fa) & r < a \\ I_n(fa)K_n(fr) & r > a, \end{cases} \tag{A.16}$$

where $A_{source}(k,\omega)$ is the Fourier transform of the source time dependence. This is typically a Ricker or Kelly wavelet. Note that the angular dependence was assumed to be that of a multipole of order n, and assuming a detector suited to detect this multipole order only, we effectively integrate out the angular dependence, so that it is omitted from here on. The boundary conditions in equations A.5 and A.6 now become

$$U_1 + U_{source} = U_2 \tag{A.17}$$

$$\sigma_{rr,1} + \sigma_{source} = \sigma_{rr,2} \tag{A.18}$$

which leads to a system of equations similar to those seen in equation A.9 and with $[M]$ given by A.10

$$[M]\begin{bmatrix} A_2 \\ B_1 \end{bmatrix} = (-1)A_{source}\begin{bmatrix} \frac{n}{R}K_n(f_1R) - f_1K_{n+1}(f_1R)I_n(f_1a) \\ -\rho_1\omega^2K_n(f_1R)I_n(f_1a) \end{bmatrix} \tag{A.19}$$

Again solving for A_2 and B_1, which are both funtions of k and ω. This is plugged into the expression for the potential solution in equation A.1

$$\Phi_1(k,\omega,r,\theta) = A_2(k,\omega)I_n(f_1r)\cos n\theta \tag{A.20}$$

Thus, the radial stress σ_{rr} (i.e. the pressure in the fluid) can be calculated as a function of position in the borehole. Multiplying by $\cos n\theta$ and integrating over angles we thus have the stress induced in the fluid $\sigma_{rr}(r = a, k, \omega) = \rho\omega^2 A_2(k, \omega) I_n(f_1 r)$. Performing a double Fourier transform over wavenumber and frequency, we can obtain the seismograms, i.e., $\sigma_{rr}(r = a, z, t)$. Note that in order to properly treat the poles and branch cuts of the expression, we introduce a small imaginary part to the frequency ω before performing a double Fourier transform, see for example Tang and Cheng (2004) (this is the method used to generate the seismograms on figure A-3). Figure A-3 shows a calculated seismograms from a dispersion curve similar to those shown in A-2. The plot on the left shows the phase and calculated group velocities and the plots on the right shows the calculated seismograms. It is easy to see from these figures how the modeshape influences the character of the corresponding seismograms. It is instructive to see these modes, and their corresponding seismograms, one at a time as the complicated interaction of dispersion curves for a complete tool model make it hard to distinguish individual effects. In figure A-3 the mode comes from an infinite velocity at around 3.5 kHz and asymptotes to the inner fluid velocity of 1000 m/s. The group velocity has the opposite behavior. By looking at the corresponding seismograms we can see that the high frequencies precede the low frequencies, suggesting that the group velocity has the greater influence on the seismogram arrival and packet shape. If the shape of the dispersion curve was reversed we would expect to see the opposite behavior in the seismograms.

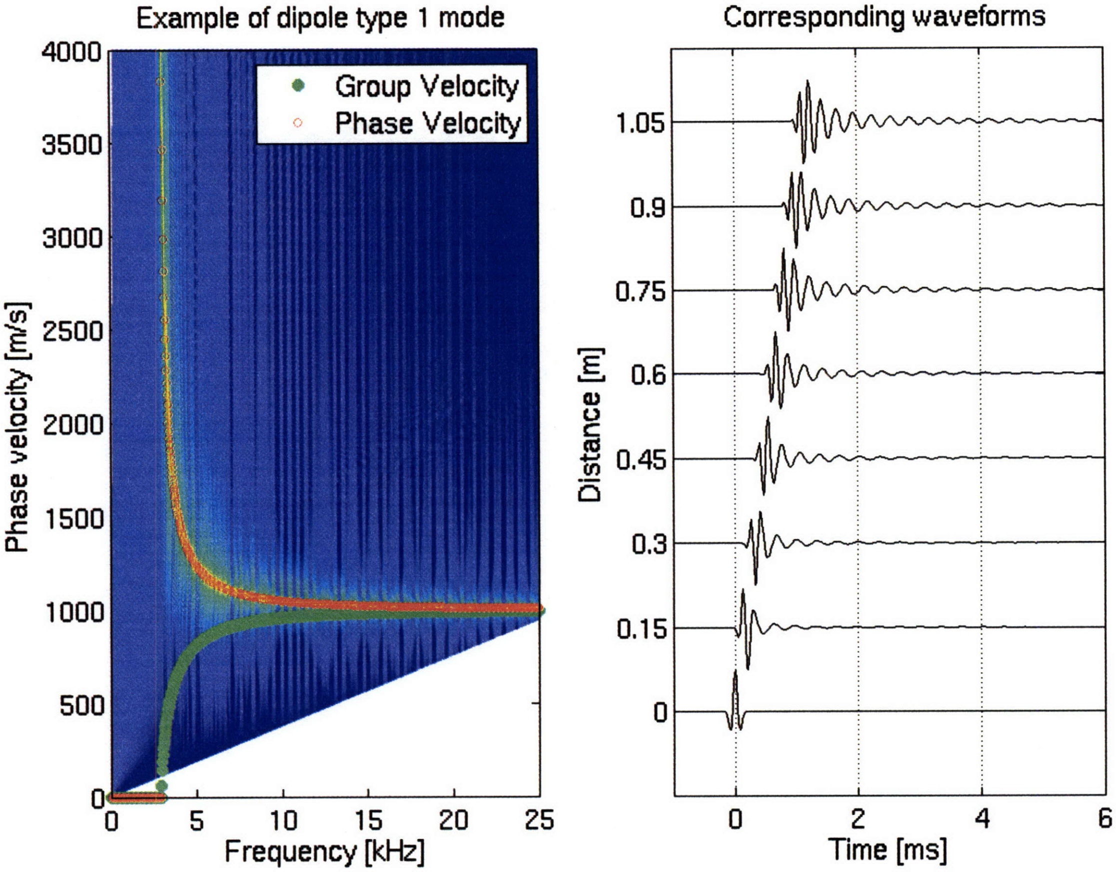

Figure A-3: The phase and group velocity of the first type of dipole and monopole mode excited in the simple model used in this appendix. The right hand side plot shows the corresponding waveforms.

Appendix B

Elements in M

This appendix lists the elements of **M** in chapter 4, equation 4.29 in full. The matrix M consists of the k and ω dependance of the equations derived from the stresses and boundary conditions. Here we show the full equations given in matrix form.
For the displacements, u, v and w, in medium j at radius R, shown in 4.3 we have

$$\begin{bmatrix} u \\ v \\ w \end{bmatrix} = \left[\mathbf{D}^{(j)}(R)\right] \cdot \begin{bmatrix} A^{(j)} \\ B^{(j)} \\ C^{(j)} \\ D^{(j)} \\ E^{(j)} \\ F^{(j)} \end{bmatrix} \qquad \text{(B.1)}$$

where

$$D_{1,1}^{(j)} = \frac{(\bar{\alpha}/\omega)}{R}\frac{\mathcal{Y}\mathcal{H}_1(n, q_p R)}{H_n^{(1)}(q_p R_{j-1})} \tag{B.2}$$

$$D_{1,2}^{(j)} = \frac{(\bar{\alpha}/\omega)}{R}\mathcal{Y}\mathcal{J}_1(n, q_p R) H_n^{(1)}(q_p R_j) \tag{B.3}$$

$$D_{1,3}^{(j)} = \frac{in(\bar{\alpha}/\omega)}{R}\frac{H_n^{(1)}(q_{sh} R)}{H_n^{(1)}(q_{sh} R_{j-1})} \tag{B.4}$$

$$D_{1,4}^{(j)} = \frac{in(\bar{\alpha}/\omega)}{R} J_n(q_{sh} R) H_n^{(1)}(q_{sh} R_j) \tag{B.5}$$

$$D_{1,5}^{(j)} = \frac{ik(\bar{\alpha}/\omega)(\bar{\beta}/\omega)}{R}\frac{\mathcal{Y}\mathcal{H}_1(n, q_{sv} R)}{H_n^{(1)}(q_{sv} R_{j-1})} \tag{B.6}$$

$$D_{1,6}^{(j)} = \frac{ik(\bar{\alpha}/\omega)(\bar{\beta}/\omega)}{R}\mathcal{Y}\mathcal{J}_1(n, q_{sv} R) H_n^{(1)}(q_{sv} R_j) \tag{B.7}$$

$$D_{2,1}^{(j)} = \frac{in(\bar{\alpha}/\omega)}{R}\frac{H_n^{(1)}(q_p R)}{H_n^{(1)}(q_p R_{j-1})} \tag{B.8}$$

$$D_{2,2}^{(j)} = \frac{in(\bar{\alpha}/\omega)}{R} J_n(q_p R) H_n^{(1)}(q_p R_j) \tag{B.9}$$

$$D_{2,3}^{(j)} = -\frac{(\bar{\alpha}/\omega)}{R}\frac{\mathcal{Y}\mathcal{H}_1(n, q_{sh} R)}{H_n^{(1)}(q_{sh} R_{j-1})} \tag{B.10}$$

$$D_{2,4}^{(j)} = -\frac{(\bar{\alpha}/\omega)}{R}\mathcal{Y}\mathcal{J}_1(n, q_{sh} R) H_n^{(1)}(q_{sh} R_j) \tag{B.11}$$

$$D_{2,5}^{(j)} = \frac{-nk(\bar{\alpha}/\omega)(\bar{\beta}/\omega)}{R}\frac{H_n^{(1)}(q_{sv} R)}{H_n^{(1)}(q_{sv} R_{j-1})} \tag{B.12}$$

$$D_{2,6}^{(j)} = \frac{-nk(\bar{\alpha}/\omega)(\bar{\beta}/\omega)}{R} J_n(q_{sv} R) H_n^{(1)}(q_{sv} R_j) \tag{B.13}$$

$$D_{3,1}^{(j)} = ik(\bar{\alpha}/\omega)\frac{H_n^{(1)}(q_pR)}{H_n^{(1)}(q_pR_{j-1})} \tag{B.14}$$

$$D_{3,2}^{(j)} = ik(\bar{\alpha}/\omega)J_n(q_pR)H_n^{(1)}(q_pR_j) \tag{B.15}$$

$$D_{3,3}^{(j)} = 0 \tag{B.16}$$

$$D_{3,4}^{(j)} = 0 \tag{B.17}$$

$$D_{3,5}^{(j)} = (\bar{\alpha}/\omega)(\bar{\beta}/\omega)q_{sv}^2\frac{H_n^{(1)}(q_{sv}R)}{H_n^{(1)}(q_{sv}R_{j-1})} \tag{B.18}$$

$$D_{3,6}^{(j)} = (\bar{\alpha}/\omega)(\bar{\beta}/\omega)q_{sv}^2 J_n(q_{sv}R)H_n^{(1)}(q_{sv}R_j) \tag{B.19}$$

For the strains, $\{e_{rr}, e_{\theta\theta}, e_{zz}, e_{\theta z}, e_{rz}, e_{r\theta}\}$ in medium j at radius R, we have

$$\begin{bmatrix} e_{rr} \\ e_{\theta\theta} \\ e_{zz} \\ e_{\theta z} \\ e_{rz} \\ e_{r\theta} \end{bmatrix} = \left[\mathbf{E}^{(j)}(R)\right] \cdot \begin{bmatrix} A^{(j)} \\ B^{(j)} \\ C^{(j)} \\ D^{(j)} \\ E^{(j)} \\ F^{(j)} \end{bmatrix} \tag{B.20}$$

where

$$E_{1,1}^{(j)} = \frac{(\bar{\alpha}/\omega)}{R^2}\frac{\mathcal{Y}\mathcal{H}_2(n, q_pR)}{H_n^{(1)}(q_pR_{j-1})} \tag{B.21}$$

$$E_{1,2}^{(j)} = \frac{(\bar{\alpha}/\omega)}{R^2}\mathcal{Y}\mathcal{J}_2(n, q_pR)H_n^{(1)}(q_pR_j) \tag{B.22}$$

$$E_{1,3}^{(j)} = \frac{in(\bar{\alpha}/\omega)}{R^2}\frac{\mathcal{Y}\mathcal{H}_3(n, q_{sh}R)}{H_n^{(1)}(q_{sh}R_{j-1})} \tag{B.23}$$

$$E_{1,4}^{(j)} = \frac{in(\bar{\alpha}/\omega)}{R^2}\mathcal{Y}\mathcal{J}_3(n, q_{sh}R)H_n^{(1)}(q_{sh}R_j) \tag{B.24}$$

$$E_{1,5}^{(j)} = \frac{ik(\bar{\alpha}/\omega)(\bar{\beta}/\omega)}{R^2}\frac{\mathcal{Y}\mathcal{H}_2(n, q_{sv}R)}{H_n^{(1)}(q_{sv}R_{j-1})} \tag{B.25}$$

$$E_{1,6}^{(j)} = \frac{ik(\bar{\alpha}/\omega)(\bar{\beta}/\omega)}{R^2}\mathcal{Y}\mathcal{J}_2(n, q_{sv}R)H_n^{(1)}(q_{sv}R_j) \tag{B.26}$$

$$E^{(j)}_{2,1} = \frac{(\bar{\alpha}/\omega)}{R^2}\frac{\mathcal{Y}\mathcal{H}_1(n,q_pR) - n^2 H_n^{(1)}(q_{sv}R)}{H_n^{(1)}(q_pR_{j-1})} \tag{B.27}$$

$$E^{(j)}_{2,2} = \frac{(\bar{\alpha}/\omega)}{R^2}\left(\mathcal{Y}\mathcal{J}_1(n,q_pR) - n^2 J_n(q_{sv}R)\right) H_n^{(1)}(q_pR_j) \tag{B.28}$$

$$E^{(j)}_{2,3} = \frac{-in(\bar{\alpha}/\omega)}{R^2}\frac{\mathcal{Y}\mathcal{H}_3(n,q_{sh}R)}{H_n^{(1)}(q_{sh}R_{j-1})} \tag{B.29}$$

$$E^{(j)}_{2,4} = \frac{-in(\bar{\alpha}/\omega)}{R^2}\mathcal{Y}\mathcal{J}_3(n,q_{sh}R)H_n^{(1)}(q_{sh}R_j) \tag{B.30}$$

$$E^{(j)}_{2,5} = \frac{ik(\bar{\alpha}/\omega)(\bar{\beta}/\omega)}{R^2}\frac{\mathcal{Y}\mathcal{H}_1(n,q_{sv}R) - n^2 H_n^{(1)}(q_{sv}R)}{H_n^{(1)}(q_{sv}R_{j-1})} \tag{B.31}$$

$$E^{(j)}_{2,6} = \frac{ik(\bar{\alpha}/\omega)(\bar{\beta}/\omega)}{R^2}\left(\mathcal{Y}\mathcal{J}_1(n,q_{sv}R) - n^2 J_n(q_{sv}R)\right) H_n^{(1)}(q_{sv}R_j) \tag{B.32}$$

$$E^{(j)}_{3,1} = -k^2(\bar{\alpha}/\omega)\frac{H_n^{(1)}(q_pR)}{H_n^{(1)}(q_pR_{j-1})} \tag{B.33}$$

$$E^{(j)}_{3,2} = -k^2(\bar{\alpha}/\omega)J_n(q_pR)H_n^{(1)}(q_pR_j) \tag{B.34}$$

$$E^{(j)}_{3,3} = 0 \tag{B.35}$$

$$E^{(j)}_{3,4} = 0 \tag{B.36}$$

$$E^{(j)}_{3,5} = ikq_{sv}^2(\bar{\alpha}/\omega)(\bar{\beta}/\omega)\frac{H_n^{(1)}(q_{sv}R)}{H_n^{(1)}(q_{sv}R_{j-1})} \tag{B.37}$$

$$E^{(j)}_{3,6} = ikq_{sv}^2(\bar{\alpha}/\omega)(\bar{\beta}/\omega)J_n(q_{sv}R)H_n^{(1)}(q_{sv}R_j) \tag{B.38}$$

$$E^{(j)}_{4,1} = -2nk\frac{(\bar{\alpha}/\omega)}{R}\frac{H_n^{(1)}(q_pR)}{H_n^{(1)}(q_pR_{j-1})} \tag{B.39}$$

$$E^{(j)}_{4,2} = -2nk\frac{(\bar{\alpha}/\omega)}{R}J_n(q_pR)H_n^{(1)}(q_pR_j) \tag{B.40}$$

$$E^{(j)}_{4,3} = \frac{-ik(\bar{\alpha}/\omega)}{R}\frac{\mathcal{Y}\mathcal{H}_1(n,q_{sh}R)}{H_n^{(1)}(q_{sh}R_{j-1})} \tag{B.41}$$

$$E^{(j)}_{4,4} = \frac{-ik(\bar{\alpha}/\omega)}{R}\mathcal{Y}\mathcal{J}_1(n,q_{sh}R)H_n^{(1)}(q_{sh}R_j) \tag{B.42}$$

$$E^{(j)}_{4,5} = \frac{in(q_{sv}^2 - k^2)(\bar{\alpha}/\omega)(\bar{\beta}/\omega)}{R}\frac{H_n^{(1)}(q_{sv}R)}{H_n^{(1)}(q_{sv}R_{j-1})} \tag{B.43}$$

$$E^{(j)}_{4,6} = \frac{in(q_{sv}^2 - k^2)(\bar{\alpha}/\omega)(\bar{\beta}/\omega)}{R}J_n(q_{sv}R)H_n^{(1)}(q_{sv}R_j) \tag{B.44}$$

$$E_{5,1}^{(j)} = 2ik\frac{(\bar{\alpha}/\omega)}{R}\frac{\mathcal{YH}_1(n, q_pR)}{H_n^{(1)}(q_pR_{j-1})} \tag{B.45}$$

$$E_{5,2}^{(j)} = 2ik\frac{(\bar{\alpha}/\omega)}{R}\mathcal{YJ}_1(n, q_pR)H_n^{(1)}(q_pR_j) \tag{B.46}$$

$$E_{5,3}^{(j)} = \frac{-nk(\bar{\alpha}/\omega)}{R}\frac{H_n^{(1)}(q_{sh}R)}{H_n^{(1)}(q_{sh}R_{j-1})} \tag{B.47}$$

$$E_{5,4}^{(j)} = \frac{-nk(\bar{\alpha}/\omega)}{R}J_n(q_{sh}R)H_n^{(1)}(q_{sh}R_j) \tag{B.48}$$

$$E_{5,5}^{(j)} = \frac{(q_{sv}^2 - k^2)(\bar{\alpha}/\omega)(\bar{\beta}/\omega)}{R}\frac{\mathcal{YH}_1(n, q_{sv}R)}{H_n^{(1)}(q_{sv}R_{j-1})} \tag{B.49}$$

$$E_{5,6}^{(j)} = \frac{(q_{sv}^2 - k^2)(\bar{\alpha}/\omega)(\bar{\beta}/\omega)}{R}\mathcal{YJ}_1(n, q_{sv}R)H_n^{(1)}(q_{sv}R_j) \tag{B.50}$$

$$E_{6,1}^{(j)} = \frac{2in(\bar{\alpha}/\omega)}{R^2}\frac{\mathcal{YH}_3(n, q_pR)}{H_n^{(1)}(q_pR_{j-1})} \tag{B.51}$$

$$E_{6,2}^{(j)} = \frac{2in(\bar{\alpha}/\omega)}{R^2}\mathcal{YJ}_3(n, q_pR)H_n^{(1)}(q_pR_j) \tag{B.52}$$

$$E_{6,3}^{(j)} = \frac{-2(\bar{\alpha}/\omega)}{R^2}\frac{\mathcal{YH}_4(n, q_{sh}R)}{H_n^{(1)}(q_{sh}R_{j-1})} \tag{B.53}$$

$$E_{6,4}^{(j)} = \frac{-2(\bar{\alpha}/\omega)}{R^2}\mathcal{YJ}_4(n, q_{sh}R)H_n^{(1)}(q_{sh}R_j) \tag{B.54}$$

$$E_{6,5}^{(j)} = \frac{-2nk(\bar{\alpha}/\omega)(\bar{\beta}/\omega)}{R^2}\frac{\mathcal{YH}_3(n, q_{sv}R)}{H_n^{(1)}(q_{sv}R_{j-1})} \tag{B.55}$$

$$E_{6,6}^{(j)} = \frac{-2nk(\bar{\alpha}/\omega)(\bar{\beta}/\omega)}{R^2}\mathcal{YJ}_3(n, q_{sv}R)H_n^{(1)}(q_{sv}R_j) \tag{B.56}$$

where

$$\mathcal{YF}_1(x) = nF_n(x) - xF_{n+1}(x) \tag{B.57}$$

$$\mathcal{YF}_2(x) = \left[n(n-1) - x^2\right]F_n(x) + xF_{n+1}(x) \tag{B.58}$$

$$\mathcal{YF}_3(x) = (n-1)F_n(x) - xF_{n+1}(x) \tag{B.59}$$

$$\mathcal{YF}_4(x) = \left[n(n-1) - \frac{x^2}{2}\right]H_n^{(1)}(x) + xF_{n+1}(x) \tag{B.60}$$

where $F_n(x) = \left\{H_n^{(1)}(x), J_n(x)\right\}$.

The stresses are given by

$$\mathbf{S} = \mathbf{C}.\mathbf{E} \tag{B.61}$$

where **C** is the elastic compliance matrix given in 4.4 and **E** are the strain matrix as defined above.

Lastly we define the matrix which generates the boundary conditions as the following

$$\mathbf{T}^{(j)}(R) \;=\; \begin{bmatrix} [\mathbf{D}] \\ [\mathbf{S}_{\{1,5,6\},\{:\}}] \end{bmatrix} \tag{B.62}$$

where **D** is the displacement matix and $\mathbf{s}_{\{1,5,6\},\{:\}}$ is the 1st, 5th and 6th rows of the stress matrix in B.61. This formulation gives the Displacement, u, v, w and stresses σ_{rr}, σ_{rz} and $\sigma_{r\theta}$ used in the boundary condition equations in 4.27.
The final step is to create the global matrix M which relates the layers present in the model to the applied boundary conditions.

$$\mathbf{M} \;=\; \begin{bmatrix} [-\mathbf{T}^{(1)}(R_1)_{\mathcal{I},\{2\}}] & [\mathbf{T}^{(2)}(R_1)_{\mathcal{I},\{1:6\}}] & [0]_{4\times 2} & [0]_{4\times 3} \\ [0]_{4\times 1} & [-\mathbf{T}^{(2)}(R_2)_{\mathcal{I},\{1:6\}}] & [\mathbf{T}^{(3)}(R_2)_{\mathcal{I},\{1:2\}}] & [0]_{4\times 3} \\ [0]_{4\times 1} & [0]_{4\times 6} & [-\mathbf{T}^{(3)}(R_1)_{\mathcal{I},\{1:2\}}] & [\mathbf{T}^{(4)}(R_1)_{\mathcal{I},\{1,3,5\}}] \end{bmatrix} \tag{B.63}$$

where $\mathcal{I} = \{1, 4, 5, 6\}$ corresponding to $u, \sigma_{rr,rz,r\theta}$ for fluid/solid interfaces (all interfaces are fluid/solid interfaces in the LWD model), and where $[0]_{n\times m}$ denotes a $n \times m$ matrix of zeros. This formulation can be immediately extended to any type and number of layers (fluid, solid, vacuum).

Appendix C

Simultaneous Inversion of cross-dipole acoustic waveforms in anisotropic media for azimuthal angle and dispersion of fast and slow shear waves

Cross-dipole acoustic logging tools are designed to measure the anisotropy characteristics in a borehole environment. The dipole sources allow measurements of the shear velocity in slow formations (ie. the formation shear wave velocity is slower than the borehole fluid compressional velocity) that are not possible with monopole tools. Most commonly the tool excites a compressional and shear wave in the formation and the lowest order dipole mode known as the flexural mode. The flexural mode is the motion of the borehole 'flexing' from side to side in the formation, and the guided flexural wave travels along the borehole-formation interface. It is a dispersive mode and asymptotes to the shear velocity at low frequencies and to the fluid velocity at high frequencies, Kurkijian and Chan (1986). In an anisotropic formation, the borehole flexural mode dispersion is sensitive to azimuthal position, and can therefore be used to estimate anisotropy, Sinha et al. (1994).

The cross-dipole sonic tool will see spatial ordering on a scale smaller than the investigating wavelength, as anisotropy. This anisotropy can be intrinsic to the formation as caused by crystal structure, grain orientation, or micro cracks, or it can be extrinsic due to fractures, faults, stress, or bedding planes. The alignment of these phenomena causes a directionally preferential stiffness, which leads to directionally dependent velocities. The polarization of the vertical and horizontal shear waves into their fast and slow components is termed 'shear wave splitting' and can be the result of either form of anisotropy. The degree of splitting can be used to calculate the fracture orientation, Tichelaar and Hatchell (1997), and fracture density, Tatham et al. (1992), in the formation surrounding the borehole. With both the direction of stress and the dispersion information it is possible to calculate 'in-situ' stress fields, Huang (1998) and Sinha and Kostek (1996), which are used to optimize well placement and production and can help predict well stability.

Dispersive waveforms can be misinterpreted as separate arrivals in the time traces which will be seen as two different modes in velocity processing. Kimball (1998) proposed an algorithm to correct dispersive waveforms using modeled dispersion curves. The dispersion relation is a function of borehole geometry, formation and fluid compressional velocities, and the formation and fluid densities. This means that each of these parameters must be known accurately in order to correctly define the frequency dependent shear wave phase velocities. Modeling the dispersion curves, rather than inverting for them, is less computationally expensive but if one of the model parameters is incorrect the derived dispersion curve will be inaccurate. Therefore it more desirable to invert the waveforms for the dispersion relationship as the result does not rely on additional measurements.

The cross-dipole tools try to minimize the dispersive effects of the flexural mode by exciting frequencies close to the low frequency asymptote, ie. in the non-dispersive regime, figure C-1. Unfortunately the energy of the flexural mode can be very low in this region, therefore decreasing the signal to noise ratio, Kimball et al. (1995). Moreover, the non-dispersive region changes, as the tool measures the response of different formations along the borehole, making it difficult to consistently excite energy over the correct frequencies. In other words even though the cross-dipole tool excites frequencies close to the low frequency asymptote there is often substantial dispersion Tang et al. (1995).

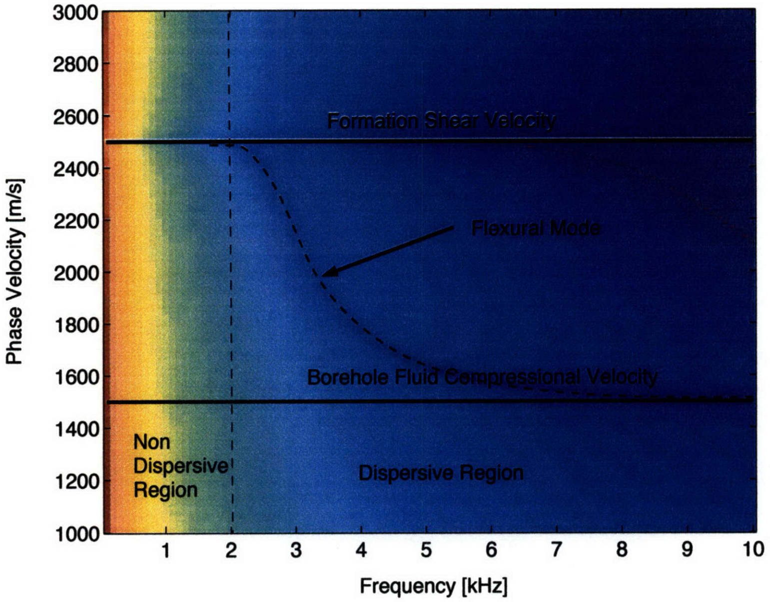

Figure C-1: Modeled Example of a Flexural Mode dispersion Curve. Borehole Diameter [13"], Borehole Fluid Shear Velocity [1500 ms^{-1}], Borehole Fluid Density [1200 kgm^{-3}], Formation Shear Velocity [2500 ms^{-1}], Formation Compressional Velocity [5000 ms^{-1}], Formation Density [2600 kgm^{-3}]

In this paper we present a method to simultaneously invert cross-dipole data for azimuthal orientation of anisotropy and for the dispersion curves of the fast and slow shear waves. Current processing performs each of these steps separately: firstly the azimuthal angle is estimated and secondly the fast and slow wave components are processed individually to obtain the formation shear wave velocities. The former is estimated by rotating the orthogonal dipole measurements until the cross components are minimized. This occurs when the measurements are aligned along the fast and slow shear directions and the angle defines the orientation of the fast and slow directions with respect to the tool. If the mode is non-dispersive, Alford rotation (Alford (1986)) can be used to project the waveforms onto the fast and slow shear mode directions. This simple rotation scheme assumes no frequency dependent velocities and finds the azimuthal angle for which the cross-dipole components are minimized. However, Huang et al. (1998) showed that any rotation scheme that does not consider waveform dispersion may produce erroneous results. Hence it is important that simultaneous inversion be done for azimuthal orientation and dispersion. The feasibility of combining the two-step process into a one-step inversion is shown by Tang and Chunduru (1999), where data are inverted for an average low frequency shear wave velocity and the azimuthal angle. In this paper we present a similar methodology but invert for the full dispersion curve allowing a better characterization of anisotropy.

C.1 The Objective function and Inversion Method

C.1.1 Cross-Dipole Data

The cross-dipole tool belongs to the family of wireline acoustic tools. It is used primarily to estimate acoustic velocities as a function of azimuthal position in slow formations, (i.e. those whose shear velocity is less than the borehole fluid velocity). Although tool design varies from company to company, all tools have similar general features and consist of two pairs of dipole sources and eight pairs of dipole receivers. The dipole acoustic transducer source pairs are oriented orthogonally on the tool, one pair along the x direction and one along the y direction. The transducer receivers are similarly oriented with the first pair having a large offset from the source and subsequent receivers being evenly distributed with a separation of approximately 15 cm. (Figure C-2 shows a cartoon of a generic cross-dipole tool). This source receiver configuration permits a directional measurement of the formation's acoustic response. The two sources fire separately, and after each excitation the receivers in both the x and y direction record the formation response. This recording results in 4 arrays of 8 (the number of receivers) traces, X source to X receiver referred to as XX, X source to Y receiver referred to XY, and similarly for YX and YY.

When a slow formation is excited with a dipole source, a set of axisymmetric

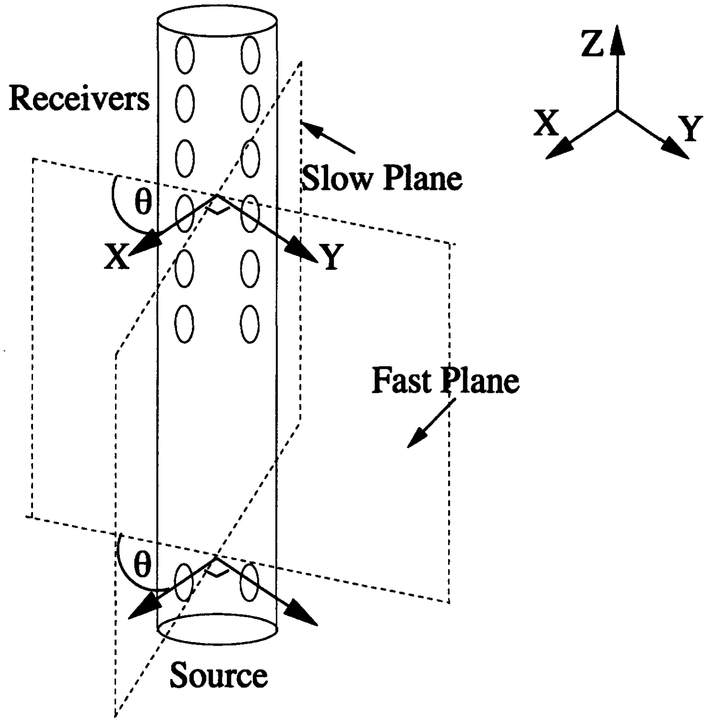

Figure C-2: Schematic of generic Cross-Dipole tool.

borehole-guided modes and compressional waves are formed. In a fast formation there is also a refracted shear wave. The guided modes of lowest cut-off frequency, known as flexural modes, are polarized in the x-y plane perpendicular to their direction of propagation that is along the z-axis. If the medium is anisotropic, the flexural wave motion splits into a fast and slow component dependent on the directional velocities of the rock and the frequency component of the excitation. When the source transducer pair oriented along the x-axis is excited, the displacement vector of the flexural wave generated is also in the x direction. The fast and slow axes of the formation make an angle θ with respect to the x and y axes so that the displacement vector has projections $\cos\theta$ and $\sin\theta$ on the fast and slow directions, respectively. The fast and slow flexural waves then propagate with their respective (frequency dependent) velocities and are recorded at the receivers. Since the receivers are also oriented along the x and y axes, the displacement measured is a second projection of the fast and slow modes back onto the x and y axes.

Let $S_x(t)$ and $S_y(t)$ represent the source excitation functions for the x and y oriented dipoles, and let $s_x(\omega)$ and $s_y(\omega)$ be their fourier transforms. Also let $g_f^{(n)}(\omega)$ and $g_s^{(n)}(\omega)$ be the formation propagation function from the source to the n^{th} receiver, i.e.,

$$\begin{aligned} g_f^{(n)}(\omega) &= \exp\left(i\frac{\omega}{v_f(\omega)}z_n\right) && \text{(C.1)} \\ g_s^{(n)}(\omega) &= \exp\left(i\frac{\omega}{v_s(\omega)}z_n\right) && \text{(C.2)} \end{aligned}$$

where $v_f(\omega)$ and $v_s(\omega)$ are the fast and slow frequency dependent phase velocities, respectively, and z_n is the distance from the source to the nth receiver. The signals recorded by the cross dipole tool are therefore given by

$$\begin{aligned} xx_n(\omega) &= g_f^{(n)}(\omega)s_x(\omega)\cos^2\theta + g_s^{(n)}(\omega)s_x(\omega)\sin^2\theta && \text{(C.3)} \\ xy_n(\omega) &= [g_f^{(n)}(\omega)s_x(\omega) - g_s^{(n)}(\omega)s_x(\omega)]\cos\theta\sin\theta && \text{(C.4)} \\ yx_n(\omega) &= [g_f^{(n)}(\omega)s_y(\omega) - g_s^{(n)}(\omega)s_y(\omega)]\cos\theta\sin\theta && \text{(C.5)} \\ yy_n(\omega) &= g_f^{(n)}(\omega)s_y(\omega)\sin^2\theta + g_s^{(n)}(\omega)s_y(\omega)\cos^2\theta && \text{(C.6)} \end{aligned}$$

Assuming the same source function for both the x and y transducers, $s_x(\omega) = s_y(\omega) = s(\omega)$, and letting $f_n(\omega) = g_f^{(n)}s(\omega)$ and $s_n(\omega) = g_s^{(n)}s(\omega)$, we can now represent equations C.3 to C.6 in matrix form

$$\begin{pmatrix} xx_n(\omega) & xy_n(\omega) \\ yx_n(\omega) & yy_n(\omega) \end{pmatrix} = \begin{pmatrix} \cos\theta & -\sin\theta \\ \sin\theta & \cos\theta \end{pmatrix} \begin{pmatrix} f_n(\omega) & 0 \\ 0 & s_n(\omega) \end{pmatrix} \times \begin{pmatrix} \cos\theta & \sin\theta \\ -\sin\theta & \cos\theta \end{pmatrix} \qquad \text{(C.7)}$$

C.1.2 Rotation

We can use equation C.7 to create synthetic waveforms for a given source function and dispersion relations. Figures C-3 and C-4 show the difference between the borehole flexural mode recorded with a tool whose x and y axes are at an angle $\theta = 25^o$ with the formation fast and slow axes, and the borehole flexural mode recorded with a tool which is aligned with the formation fast and slow axes. In matrix terms, if the tools and formation axes are aligned, the diagonal components of equation C.7 are maximized and the off diagonal components vanish.

We can invert C.7

$$\begin{pmatrix} f_n(\omega) & 0 \\ 0 & s_n(\omega) \end{pmatrix} = \begin{pmatrix} \cos\theta & \sin\theta \\ -\sin\theta & \cos\theta \end{pmatrix} \begin{pmatrix} xx_n(\omega) & xy_n(\omega) \\ yx_n(\omega) & yy_n(\omega) \end{pmatrix} \times \begin{pmatrix} \cos\theta & -\sin\theta \\ \sin\theta & \cos\theta \end{pmatrix}, \tag{C.8}$$

which gives the fast and slow propagation functions as

$$f_n(\omega) = xx_n(\omega)\cos^2\theta + [xy_n(\omega) + yx_n(\omega)]\sin\theta\cos\theta + yy_n(\omega)\sin^2\theta \tag{C.9}$$

$$s_n(\omega) = xx_n(\omega)\sin^2\theta - [xy_n(\omega) + yx_n(\omega)]\sin\theta\cos\theta + yy_n(\omega)\cos^2\theta. \tag{C.10}$$

Additionally, it is easy to see from equations C.9 and C.10 that if $\theta = 90^o$ or 0^o there will be no $xy_n(\omega)$ or $yx_n(\omega)$ dependence.

C.1.3 Propagation

Next, the effects of propagation through the formation are undone. Figure C-5 shows the same data from figure C-4 after the effects of propagation have been undone. If the correct dispersion relation is used (i.e., each frequency component is back propagated at the correct velocity), only the source function remains at each receiver on the inline arrays, and because the correct rotation has been applied, there is no signal on the cross-line arrays.

Remembering that $f_n(\omega) = g_f^{(n)} s(\omega)$ and $s_n(\omega) = g_s^{(n)} s(\omega)$, we can write equation C.8 as,

$$\begin{pmatrix} s(\omega) & 0 \\ 0 & s(\omega) \end{pmatrix} = \begin{pmatrix} e^{-i\frac{\omega}{v_f(\omega)}z_n} & 0 \\ 0 & e^{-i\frac{\omega}{v_s(\omega)}z_n} \end{pmatrix} \times$$
$$\begin{pmatrix} \cos\theta & \sin\theta \\ -\sin\theta & \cos\theta \end{pmatrix} \begin{pmatrix} xx_n(\omega) & xy_n(\omega) \\ yx_n(\omega) & yy_n(\omega) \end{pmatrix} \begin{pmatrix} \cos\theta & -\sin\theta \\ \sin\theta & \cos\theta \end{pmatrix}. \quad \text{(C.11)}$$

which is valid for any receiver n.

The propagation function has been moved to the right hand side. There is now a complete expression for the rotation and propagation of a source function to each of the array receivers. In other words, if the correct azimuthal angle and dispersion relations, $v_f(\omega)$ and $v_s(\omega)$, are used in equation C.11, we recover the source function $s(\omega)$ at every receiver.

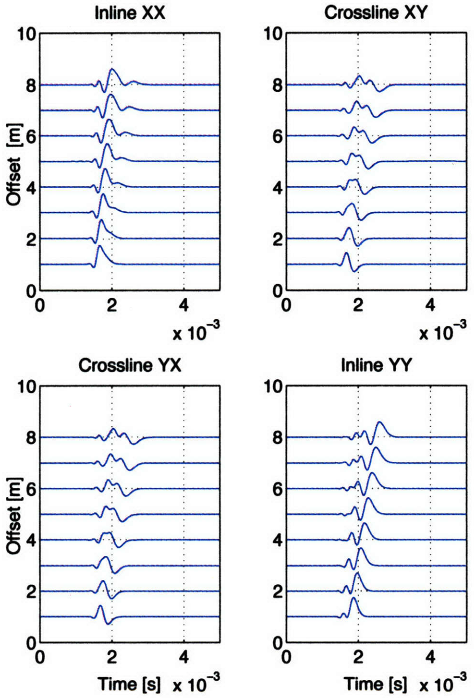

Figure C-3: Time series representation of the borehole flexural mode with tool at angle $\theta = 25^o$ with the formation axes.

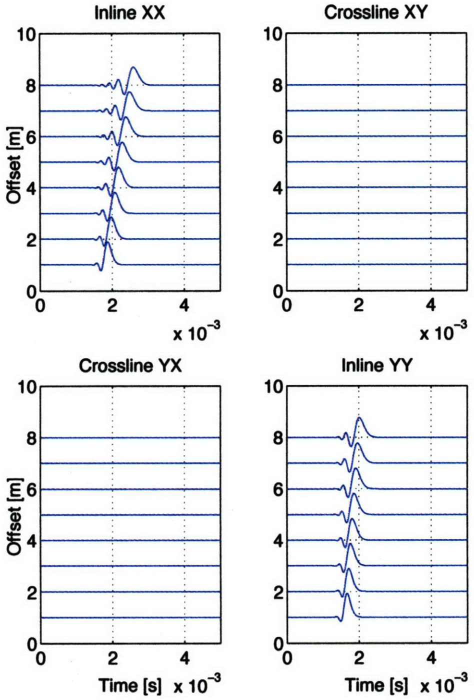

Figure C-4: Time series representation of the borehole flexural mode with tool aligned ($\theta = 90^o, 0^o$) with the formation axes.

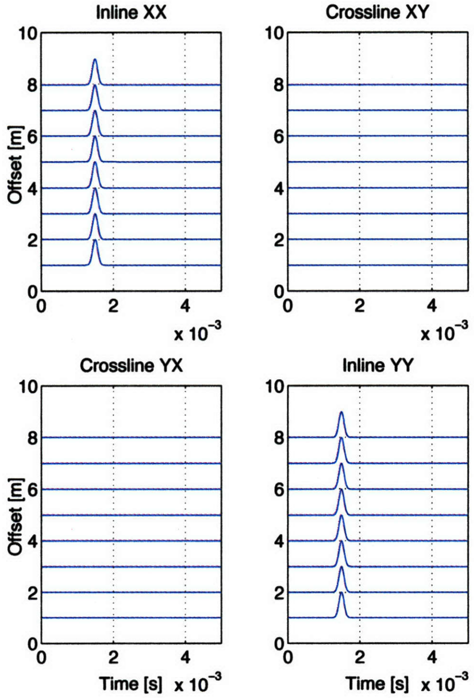

Figure C-5: Time series representation of flexural mode after back propagation with the correct dispersion relation.

C.2 Objective Function

To set up this problem as an inversion, it is necessary to form an objective function whose minimum corresponds to the correct values of the parameters being inverted for. (ie $v_f(\omega)$, $v_s(\omega)$ and θ). If the two inversions for azimuth and phase velocities are performed separately, the second inversion result is conditional on the first. This conditionality means that any error in the first result will be carried into the second. Performing a joint inversion gives the global best estimate for all of the parameters simultaneously and provides an unconditional result.

We know that for the correct azimuth, θ, the back rotated signals $f_n(\omega)$ and $s_n(\omega)$ will be maximized. We can therefore find the derivative of equations C.9 and C.10 and set them to zero (or minimize, in the case of an inversion) to obtain the azimuthal angle,

$$\frac{\partial f(\omega)}{\partial\theta} = (yy - xx)\sin 2\theta + (xy + yx)\cos 2\theta = 0 \tag{C.12}$$

$$\frac{\partial s(\omega)}{\partial\theta} = (xx - yy)\sin 2\theta - (xy + yx)\cos 2\theta = 0 \tag{C.13}$$

For the correct azimuth both $\frac{\partial f}{\partial\theta}(\omega)$ and $\frac{\partial s}{\partial\theta}(\omega)$ would ideally be zero independently, therefore their difference $\frac{\partial f}{\partial\theta}(\omega) - \frac{\partial s}{\partial\theta}(\omega)$ also vanishes. In order to have an objective function that is also sensitive to correlations in the data (i.e. between receivers), we chose to minimize the quantity $\int d\omega \left|\frac{\partial f_n}{\partial\theta}(\omega) - \frac{\partial f_m}{\partial\theta}(\omega)\right|^2 + \left|\frac{\partial s_n}{\partial\theta}(\omega) - \frac{\partial s_m}{\partial\theta}(\omega)\right|^2$, where n and m are the receiver indices (in this case 1 to 8). Note also that when the signal is incorrectly back-rotated, the f_n and s_n data both contain fast and slow components which are correlated and correctly picked-up by such an objective function.

For the propagation, we know that if the correct velocity is used at each frequency, the data at each receiver will be back propagated to the source function. Thus if we undo the propagation correctly and subtract the signal from any receiver pair the absolute value of their difference should vanish.

Therefore, our choice for an objective function is

$$\begin{aligned} O[v_f(\omega), v_s(\omega), \theta] &= \int_\omega \sum_{n,m} \left| \frac{\partial f_n(\omega)}{\partial \theta} - \frac{\partial f_m(\omega)}{\partial \theta} \right|^2 \\ &+ \left| \frac{\partial s_n(\omega)}{\partial \theta} - \frac{\partial s_m(\omega)}{\partial \theta} \right|^2 \\ &+ |f_n(\omega) - f_m(\omega)|^2 + |s_n(\omega) - s_m(\omega)|^2 \end{aligned} \tag{C.14}$$

which is sensitive to both azimuth angle and fast and slow dispersion. In addition, this objective function combines all the data from all receivers, and its minimization should therefore enable one to obtain the best fitting parameters (azimuth as well as fast and slow mode dispersion curves) taking into account the maximum amount of information contained in the data. This method is to be contrasted with more traditional methods (for example, first estimate the azimuth independently of dispersion and then separately analyze the fast and slow mode data), that only partially take into account all the information contained in the data. Equation C.15 is another representation of C.14. It shows, in matrix form, how the inversion calculates the value of the objective function for the fast dispersion using trial functions v_{f-t} and θ_{trial} for receivers spaced a distance z_n and z_m from the source. A similar matrix can be written for the slow dispersion.

$$\begin{pmatrix} a & b \\ c & d \end{pmatrix} \tag{C.15}$$

where,

$$a = \frac{1}{2} e^{-\frac{i z_n \omega}{v_{f-t}(\omega)}} \left[e^{\frac{i z_n \omega}{v_f(\omega)}} + e^{\frac{i z_m \omega}{v_f(\omega)}} + \left(e^{\frac{i z_n \omega}{v_f(\omega)}} - e^{\frac{i z_m \omega}{v_f(\omega)}} \right) \cos 2(\theta - \theta_t) \right]$$

$$b = \frac{1}{2} e^{-\frac{i z_m \omega}{v_{f-t}(\omega)}} \left[e^{\frac{i z_n \omega}{v_f(\omega)}} - e^{\frac{i z_m \omega}{v_s(\omega)}} \right] \sin 2(\theta - \theta_t)$$

$$c = \frac{1}{2} e^{-\frac{i z_n \omega}{v_{f-t}(\omega)}} \left[e^{\frac{i z_n \omega}{v_f(\omega)}} - e^{\frac{i z_m \omega}{v_f(\omega)}} \right] \sin 2(\theta - \theta_t)$$

$$d = \frac{1}{2} e^{-\frac{i z_m \omega}{v_{f-t}(\omega)}} \left[e^{\frac{i z_n \omega}{v_f(\omega)}} + e^{\frac{i z_m \omega}{v_f(\omega)}} + \left(-e^{\frac{i z_n \omega}{v_f(\omega)}} + e^{\frac{i z_m \omega}{v_f(\omega)}} \right) \cos 2(\theta - \theta_t) \right]$$

One can see from inspection of C.15 that if $\theta_t = \theta$, the two off diagonal terms will be zero and the diagonal terms will be maximized. If $v_{f-t} = v_f$, the two diagonal terms will be zero but the off diagonal terms will still have a contribution unless the trial angle is correct. Note that subtracting f_m from f_n and not s_n makes the objective function insensitive to the initial source receiver offset. The full dispersion curve specifies a velocity for each frequency component in the data.

C.3 Inversion

Depending on the size of the fourier transform used to convert the data into the frequency domain, there can be a large number of parameters to invert for. Typically if the traces have 512 samples in time and a 512 point fast fourier transform is performed, there will be 256 frequencies to invert for on each dispersion curve. This leads to an inversion search space of 513 parameters ($2 \times 256(frequencies) + 1(angle)$). In order to avoid inverting such a large model space the dispersion curves can be parameterized by using piecewise constants, for example. Essentially this divides the frequency space into a number of bands over which the dispersion curve is described by a constant. The inversion code implements a variable grid algorithm, which dynamically updates the placement and size of the frequency bands with each iteration. The algorithm has two stages. The first, called the spin-up, uses regularly spaced bins to estimate the rough form of the data's dispersion curve. At each spin-up iteration the code doubles the number of piecewise constants it uses to fit the curve. At the first iteration it fits one constant which represents some average phase velocity; at the next iteration it fits two, and at the next 4, and so on. The spin-up is typically run for 4 iterations, which means that the dispersion curve has been parameterized by 8 evenly spaced (in frequency) constants. These iterations provide the best possible starting guess for the second part of the algorithm which uses a variable grid frequency spacing. After each minimization iteration the grid refining code allocates the number of frequency bins to be used according to the shape of the dispersion curve at those frequencies. In other words, the algorithm adds more frequency bins where the gradient of the curve is largest, ensuring that the inversion has enough parameters to capture the character of the curve while keeping the number to a minimum so that the inversion runs efficiently.

Figure C-7 shows the objective function space for some synthetic flexural wave forms. The data was created using the dispersion relations and source spectrum shown in figure C-6. The plots were made by dividing the frequency axis into 4 regions (shown as the red vertical dotted lines in C-6) and holding three of the phase velocities constant, at the correct value, while varying the fourth. The objective function surface is shown for the low, mid-low, mid-high, and high regimes and the pink star marks the true minimum of the surface. Figure C-8 shows a similar view of the surface as a function of azimuthal angle; here the slow dispersion curve is held at the correct velocity while the angle and fast dispersion relation are varied in the 4 frequency bins. Each of the minima shown in figure C-8 show smoothly varying structure with a single minimum. The absence of complicated structure or local minima shows the objective function is easy to invert. The minima decrease in size for the higher frequency bins but remain smooth and well behaved.

The slant of the minima in figure C-7 is due to a correlation between the fast and slow velocity modes. When inverting the data, the objective function is looking to find the values of v_f and v_s that back propagate the data to the source function. Although only one choice for each of these dispersion curves will give the correct answer, there can be some trade off between the two modes. In other words, if the inversion chooses the fast mode to be a little slower and the slow mode to be a little faster, there is still a good match of the source functions. This trade off is intrinsic to the objective function, however by using all possible receiver pairs the length of the correlation is reduced. If the same figure were shown for just one receiver pair, the correlation would stretch; conversely, if there were more than 8 pairs of receivers, there would be a shrinking of the minimum in the diagonal direction. From the frequency spectrum of the data, shown in figure C-6 (the black curve), and from the total value of the

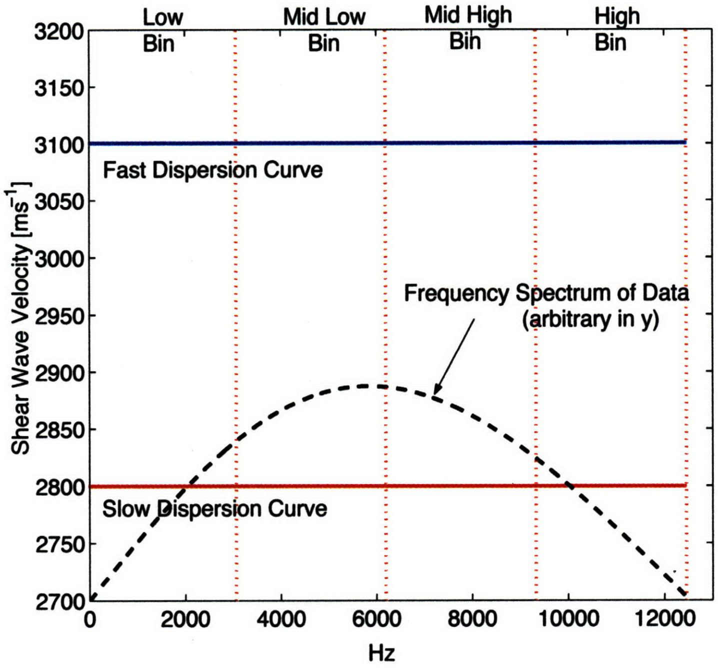

Figure C-6: Dispersion Relations for fast and slow modes and the spectrum of synthetic data used for objective function surfaces.

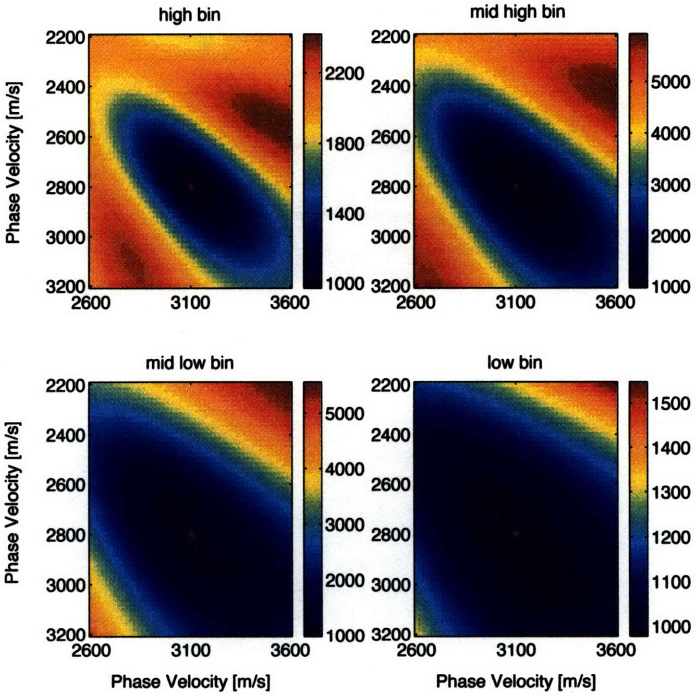

Figure C-7: Objective function surfaces for 4 different frequency bands and the correct rotation angle with zero offset to first receiver.

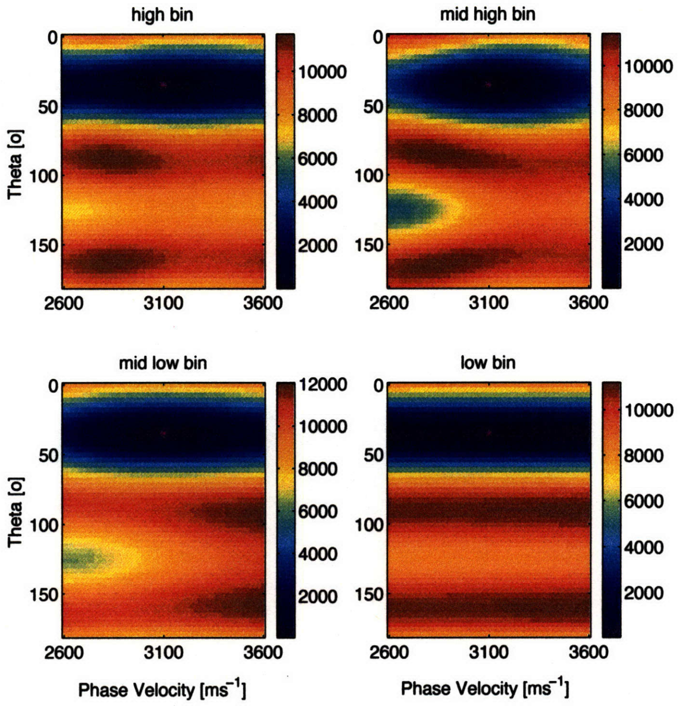

Figure C-8: Objective function surfaces for 4 different frequency bands with one dispersion curve held at the correct values and zero offset to the first receiver.

objective function in each in each bin, seen in the colourbars in figure C-7, it is clear that the frequencies with higher spectral content have a greater influence on the value of the objective function. For the high and low frequency bands, where the spectrum has less magnitude, the contribution to the objective function is less. This fact has important consequences for the inversion as the results are likely to be inaccurate where the spectrum has lower magnitude.

C.4 Results

C.4.1 Results from Synthetic Data

This section presents inversion results for synthetic flexural waveforms and discusses the consequences of noise within the data. Synthetic waveforms, were calculated using a rotation of 35^o and the dispersion relations and source spectrum shown in figure C-9. The phase velocity values were chosen to be similar to those found in a shaley sandstone formation and the source spectrum is typical of those used in industry shear sonic logging tools. Figure C-10 shows the time series array representation of the calculated synthetic data (green). The data are inverted for a total of 6 spin-up iterations and a further 6 iterations using the dynamic frequency grid. The blue curves, again in figure C-10, show the time series after the data have been back propagated and rotated by the output of the inversion code. As previously discussed in sections C.1.2 and C.1.3, if the data have been correctly rotated and back propagated, the cross-line components will be minimized and the in-line components will recover their original form from the time of excitation. In other words they have had the effects of rotation and propagation along the borehole undone and they resemble the excitation source function. This can be seen clearly in figure C-10 where the blue traces have been minimized on the cross-line components and show the source function on the in-line traces. The inversion also correctly calculated the angle between the tools x-axis and the fast plane as 35^o. Thus mismatch between the inversion result and synthetic curves at high frequencies is due to the lack of data above 10 khz. The source spectrum is highest around 4 khz but falls off rapidly and there is almost no frequency content in the data above 9 khz.

Figures C-12 and C-13 show inversion results for the same synthetic data used above but with 5% gaussian white noise added to the time traces which is approximately 30dB. The azimuthal angle is estimated to be 34^o which is 1^o less than the true angle. The inverted dispersion curves are noisy above and below the region of high frequency content. There is however, good agreement where the frequency content is highest.

C.4.2 Results from Field Data

In this section we present some results from real cross-dipole data from a well in Venezuela. We compare three methods; the joint inversion, simple frequency domain Alford rotation followed by Prony's method and, simple frequency domain Alford rotation followed by a back propagation scheme which inverts each frequency individually. The simple frequency domain rotation scheme is similar to that of the joint

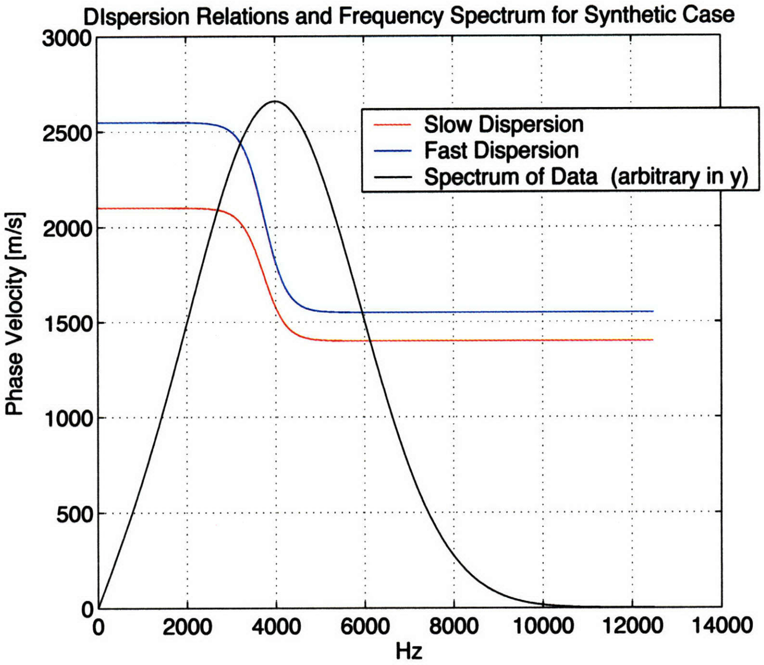

Figure C-9: Dispersion curves for fast and slow shear waves used to create synthetic data. The black curve shows the synthetic data.

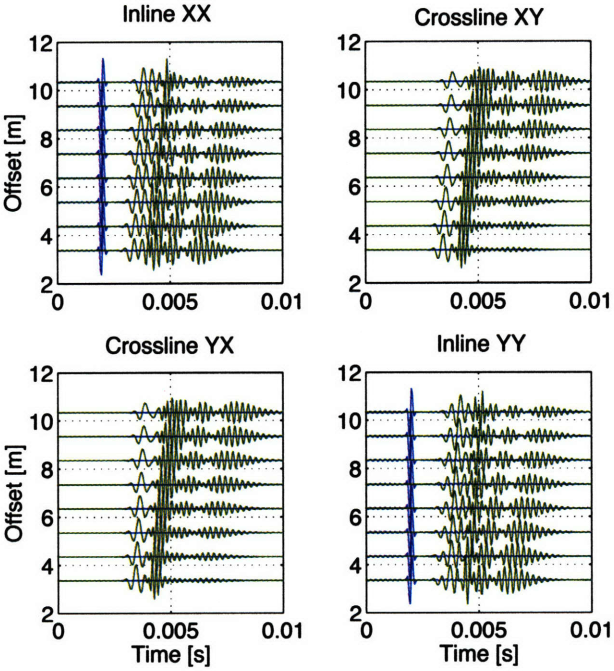

Figure C-10: Time series Representation of original synthetic data (green) and after rotation and back propagation prescribed by inversion output (blue).

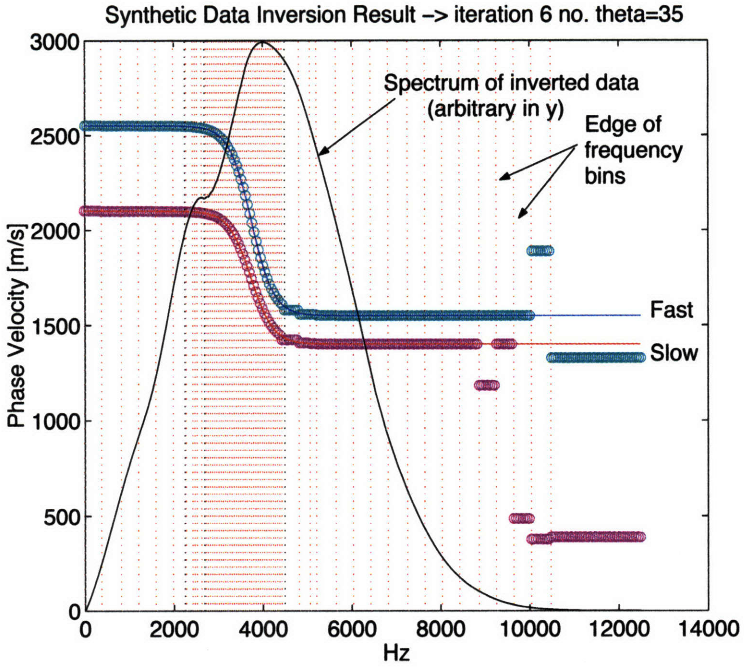

Figure C-11: The inversion results for the synthetic data case. The circles represent the inversion output and the solid curves show the dispersion relationships used to create the synthetic data.

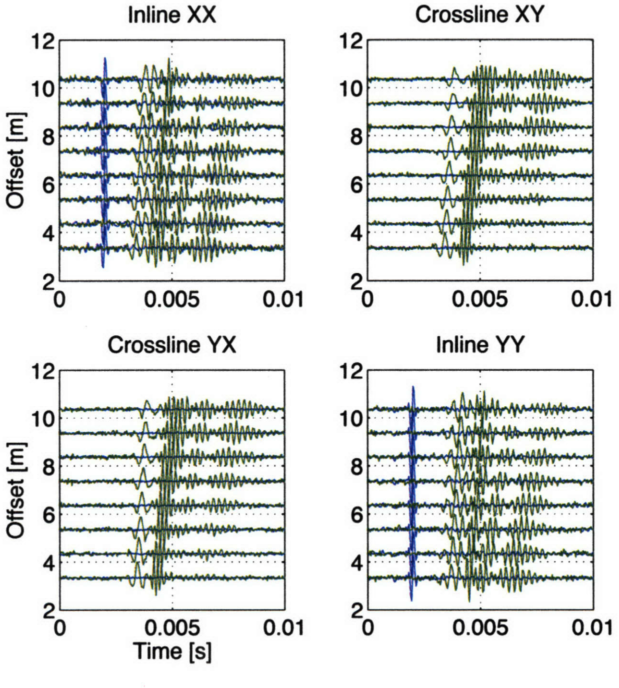

Figure C-12: Time series Representation of original noisy synthetic data (green) and after rotation and back propagation prescribed by inversion output (blue).

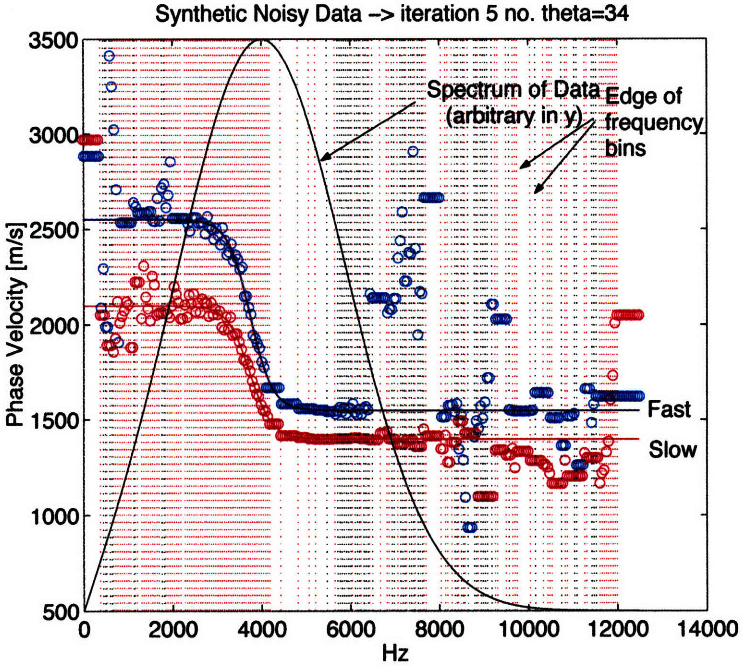

Figure C-13: The inversion results the noisy synthetic data case. The circles represent the inversion output and the solid curves show the dispersion relationships used to create the synthetic data.

inversion but is calculated without taking into account the effects of dispersion. Figures C-16, C-19 C-22 and, C-25 show reasonable agreement between the three results for depths of 7000, 7500, 6700 and, 8000 ft. Below each inversion result is a calculation of semblance from the data after rotation onto the fast and slow axes. (Figures C-17, C-20,C-23 and, C-26. The maximum contour corresponds to the velocity of coherent energy in the waveforms. Figures C-18, C-21, C-24 and C-27 show the original waveforms in green and after they have been rotated and back propagated as prescribed by the inversion (blue). As previously discussed in sections C.1.2 and C.1.3 there should be a minimization for the cross-line components and the waveforms should resemble the source function.

Table C.1 shows the azimuthal angle between the x axis of the tool and the fast formation direction calculated by the joint inversion, and the simple frequency domain Alford rotation. It also shows the difference between these two inversions and the difference in shear mode velocities taken from the dispersion curves of the rotated data. (except for depth 7500ft which was taken from the semblance plots) Anisotropy in rocks is typically less than 10% suggesting the data from depth 7500ft are noisy or the borehole may not be exactly circular.. The tool rotates as it moves through the well so the inversion results must be corrected to find the direction of maximum stress with respect to the geographic north. The tool measures the azimuthal angle from the x-axis on the tool and the magnetic north, table C.2 shows the corrected results. These can be compared with borehole break out measurements in the well which are areas of damage to the borehole caused by stress. As the stress acts on the borehole it can change from circular to elliptical with the major axis in the direction of minimum stress. If the deformation increases past the elastic regime the borehole wall can experience failure and some of the stress will be released in the form of a break out. These break outs are measured by calipers in the well which record the diameter of the borehole in orthogonal directions. Break out data gathered from this particular well indicate a maximum stress direction between 330^o and 360^o. Additional stress information can be taken from the word stress map, www.world-stress-map.org, which compiles regional stress field data for public use. Figure C-15 shows the regional stress enlarged in the region of the borehole. Here the direction of maximum stress is recorded as approximately $315^o \pm 10^o$. Figure C-14 shows the stresses from breakouts and regional stresses with the inverion results for each depth. The azimuthal angles calculated from the inversion fall within the expected direction with the exception of the result at depth 7500 ft. It is unlikely that the stress direction changes significantly over the length of the well because the regional stresses are determined by the plate movements along the northern coast on Venezuela, shown as the thick black line in figure C-15. Instead the inverted angle mismatch is likely to be a result of noise in the data. The dispersion inversions at this depth, figure C-22, show spurious results for the fast phase velocities at low frequencies, indicating the presence of noise.

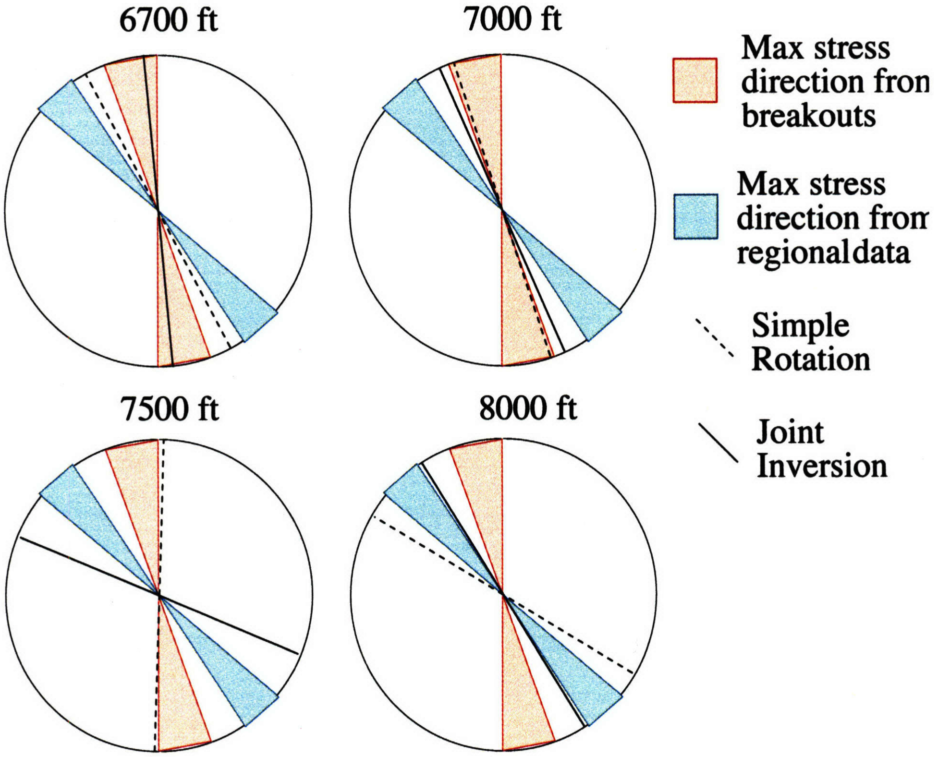

Figure C-14: Stress directions for joint and simple inversions shown with maximum stress directions calculated from break outs and regional stresses.

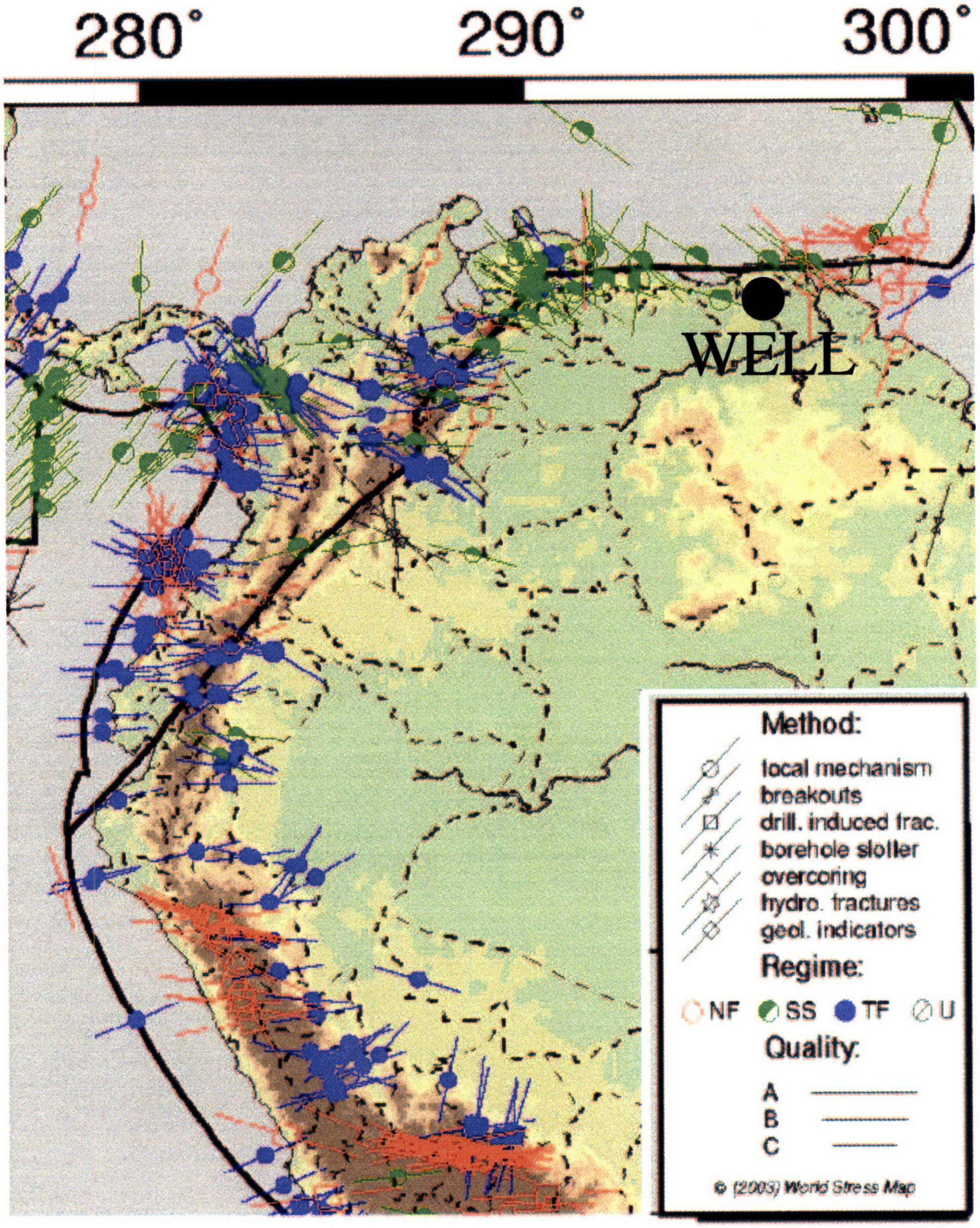

Figure C-15: Regional stress map for area of borehole.

C.5 Conclusions and Further Work

We have presented a method for a joint inversion for azimuthal angle and dispersion relation for cross dipole acoustic waveforms. There is good agreement between the dispersion relations calculated here and those calculated using traditional processing methods but the calculated azimuthal angles differ significantly. These angles have been compared with break out data from the borehole and regional stress maps and show reasonable agreement at three of the four depths. The data quality at depth 7500 ft is likely responsible for the poor maximum stress direction estimation. This noise can be seen in the dispersion curves for that depth in the low frequencies. It should be noted however that the joint inversion gives much better results in the low frequencies than either of the comparative methods. The semblance plots also agree with the joint inversion results underlining the importance of a simultaneous inversion. Further work on this project should address multi-modal arrivals. In this paper we have assumed that the majority of the energy is in the flexural mode, allowing us to ignore the refracted compressional and shear waves. If the borehole is not perfectly cylindrical the flexural mode may not be the strongest arrival and contamination in the flexural mode from other arrivals must be accounted for. This can be achieved by filtering in the time and/or the frequency domain, if the arrivals are well separated, but often this method is not ideal because useful data may be discarded or not separated completely. A second consideration is the speed of the algorithm which may be improved using alternative non-linear inversion methods.

C.6 Acknowledgments

This work was partially supported by the Department of Energy, Grant DE-FC26-02NT15346

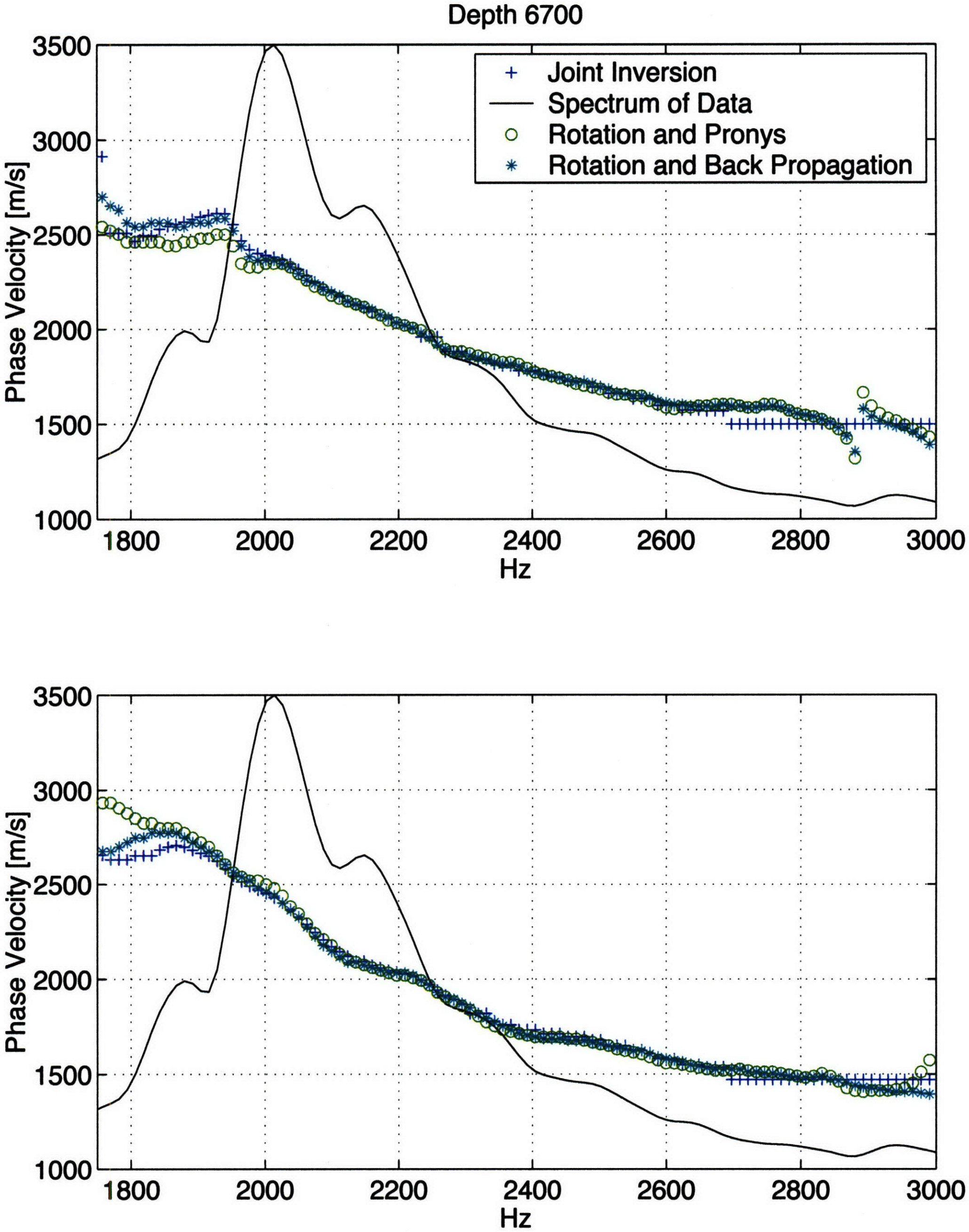

Figure C-16: Dispersion analysis results for depth 6700ft.

Depth ft	Joint Inversion degrees	Simple Inversion degrees	difference degrees	Difference in velocities from fast and slow modes (from dispersion) $[ms^{-1}]$ [%]
6700	50	27	23	250, 9%
7000	50	59	9	300, 9%
7500	47.5	56	8.5	550, 17%
8000	69	43	26	250, 7%

Table C.1: Angle between fast plane and tool x-axis for joint inversion and simple angle inversion

Depth ft	tool angle degrees from true North	Joint Inversion degrees from true North	Simple Inversion degrees from true North
6700	55	355	332
7000	76	335	343
7500	115	293	1
8000	258	327	301

Table C.2: Angle between fast plane and tool x-axis for joint inversion and simple angle inversion

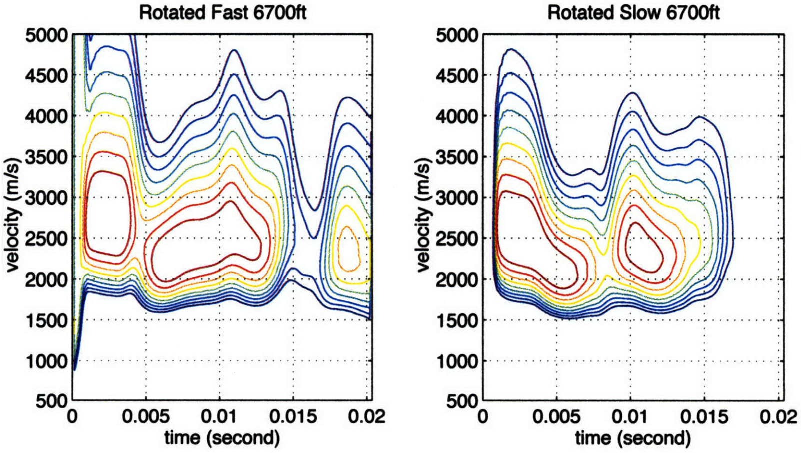

Figure C-17: Semblance analysis results for rotated data at depth 6700ft.

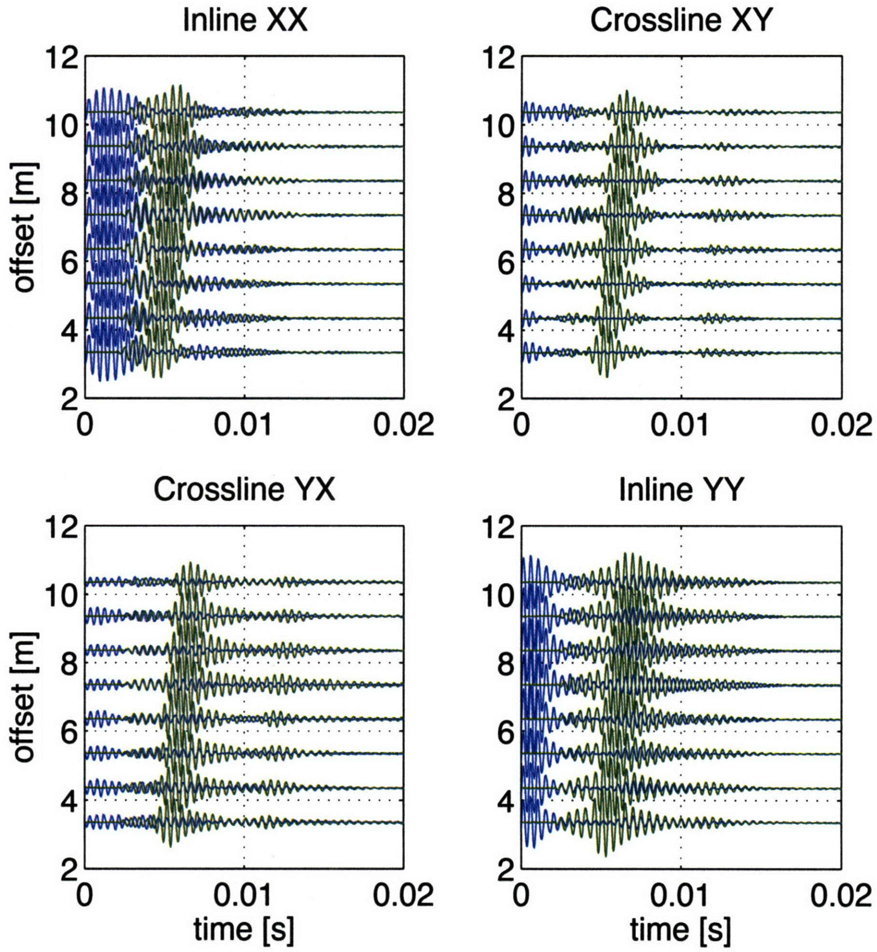

Figure C-18: Original waveforms (green) and after rotation and back propagation as prescribed by inversion results (blue).

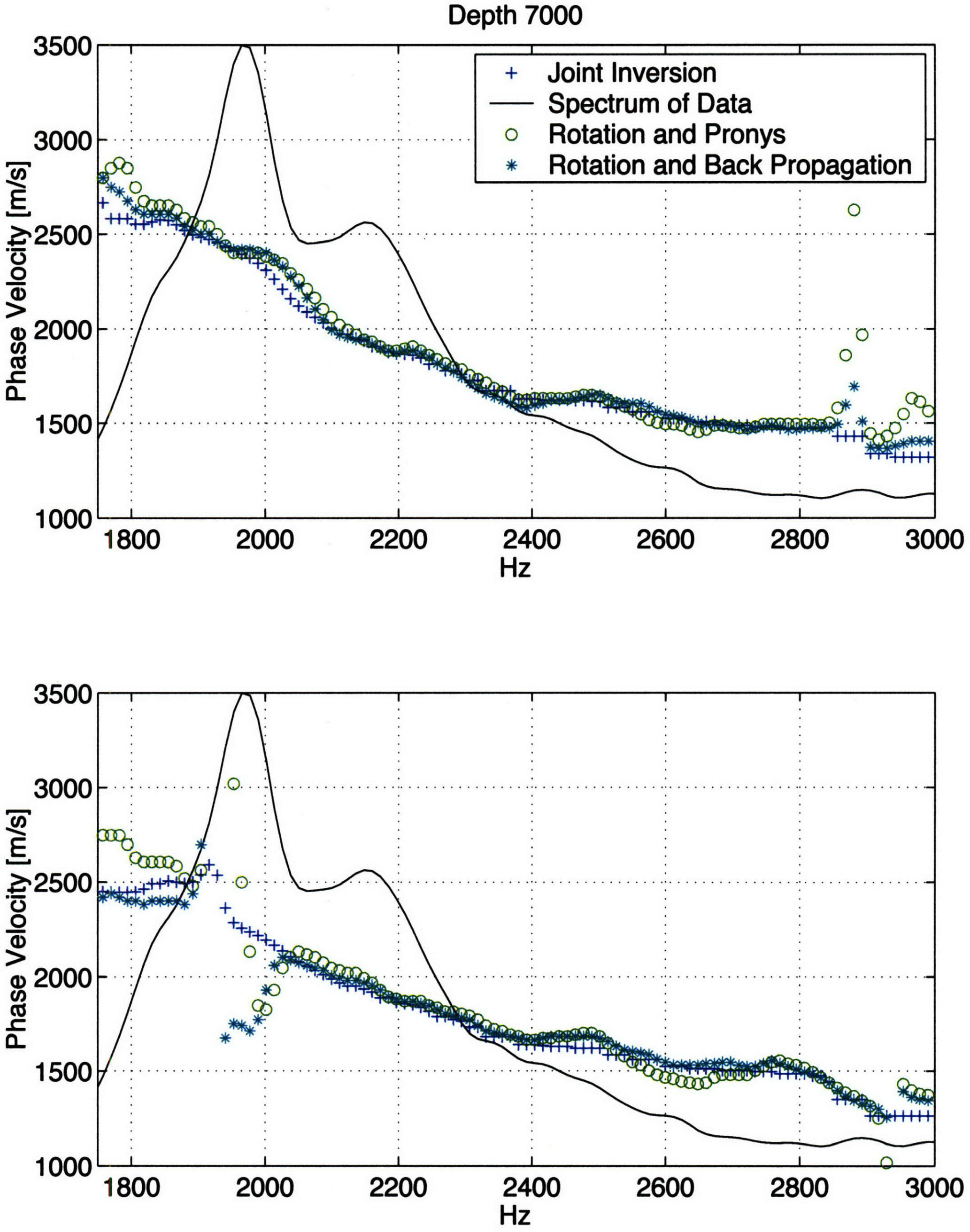

Figure C-19: Dispersion analysis results for depth 7000ft.

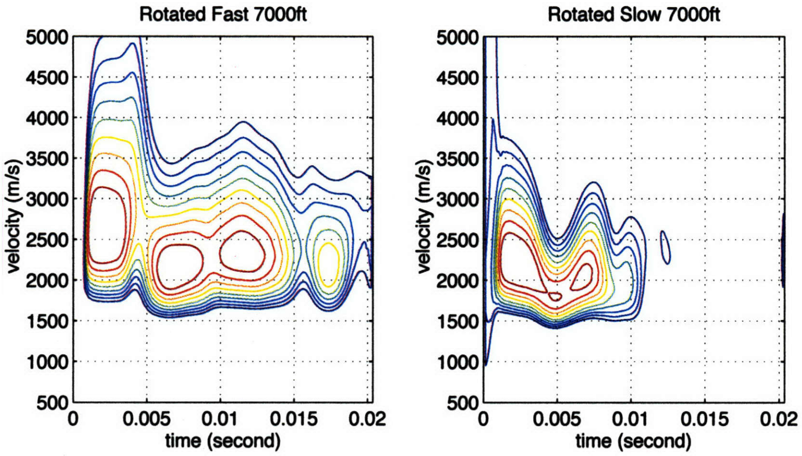

Figure C-20: Semblance analysis results for rotated data at depth 7000ft.

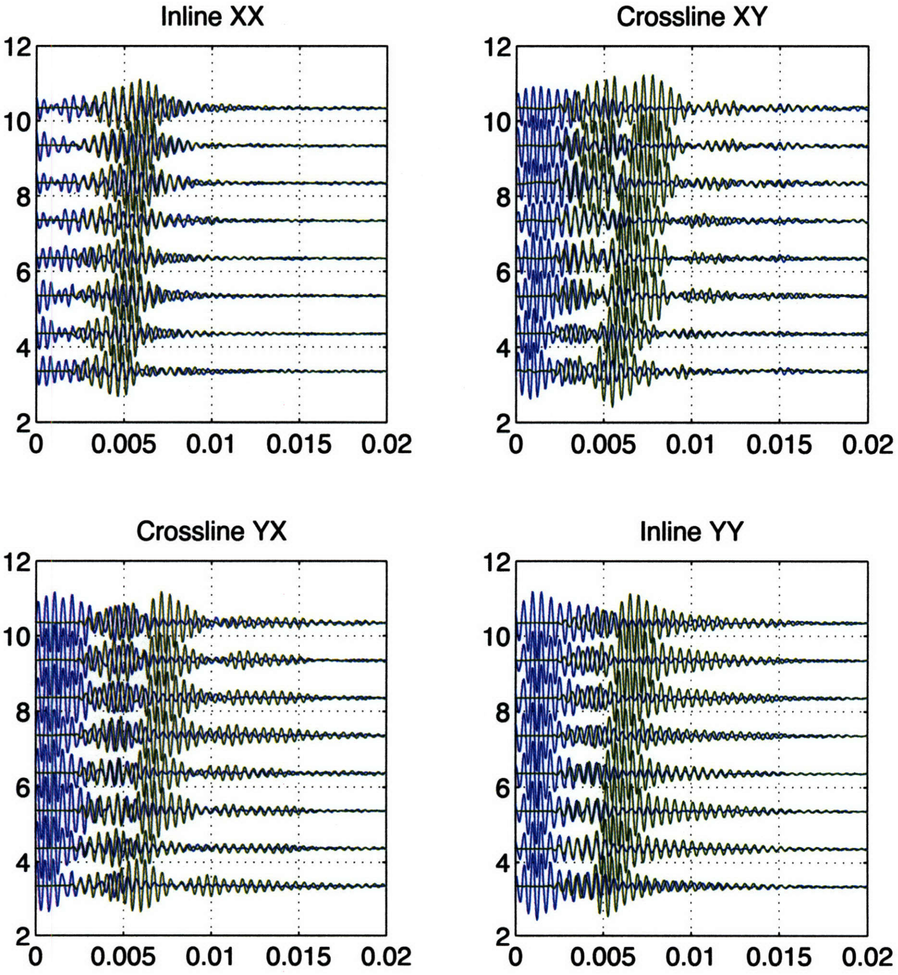

Figure C-21: Original waveforms (green) and after rotation and back propagation as prescribed by inversion results (blue).

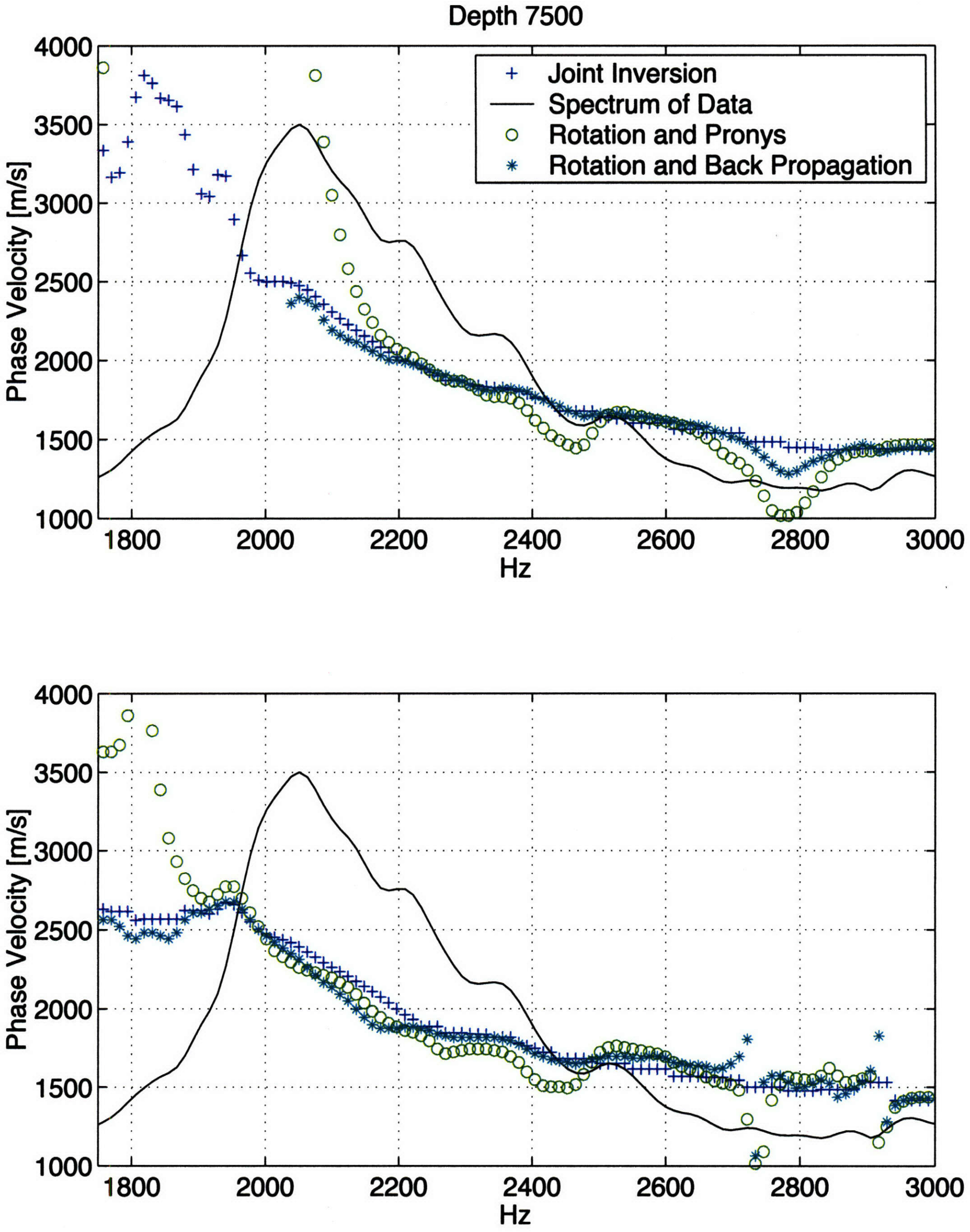

Figure C-22: Dispersion analysis results for depth 7500ft.

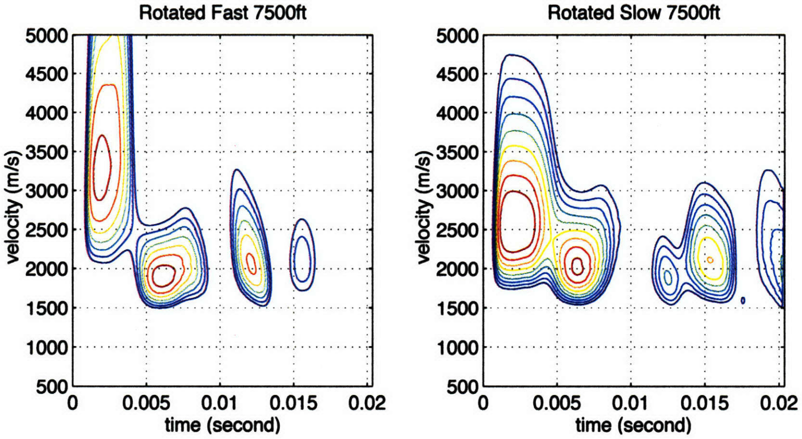

Figure C-23: Semblance analysis results for rotated data at depth 7500ft.

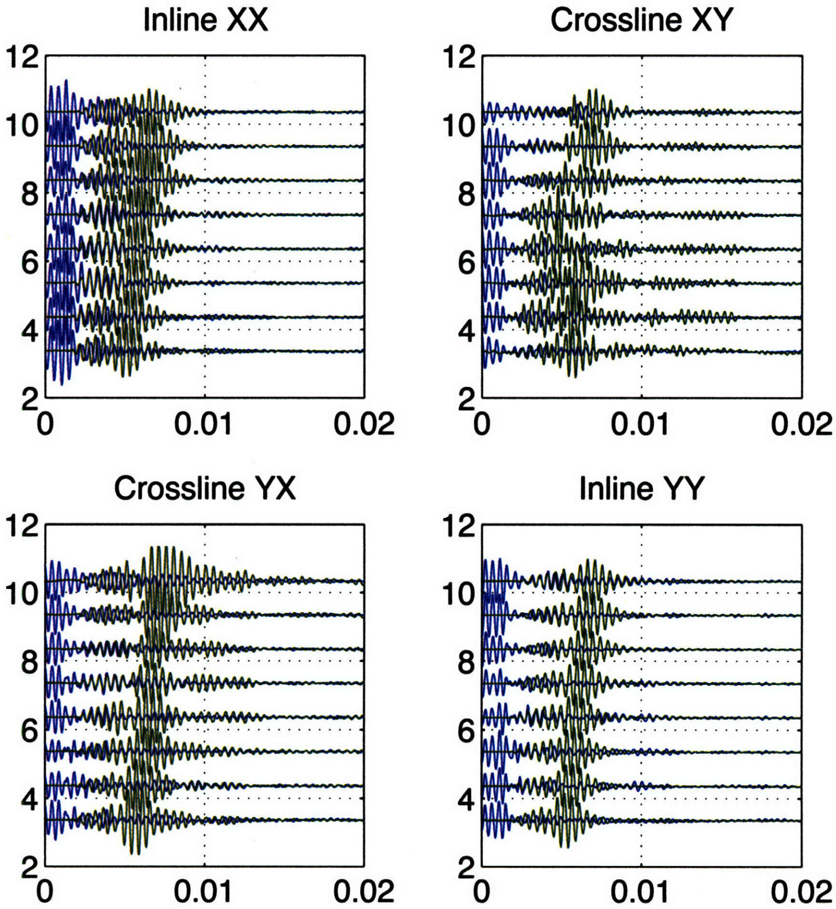

Figure C-24: Original waveforms (green) and after rotation and back propagation as prescribed by inversion results (blue).

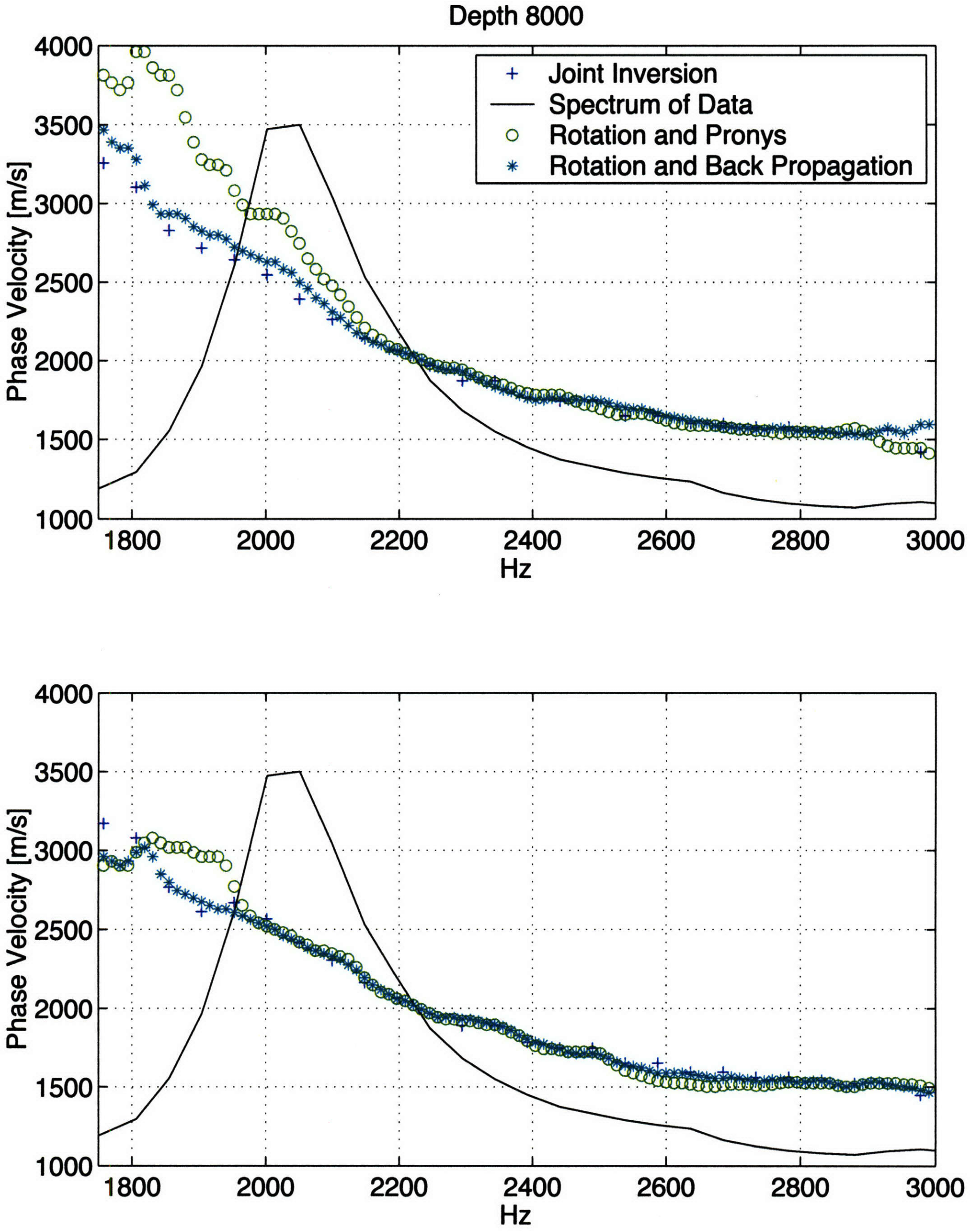

Figure C-25: Dispersion analysis results for depth 8000ft.

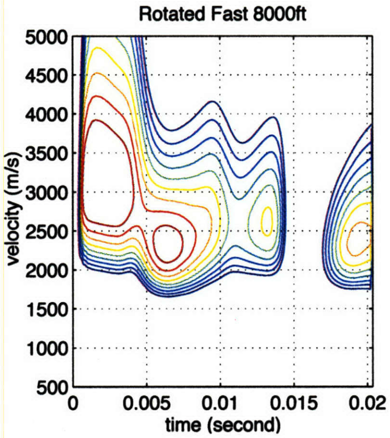

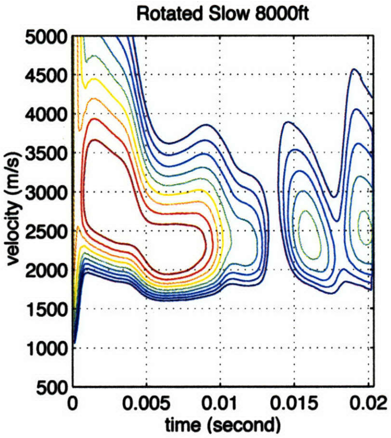

Figure C-26: Semblance analysis results for rotated data at depth 8000ft.

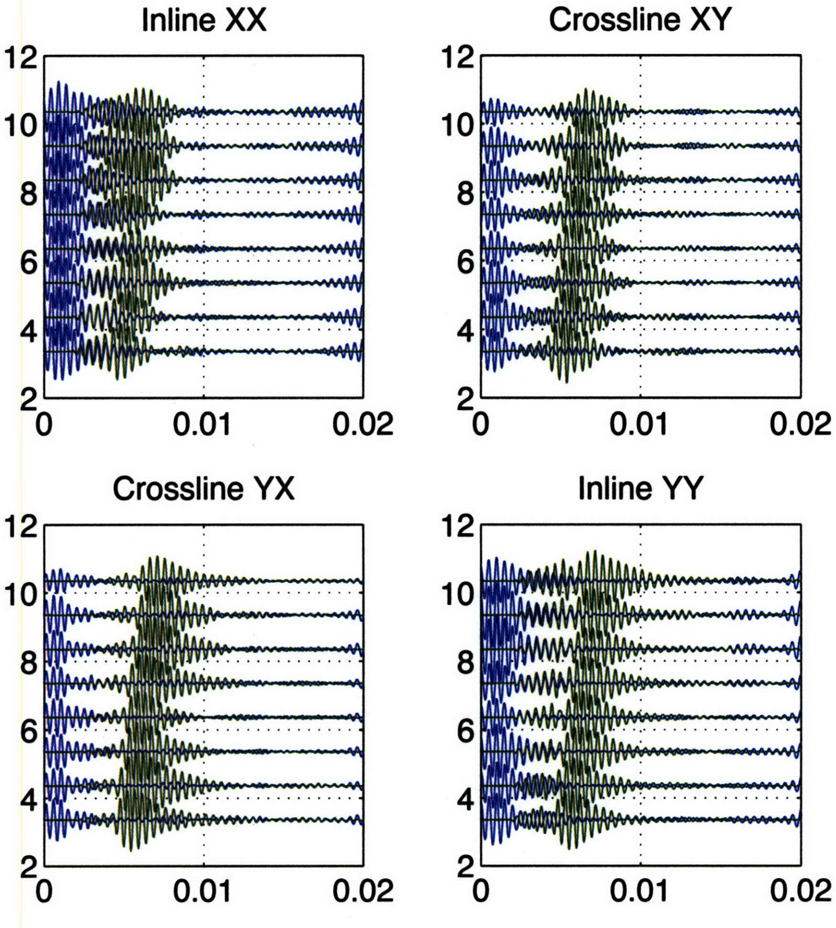

Figure C-27: Original waveforms (green) and after rotation and back propagation as prescribed by inversion results (blue).

Bibliography

Alford, R. M. (1986). Shear data in the presence of azimuthal anisotropy. In *Expanded Abstracts*, pages 476–479. Soc. Expl. Geophys.

Auld, B. (1990). *Acoustic fields and waves in solids*, chapter 4. Krieger.

Baker, L. (1984). The effect of the invaded zone on full wavetrain acoustic logging. *Geophysics*, 49(6):796–809.

Baker, L. and Winbow, G. (1988). Multipole p-wave logging in formations altered by drilling. *Geophysics*, 53(9):1207–1218.

Biot, M. (1952). Propagation of elastic waves in a cylindrical bore containing a fluid. *J. Appl. Phys.*, 23:997–1009.

Blakeman, E. R. (1982). A case study of the effect of shale alteration on sonic transit times. In *Transactions of the SPWLA*. SPWLA.

Boonen, P. and Tepper, R. (1998). Important implications from a comparison of LWD and wireline acoustic data from a gulf of mexico well. In *Transactions of the SPWLA*.

Brie, A. and Saiki, Y. (1996). Practical dipole sonic dispersion correction. In *Expanded Abstracts*, pages 178–181. Soc. Expl. Geophys.

Chan, A. K. and Tsang, L. (1983). Propagation of acoustic waves in a fluid-filled borehole surrounded by concentrically layered transversely isotropic formation. *J. Acoust. Soc. Am.*, 74(5):1605–1616.

Chen, S. T. (1988). Shear-wave logging with dipole sources. *Geophysics.*, v 53:659–667.

Cheng, C. H. and Toksöz, M. N. (1981). Elastic wave propagation in fluid filled boreholes and synthetic acoustic logs. *Geophysics*, 46:1051–1059.

Ellefsen, K. (1990). *Elastic wave propagation along a borehole in an anisotropic medium.* PhD thesis, Massachusetts Institute of Technology.

Goldberg, D., Cheng, A., Blanch, J., and Byun, J. (2003). Analysis of LWD sonic data in low-velocity formations. In *Expanded Abstracts.* Soc. Expl. Geophys.

Hornby, B. E. and Chang, S. K. (1985). A case study of shale and sandstone alteration using a digital sonic tool. In *Transactions of the SPWLA.* SPWLA.

Huang, X. (1998). A study of tectonic stresses in the earth using standard acoustic logging. Technical report, MIT.

Huang, X. (2003). *Effects of tool positions on Borehole acoustic measurements: a stretched grid finite difference approach.* PhD thesis, MIT.

Huang, X., Burns, D. R., and Toksoz, M. N. (1998). Dispersion analysis of cross-dipole data. In *Earth Resources Laboratory MIT Consortia.*

Kimball, C. V. (1998). Shear slowness measurement by dispersive processing of the borehole flexural mode. *Geophysics.*, 63(2):377–344.

Kimball, C. V., Lewicki, P., and Wijeyesekera, N. I. (1995). Error analysis of maximum likelihood estimates of physical parameters from one or more dispersive waves. *IEEE transactions on signal processing*, 43:2928–2936.

Kimball, C. V. and Marzetta, T. L. (1984). Semblance processing of borehole acoustic array data. *Geophysics*, 49(3):274–281.

Kurkijian, A. L. and Chan, S.-K. (1986). Acoustic multipole sources in fluid-filled boreholes. *Geophysics*, 51(1):148–163.

Kurkjian, A. L. (1985). Numerical computation of individual far-feild arrivals excited by an acoustic source in a borehole. *Geophysics*, 50:852–866.

Kurkjian, A. L. and Chang, S. K. (1986). Acoustic multipole sources in fluid filled boreholes. *Geophysics*, 51:148–163.

Lang, S., Kurkjian, A., McClellan, J., Morris, C., and Parks, T. (1987). Estimating slowness dispersion from arrays of sonic logging waveforms. *Geophysics*, 52:530–544.

Leslie, H. and Randall, C. (1992). Multipole sources in boreholes penetrating anisotropic formations: Numerical and experimental results. *J. Acounst. Soc. Am.*, 91(6):12–27.

Market, J., Althoff, G., Barnett, C., Deady, R., and Varsamis, G. (2002). Processing and quality control of LWD dipole sonic measurements. In *Transactions of the SPWLA*. SPWLA.

Paillet, F. L. and White, J. E. (1982). Acoustic modes of propagation in the borehole and their relationship to rock properties. *Geophysics*, 47:1215–1228.

Plona, T., Sinha, B., Kane, M., Shenoy, R., Bose, S., Walsh, J., Endo, T., Ikegani, T., and Skelton, O. (2002). Mechanical damage detection and anisotropy evaluation using dipole sonic dispersion analysis. In *Transactions of the SPWLA*. SPWLA.

Rao, R. (2005). Dispersive wave analysis method and application. In *Borehole Acoustics*. Earth Resources Laboratory, MIT.

Rao V.N, R. (1999). Models in LWD applications. In *Earth Resources Laboratory Consortium Report*, pages (5,1)–(5,13).

Ricks, D. C. (1994). *Elastodynamic modeling of fluid-loaded cylindrical shells with multiple layers and internal attachments.* PhD thesis, Massachusetts Institute of Technology.

Schmitt, D. P. (1988a). Effects of radial layering when logging in saturated porous formations. *J. Acoust. Soc. Am.*, 84(6):2200–2214.

Schmitt, D. P. (1988b). Shear wave logging in elastic formations. *J. Acoust. Soc. Am.*, 84(6):2215–2229.

Schmitt, D. P. (1989). Acoustic multipole logging in a transversely isotropic poroelastic formations. *J. Acoust. Soc. Am.*, 86:2397–2421.

Schmitt, D. P. and Bouchon, M. (1985). Full wave acoustic logging: synthetic microseismograms and frequency wave number analysis. *Geophysics*, 50:1756–1778.

Sinha, B. K. and Kostek, S. (1996). Stress-induced azimuthal anisotropy in borehole flexural waves. *Geophysics*, 61(6):1899–1907.

Sinha, B. K., Norris, A. N., and Chang, S. K. (1994). Borehole flexural modes in anisotropic formations. *Geophysics*, 59:2674–2685.

Tang, X. and Cheng, A. (2004). *Quantitative Borehole Acoustic Methods*, chapter 4. Elsevier.

Tang, X. and Chunduru, R. K. (1999). Simultaneous inversion of formation shear-wave anisotropy parameters from cross-dipole acoustic-array waveform data. *Geophysics*, 64(5).

Tang, X. M., Dubinsky, V., Wang, T., Bolshakov, A., and Patterson, D. (2002). Shear-velocity measurement in the logging-while-drilling environment: Modeling and field evaluations. In *Transactions of the SPWLA*. SPWLA.

Tang, X. M., Reiter, E. C., and Burns, D. R. (1995). A dispersive-wave processing technique for estimating formation shear velocity from diplole and stonely waveforms. *Geophysics*, 60(1):19–28.

Tatham, R. H., Matthews, M. D., Sekharan, K. K., Wade, C. J., and Liro, L. M. (1992). A physical model study of shear wave splitting and fracture intensity. *Geophysics.*, 57(4):647–652.

Thomsen, L. (1986). Weak elastic anisotropy. *Geophysics*, 51:1954–1966.

Tichelaar, B. W. and Hatchell, P. J. (1997). Inversion of 4-c borehole flexural waves to determine anisotropy in a fractured carbonate reservoir. *Geophysics.*, 62(5):1432–1441.

Tsang, L. and Rader, D. (1979). Numerical evaluation of the transient acoustic waveform due to a point source in a fluid-filled borehole. *Geophysics*, 44:1706–1720.

White, J. (1968). Computed response of an acoustic logging tool. *Geophysics*, 33:302–310.

White, J. E. and Tongtaow, C. (1981). Cylindrical waves in transversely isotropic media. *J. Acoust Soc. Am.*, 70(4):1147–1155.

Winbow, G. A. (1988). A theoretical study of acoustic S-wave and P-wave velocity logging with conventional and dipole sources in soft formations. *Geophysics*, 53(10):1334–1342.

Wu, P., Scheibner, D., and Borland, W. (1993). A case study of near-borehole shear velocity alteration. In *Transactions of the SPWLA*. SPWLA.

Zhang, B. and Wang, K. (1996). Theoretical study of perturbation method for acoustic multipole logging in anisotropic formation. *J. Acoust. Soc. Am.*, 99(5):1037–1052.